UNCLASSIFIED

AD NUMBER

ADB231769

NEW LIMITATION CHANGE

TO

Approved for public release, distribution unlimited

FROM

Distribution authorized to U.S. Gov't. agencies only; Proprietary Information; Jul 97. Other requests shall be referred to US Army Medical Research and Materiel Comd., 504 Scott St., Fort Detrick, MD 21702-5012.

AUTHORITY

USAMRMC ltr, 1 Jun 2001.

THIS PAGE IS UNCLASSIFIED

AD______________

AWARD NUMBER DAMD17-96-1-6023

TITLE: Fluorescence Lifetime Imaging for Breast Cancer Detection

PRINCIPAL INVESTIGATOR: Eva M. Sevick Muraca, Ph.D.

CONTRACTING ORGANIZATION: Purdue Research Foundation
West Lafayette, Indiana 47907

REPORT DATE: July 1997

TYPE OF REPORT: Annual

DTIC QUALITY INSPECTED 2

PREPARED FOR: Commander
U.S. Army Medical Research and Materiel Command
Fort Detrick, Maryland 21702-5012

DISTRIBUTION STATEMENT: Distribution authorized to U.S. Government agencies only (proprietary information, July 1997). Other requests for this document shall be referred to U.S. Army Medical Research and Materiel Command, 504 Scott Street, Fort Detrick, Maryland 21702-5012.

The views, opinions and/or findings contained in this report are those of the author(s) and should not be construed as an official Department of the Army position, policy or decision unless so designated by other documentation.

19971210 051

REPORT DOCUMENTATION PAGE

Form Approved
OMB No. 0704-0188

Public reporting burden for this collection of information is estimated to average 1 hour per response, including the time for reviewing instructions, searching existing data sources, gathering and maintaining the data needed, and completing and reviewing the collection of information. Send comments regarding this burden estimate or any other aspect of this collection of information, including suggestions for reducing this burden, to Washington Headquarters Services, Directorate for Information Operations and Reports, 1215 Jefferson Davis Highway, Suite 1204, Arlington, VA 22202-4302, and to the Office of Management and Budget, Paperwork Reduction Project (0704-0188), Washington, DC 20503.

1. AGENCY USE ONLY ***(Leave blank)***

2. REPORT DATE July 1997

3. REPORT TYPE AND DATES COVERED Annual (1 Jul 96 - 30 Jun 97)

4. TITLE AND SUBTITLE Fluorescence Lifetime Imaging for Breast Cancer Detection and Diagnosis

5. FUNDING NUMBERS DAMD17-96-1-6023

6. AUTHOR(S)
Eva M. Sevick Muraca, Ph.D.

7. PERFORMING ORGANIZATION NAME(S) AND ADDRESS(ES)
Purdue Research Foundation
West Lafayette, Indiana 47907

8. PERFORMING ORGANIZATION REPORT NUMBER

9. SPONSORING/MONITORING AGENCY NAME(S) AND ADDRESS(ES)
Commander
U.S. Army Medical Research and Materiel Command
Fort Detrick, Frederick, MD 21702-5012

10. SPONSORING/MONITORING AGENCY REPORT NUMBER

11. SUPPLEMENTARY NOTES

12a. DISTRIBUTION / AVAILABILITY STATEMENT

Distribution authorized to U.S. Government agencies only (proprietary information, July 1997). Other requests for this document shall be referred to U.S. Army Medical Research and Materiel Command, 504 Scott Street, Fort Detrick, Maryland 21702-5012.

12b. DISTRIBUTION CODE

13. ABSTRACT *(Maximum 200*

New screening tools are needed for women for whom x-ray mammography is not suitable. We present a new and novel modality called "fluorescence lifetime imaging" as a potential tool for breast cancer detection and diagnosis. In this technique, the contrast for the diseased tissue is provided by a change in lifetime of fluorescent contrast agents such as porphyrins or some of the newly synthesized lifetime sensitive dyes. Our study involves experimental and computational approaches to explore the technical feasibility of this technique. Experimental studies are planned which include frequency domain measurements of the fluorescent light in a multiple detector - multiple source arrangement. Measurements will be performed for analyte sensitive dyes in heterogeneous tissue phantoms. These measurements will be used as inputs to a developed inverse imaging algorithm to obtain an image of lifetime. Since probe or dye lifetimes are sensitive to biochemical environment, diagnostic information is also obtained in addition to detection of disease. Preliminary computational and experimental results are promising and suggest a new imaging modality with specificity for breast disease.

14. SUBJECT TERMS Breast Cancer

15. NUMBER OF PAGES 99

16. PRICE CODE

17. SECURITY CLASSIFICATION OF REPORT	**18. SECURITY CLASSIFICATION OF THIS PAGE**	**19. SECURITY CLASSIFICATION OF ABSTRACT**	**20. LIMITATION OF ABSTRACT**
Unclassified	Unclassified	Unclassified	Limited

NSN 7540-01-280-5500

Standard Form 298 (Rev. 2-89)
Prescribed by ANSI Std. Z39-18
298-102

FOREWORD

Opinions, interpretations, conclusions and recommendations are those of the author and are not necessarily endorsed by the U.S. Army.

____ Where copyrighted material is quoted, permission has been obtained to use such material.

____ Where material from documents designated for limited distribution is quoted, permission has been obtained to use the material.

____ Citations of commercial organizations and trade names in this report do not constitute an official Department of Army endorsement or approval of the products or services of these organizations.

____ In conducting research using animals, the investigator(s) adhered to the "Guide for the Care and Use of Laboratory Animals," prepared by the Committee on Care and Use of Laboratory Animals of the Institute of Laboratory Resources, National Research Council (NIH Publication No. 86-23, Revised 1985).

____ For the protection of human subjects, the investigator(s) adhered to policies of applicable Federal Law 45 CFR 46.

____ In conducting research utilizing recombinant DNA technology, the investigator(s) adhered to current guidelines promulgated by the National Institutes of Health.

____ In the conduct of research utilizing recombinant DNA, the investigator(s) adhered to the NIH Guidelines for Research Involving Recombinant DNA Molecules.

____ In the conduct of research involving hazardous organisms, the investigator(s) adhered to the CDC-NIH Guide for Biosafety in Microbiological and Biomedical Laboratories.

Eva M Sevick-Muraca 7/30/97
PI - Signature Date

TABLE OF CONTENTS

Report Documentation Page 2

Foreword. 3

Table of Contents 4

I. Introduction 5

II. Computational methods. 6

III. ExperimentalMethods and Approaches. 9

IV. Experimental Results and Discussion. .12

V. Summary 16

VI. Year Two Activities 17

VII. References. 17

Appendices

Figures

publication: “Imaging of fluorescent yield and lifetime from multiply scattered light re-emitted from random media”

manuscript: “The role of higher order scattering in solutions to the forward and inverse optical imaging problems in random media”

I. Introduction

With the development of near-infrared (NIR) laser diodes, the synthesis of fluorescent dyes with excitation and emission spectra in the NIR wavelength regime has accelerated in the past decade. Examples of fluorescent dye development include (i) microscopy dyes for sensing cellular metabolic and structural constituents; (ii) DNA-binding dyes for automated DNA sequencing; and (iii) photodynamic agents for anti-cancer, therapeutic action. Armed with the knowledge that NIR light can penetrate several centimeters into tissue [for review see reference (1)], one can speculate that these and other designer fluorescent dyes may offer diagnostic opportunities when used in conjunction with optical imaging techniques as contrast agents for the detection of diseased tissues, specifically breast cancer.

The detection of disease via the use of fluorescent dyes and photodynamic drugs as contrast agents for the detection of disease has been proposed by several investigators. However, a long-standing problem has been the low uptake or "leakage" into diseased tissues providing insufficient contrast for detection of disease - making it difficult to detect the diseased tissue signal from the background tissue signal. While targeted delivery may improve uptake ratios and contrast imparted by these agents, drug and contrast agent targeting approaches have been rather elusive even in conventional imaging modalities such as magnetic resonance imaging and x-ray computed tomography. Investigators have sought to improve optical contrast independent of uptake ratio by employing dyes which fluoresce differently in diseased and normal tissues. The use of agents whose emission characteristics vary with tissue pH (2, 3) and O_2 (4) may not only enhance detection of diseased tissues by the nature of differing fluorescent properties, but may also contain diagnostic information regarding the disease.

The difficulty, however, lies in using the multiply scattered light detected at the tissue-air interface to reconstruct an image which differentiates internal tissues on the basis of uptake and the fluorescent properties of quantum yield, and lifetime. In ongoing work in this and other laboratories, investigators have demonstrated the capacity for fluorescent lifetime and quantum yield imaging from frequency-domain measurements of modulation phase-shift and amplitude demodulation conducted at the surface of a simulated tissue phantom (5-7). Under this support, the aims of this two year exploratory research project are:

(1) To develop inverse imaging algorithms providing lifetime and yield mapping of tissues as thick as five centimeters;

(2) To measure the temporal, re-emitted excitation and fluorescence from tissue phantoms using frequency-domain techniques; and

(3) To use these measurements as input into the inverse imaging algorithm for reconstruction of lifetime and yield maps.

Finally, in this current last year of the project, we will accomplish the last and final aim of the project,

(4) To test computational and experimental approaches using dyes which enable analyte concentration determination from measurement of lifetime and yield within a tissue-mimicking phantom.

Specifically, we seek to develop fluorescence lifetime imaging techniques for screening in a population of women who are at high risk for the disease, and for those women who require prognostic indicators of lymphatic involvement. Under other support, the development of imaging instrumentation and contrast agents for identification of disease is ongoing. This DOD support focuses upon the development of inverse solution procedures and coupling of measurements to image algorithms for the detection of disease. These specific aims are the foundations of the technology.

In the following, we outline the computational and experimental methods as well as the results obtained in this first year of the exploratory research grant.

II. Computational methods

During the past year, computational efforts for reconstructing lifetime and quantum yield from measurements of phase and amplitude modulation have been spearheaded by Dilip Y. Paithankar, and more recently Tamara L. Troy in the Photon Migration Laboratory. Both studies, although separate, iteratively solved the diffusion equations describing light propagation and fluorescence generation in a random medium as the spatial distribution of lifetime and quantum efficiency were altered. The map of these fluorescent optical properties that best matched simulated measurements and predictions from the diffusion equations provided the optical image of interior heterogeneities from exterior measurements. The preliminary work described in the publication, "Imaging of fluorescent yield and lifetime from multiply scattered light re-emitted from random media," involved reconstruction of lifetime, τ, and the product of the quantum efficiency and absorption coefficient owing to fluorophore, $\phi\mu_{a_{x\to m}}$, within a circular 2-D phantom with 20 detectors and 4 sources of modulated light. This latter quantity, $\phi\mu_{a_{x\to m}}$, is related to the local concentration of fluorophore, [C], via the extinction coefficient, ε:

$$\phi\mu_{a_{x\to m}} = \phi\varepsilon[C] \tag{1}$$

and convolutes changes in contrast agent uptake with changes in quantum yield due to differing biochemical environments. Details of the computational approach and results are shown in the publication included in the Appendix. In brief, the results show that it is possible to reconstruct interior images of lifetime, τ, and fluorescent yield, $\phi\mu_{a_{x\to m}}$, from exterior measurements of phase-shift and amplitude modulation made at the tissue-air interface.

However, uptake or local concentration of fluorophore, [C], may not be specific to disease. The biochemistry probed quantum yield, ϕ, changes of designer fluorophores may very well be. Consequently, to enhance the specificity for detection of breast cancer in women who are at high risk, or who show positive mammograms, we sought to develop an imaging technique that focused upon specificity to disease as detected by ϕ rather than the product, $\phi\mu_{a_{x\to m}}$. More recently, Troy and Sevick-Muraca, developed an inversion technique that could segregate changes in lifetime and quantum efficiency from differences in local concentrations of fluorescent contrast agents. This is especially important for the specific identification of disease based upon local biochemical environment.

In this second approach in the laboratory, the uptake of fluorophore is independently assessed by reconstruction of absorption owing to fluorophore alone, or $\mu_{a_{x\rightarrow m}}$. The reconstruction is performed by simulating measurements of phase-shift and amplitude modulation at excitation wavelength prior to and following administration of a contrast agent. With the exterior values of $\mu_{a_{x\rightarrow m}}$ determined, simulated measurements of phase-shift and amplitude modulation at the emission wavelengths are then used to reconstruct values of lifetime, τ, and quantum efficiency, ϕ.

In the most recent work by Sevick and Troy, the simulated phantom mimics the experimental system in the Photon Migration Laboratory consisting of a square rectangular phantom whose surface is imaged onto the photocathode of a gain-modulated image intensified CCD camera. While measurements of fluorescent and excitation phase-shift and amplitude modulation across one face of the phantom are possible at a resolution of 512 x 512 (8,9); we simulate the use of 1x17 detection pixels in our inversions. With four sides imaged, there are 56 (4 x 17 - 2) detectors positioned around the periphery and 4 sources located midplane on each of the four sides.

Under conditions in which contrast is obtained from a 10:1 uptake alone, i.e., $\mu_{a_{x\rightarrow m}}$, the 2-D detection of a 0.06 cm^2 heterogeneity embedded in a 16 cm^2 phantom can be distinguished from a somewhat noisy background, as shown in Figure 1. This uptake ratio is the best physiologic uptake reported for a photodynamic agent. It is important to note that the data used in the reconstruction of Figure 1 is simulated and not experimental. The data are simulated with an ample noise level of 0.1 degree in phase-shift and 1% in amplitude demodulation at the excitation wavelength at 100 MHz modulation frequency.

On the otherhand, when additional contrast is provided by a decrease in lifetime from 10 nanoseconds in the surrounding normal tissues, to 1 nanosecond in the simulated diseased heterogeneity, the contrast is enhanced providing better detection of the heterogeneity (Figure 2). This latter result assumes that the uptake ratio has been correctly detected from excitation measurements. It is important to note that fluorescent measurements are simulated with an ample noise level of 0.1 degree in phase-shift and 1% in amplitude demodulation.

Less encouraging, but still promising are the results on quantum efficiency. Albeit a noisy image reconstruction, Figure 3 illustrates the additional contrast provided by an increase in quantum yield from a value of 0.01 in the surrounding normal tissues, to a value of 0.1 in the diseased tissue. These results are again provided for a physiological uptake ratio of 10:1. It is important to note that DNA-binding dyes, although not candidates for contrast agent administration in patients, have a quantum yield change of one thousand fold difference in healthy and dying cells.

These results are encouraging, suggestive that fluorescence lifetime and quantum efficiency can be exploited to provide contrast beyond that provided by uptake changes.

In year two, work continues to expand imaging algorithms for use of multi-frequency, multi-wavelength measurements. In addition, we are exploring the use of non-iterative methods to provide rapid image formation for real time clinical use. Our work in this domain is not described here, but rather in the manuscript accepted for publication and found in the Appendix.

III. Experimental Methods and Approaches

In order to experimentally assess the contrast provided by fluorescence and absorption, frequency-domain measurements were conducted in a tissue-simulating phantom using micromolar concentrations of IR-125 (or indocyanine green, ICG) (ACROS Organics, Fairlawn, NJ), and DTTCI (ACROS Organics, Fairlawn, NJ). The tissue phantom, illustrated in Figure 4, consisted of a cylindrical Plexiglas container, 20 cm in diameter, 30.5 cm in height, and filled with 0.5% Intralipid solution (Kabi Pharmacia, Clayton, NC) to mimic tissue scattering properties. The heterogeneity consisted of a 9 mm inner diameter cylindrical glass container in which the same scattering solution was held. The appropriate concentrations of dye were added to both solutions to explore the issues of fluorescent contrast for frequency-domain photon migration imaging. Measurements of phase-shift and amplitude demodulation were conducted as the position of the tissue mimicking heterogeneity was precisely moved using an x-y translation stage (PMC200-P, Newport, Irvine, CA) to various distances midpoint between the source and detector. Contrast was measured as a function of distance, x, between the inner circumference of the phantom and the leading edge of the heterogeneity as shown in Figure 4. An object position of zero denotes contact between the phantom wall and the heterogeneity. Measurements were conducted in the absence of dyes to assess the contribution of the vessel on measurements of phase-shift and amplitude modulation. Measurements of excitation light showed less than a one degree phase-shift and a 0.1% modulation change owing to the presence of the glass vessel filled with the same Intralipid solution as contained in the surrounding medium. These deviations due to the vessel wall of the heterogeneity occurred only when it was close to of the phantom wall. Since these differences are small compared to the changes owing to fluorescence in our measurement, we did not account for them in the presentation of our results.

Indocyanine green, ICG is a FDA approved, tricarbocyanine dye used typically for hepatic function studies and ophthalmic angiography studies. It has also been used as an absorption contrast agent for imaging of rat gliomas and tumor margins (10) and as a fluorescent contrast agent for the estimation of burn depth (11). Although ICG has absorption and fluorescence peaks at 764 nm and 803 nm, respectively, the absorption and fluorescence measurements were conducted at 780 nm and 830 nm, respectively, to be consistent with the characteristics of DTTCI. ICG dosage corresponds to uniform systemic concentrations of 1-3 μM, 50-75 fold lower than lethal levels. While these ICG concentrations are also in the therapeutic range for many photodynamic agents, we have found that the quantum efficiency of ICG is tenfold or more greater than many photodynamic agents. Nonetheless, in the work presented herein, we assess the contrast offered by ICG for photon migration imaging using clinically realistic tissue concentrations of ICG. Extrapolation of our results using ICG to therapeutic concentrations of photodynamic agents must account for the differences in fluorescent yield.

Measurements of phase-shift and amplitude modulation owing to dye

Experimental measurements of fluorescent phase-shift and amplitude demodulation were conducted at modulation frequencies of 80, 160, and 240 MHz using an ISS (ISS, Champaign, IL) based system illustrated in Figure 5. The excitation source consisted of an Argonpumped, picosecond pulsed Ti:Sapphire laser (Spectra-Physics, MountainView, CA) operating at 780 nm, at a laser repetition rate of 80.00000 MHz and an average power of 1.3 W. A glass microscope slide was used to split the beam, directing 90% of the light into a 1000 micron fiber (HCP-M1000T-08, Spectran Specialty Optics Co., Avon, CT) coupled to the tissue phantom model. The remaining 10% was delivered to a reference photomultiplier tube (PMT), (R928, Hamamatsu Photonics) to provide a reference signal. The multiply scattered light detected at the tissue phantom periphery was collected using a second 1000 micron fiber located 2.8 circumferential centimeters from the source fiber. The light was delivered to a sampling PMT outfitted with either neutral density filters (CVI Laser Corporation, Albuquerque, NM) and a 780±10 nm interference filter (model #10-780-4-1.00, CVI Laser Corporation, Albuquerque, NM) for collecting the multiply scattered, excitation light, or an 830±10 nm interference filter (model #10-830-4-1.00,CVI Laser Corporation, Albuquerque, NM) to monitor the generated fluorescence. The PMTs were gain modulated at a harmonic of the laser repetition rate plus an offset frequency of 100 Hz. The heterodyned signal was then acquired and analyzed for phase-shift and amplitude demodulation using ISS electronics and software.

Measurement of extinction coefficients, quantum yields and lifetimes

The extinction coefficients of DTTCI and ICG were determined at 780 nm and 830 nm using a double-beam spectrophotometer (Spectronic Genesys 5, Milton Roy, Rochester, NY) from a series of micromolar samples diluted in water. Fluorescent quantum yield measurements were conducted using a spectrofluorometer (Fluorolog-2, SPEX, Edison, NJ). These values were determined with comparison to measurements of ICG in DMSO using the published quantum yield at 780 and 830 nm excitation/fluorescent wavelengths (12). Lifetime measurements were conducted with phase fluorimetry using IR-140 (ACROS Organics, Fairlawn, NJ) as a standard. Table I lists the extinction coefficients, quantum yield, and lifetime of the two dyes in water. These properties are assumed to be reflective of those in 0.5% Intralipid.

Experimental protocols

Table II summarizes the experiments involving a single fluorescent heterogeneity designed to evaluate (i) the influence of lifetime on contrast, (ii) the effect of uptake ratio on the fluorescent and absorption contrast, and (iii) the influence of fluorescent surroundings on the contrast enabling detection of a single body.

IV. Experimental Results and Discussion

Influence of lifetime on fluorescent contrast

In order to assess the influence of lifetime on contrast, two Intralipid solutions containing ICG and DTTCI at concentrations of 2.0 and 4.2 mM respectively were employed separately as heterogeneities within the tissue phantom. The DTTCI ad ICG concentrations were chosen since they reflected similar fluorescent cross sections ($\phi\mu_{a_{x\to m}} = 4\text{x}10^{-3}$ and $6\text{x}10^{-3}$), yet different lifetimes (1.18 and 0.56 ns, respectively). Figure 6a and 6b illustrate the phase-shift difference and amplitude demodulation for the excitation and emission light reported relative to the absence case as a function of the lateral position of the 2.0 mM ICG filled heterogeneity. The closed symbols denote fluorescent measurements made with the 830 nm interference filter while the open symbols denote excitation measurements conducted with neutral density filters and the 780 nm interference filter. Comparison of signals shows that greater phase-shift and amplitude demodulation contrast at distances farther from the periphery is afforded by fluorescence measurements. This occurs due to the lifetime or added time-lag of the emission process that is inherent in fluorescence, but not in absorbance measurements. In addition, the fluorescent contrast owing to a heterogeneity position greater than 4 cm away from the source and detector is enhanced at lower modulation frequencies, consistent with the observation of greater excitation photon sampling volume at lower modulation frequencies (12).

Figures 7a and 7b contain the analogous data for the 4.2 µM DTTCI in Intralipid solution. Since similar fluorescent cross sections is available in the two measurements involving the two dyes, the difference in contrast between the DTTCI and ICG fluorescence measurements described in Figures 6 and 7 must be due primarily to differences in lifetime. As the lifetime of the fluorescent dye in the heterogeneity increases, the measured amplitude demodulation should decrease and the contrast available from amplitude demodulation increases. Indeed the maximum amplitude demodulation owing to DTTCI is approximately

0.5 while for ICG is 0.7, consistent with the greater lifetime of the DTTCI dye. In addition, as the lifetime of the fluorescent dye in the heterogeneity increases the fluorescent phase-shift should increase, and the contrast available from phase-shift increases. Indeed the maximum contrast afforded by phase-shift owing to DTTCI is approximately 45 degrees while for ICG is approximately 30 degrees, again consistent with the greater lifetime of DTTCI. The differences in absorption measurements between DTTCI and ICG arise due to the differences in absorption cross sections of the two solutions. We have repeated the experiments shown in Figures 6 and 7 with the exception that concentrations yielding identical absorption cross sections were employed. The results show similar behavior to that as illustrated in Figures 6 and 7 and are not shown here for brevity. Nonetheless, our results show that frequency-domain measurements contain information of fluorescence lifetime and can be used to provide diagnostic information if lifetime can be extracted from the multiply scattered signal with inverse imaging algorithms as proposed by Sevick-Muraca, *et al.,* (8) and O'Leary, *et al.* (9).

The effect of uptake on fluorescent and absorption contrast

Since the administration of contrast agents can hardly expect to result in perfect uptake into tissue regions of interest, a study was conducted to investigate the reduction of contrast owing to imperfect uptake. Figures 8a and 8b illustrate the phase-shift and amplitude demodulation as a function of position of a heterogeneity containing a one hundred fold greater concentration of ICG than its surroundings. Measurements are reported as a function of the heterogeneity position away from the source and detector. The concentration of ICG in the scattering solution comprising the heterogeneity was 2.3 μM. Fluorescent and excitation measurements are reported relative to those conducted in the absence of the heterogeneity. The shaded symbols denote referenced fluorescence measurements made with the 830 nm interference filter while the open symbols denote referenced excitation measurements conducted with the 780 nm interference filter and neutral density filters. Upon comparison to the perfect uptake results illustrated in Figure 6, one finds that the magnitude of contrast is dramatically reduced when the partitioning between simulated diseased and normal tissues is reduced from a perfect uptake ratio to a 1:100 uptake ratio from the surroundings to the heterogeneity. Nonetheless, the magnitude of contrast offered by fluorescence phase-shift and amplitude demodulation measurements still exceeds that possible by absorption measurements in agreement with the argument presented in Section 2. This again can be attributed to the additional contrast offered by the fluorescence process. In addition, the experimental measurements of fluorescence contrast appears to be more sensitive to heterogeneity position than those measurements of contrast owing only to absorption.

Figures 9a and 9b illustrate similar measurements when the partitioning between the heterogeneity and surrounding scattering medium is tenfold. Again, the absorption measurements indicate the ability to detect a heterogeneity located between zero and 1 cm from the phantom periphery using phase and amplitude demodulation measurements, while fluorescent measurements afford detection of the heterogeneity located twice as deep within the phantom. In addition, the sensitivity of phase contrast to heterogeneity position appears greater for fluorescence measurements than when contrast is owing to absorption.

Current approaches for frequency-domain optical imaging in tissues involve reconstructing perturbations in tissue absorption. Since the best possible contrast that can be offered by absorption is that due to a perfect absorber, we evaluated the contrast due to fluorescence in comparison to that due to perfect absorber. Using a black painted Plexiglas rod 9 mm in diameter, measurements of phase-shift and amplitude demodulation of the multiply scattered excitation light at 780 nm were conducted as the perfect absorber was moved away from the source and detector. Measurements are reported relative to the "absence" case. Figure 10a and 10b illustrates the contrast offered by phase-shift and amplitude demodulation measurements as a function of heterogeneity position for a 9 mm diameter perfect absorber and a 9 mm diameter tube filled with a 3 μM concentration of ICG. In the case of the fluorescence measurements, the phase-shift and amplitude demodulation were reported relative to the "absence" case in which the fluorescent body was moved more than 5 cm away from the source and detector. These results point to the superior contrast offered by fluorescence frequency-domain approaches since the contribution of fluorescent lifetime is included in the measurement.

Since partitioning of contrast agents is a common obstacle to even conventional imaging modalities, one might expect similar difficulties involving fluorescent contrast agents for optical imaging. The ability to detect a fluorescent body in scattering medium which mimics tissues has been demonstrated by several investigators However no studies have addressed the contrast available when there is imperfect partitioning in the tissue volume of interest. We have demonstrated that the contrast due to fluorescence exceeds that due to absorption even under conditions of imperfect partitioning. The advantage for fluorescent biomedical optical imaging may lie in the additional contrast offered by changing the quantum yield and lifetime of contrast agents when inside the tissue region of interest.

Influence of lifetime and quantum yield in heterogeneity and surroundings

In order to evaluate the contribution of changing lifetime upon the contrast offered by fluorescent frequency-domain measurements, Intralipid solutions of DTTCI and ICG fluorescent dyes were employed in the surroundings and the heterogeneity to evaluate the impact of changing lifetimes upon measured contrast. In all experiments, the concentrations of dyes were maintained such that the absorption cross section due to dye in the heterogeneity was approximately one hundred times that in the surrounding medium. In one experiment, the DTTCI dye solution with the longer lifetime was employed in the heterogeneity while the ICG solution comprised the surrounding medium. In the second experiment, the long-lifetime DTTCI dye solution was employed as the surrounding medium while the shorter lifetime ICG solution was used in the heterogeneity.

The open symbols in Figures 11 and 12 illustrate the phase-shift and amplitude demodulation reported at 80 MHz relative to the absence case when the longer lived fluorescent dye was partitioned within the heterogeneity ($[C_{DTTCI}]=4\text{x}10^{-6}$ M, $\mu_{a_{x\rightarrow m}}=1.7\text{x}10^{-1}$ cm^{-1}) and the short-lived dye constituted the surroundings ($[C_{ICG}]=1\text{x}10^{-8}$ M, $\mu_{a_{x\rightarrow m}}=1.3\text{x}10^{-3}$ cm^{-1}). The filled symbols illustrate similarly obtained data with the exception that the longer lived fluorescent dye was partitioned within the surroundings ($[C_{DTTCI}]=4\text{x}10^{-8}$ M, $\mu_{a_{x\rightarrow m}}=1.7\text{x}10^{-3}$ cm^{-1}) and the short-lived dye constituted the heterogeneity ($[C_{ICG}]=1\text{x}10^{-6}$ M, $=1.3\text{x}10^{-1}$ cm^{-1}). The filled symbols denote referenced fluorescent measurements made with the 830 nm interference filter while the open symbols denote referenced excitation measurements conducted with the 780 nm interference filter. There are several points to note: (1) Since the absorption cross sections of the surroundings and heterogeneities remain constant between the two experiments, the excitation phase-shift and amplitude demodulation measurement in Figures 11 and 12 show nearly identical phase and amplitude demodulation contrast; (2) The fluorescent phase contrast exhibited by a longer-lived, fluorescent heterogeneity in a shorter-lived, fluorescent surroundings results in a greater phase-shift when compared to the fluorescent phase contrast exhibited by a shorter lived fluorescent heterogeneity in a longer lived fluorescent surroundings (Figure 11); and (3) Even though the quantum yield of DTTCI is three times and the lifetime is double that of ICG (see Table I), the contrast provided by amplitude demodulation results in values less than one when DTTCI comprises the fluorescent heterogeneity (Figure 12). Conversely, the contrast provided when ICG comprises the fluorescent heterogeneity results in amplitude demodulation values greater than one (Figure 12).

These results demonstrate that fluorescent lifetime and quantum yield, properties that are dependent upon local biochemical environment, can be reflected in the multiply scattered fluorescent signals detected from the periphery of tissue simulating phantoms. Upon application of inverse imaging algorithms, determinations of lifetime and yield maps of interior heterogeneities may be possible.

V. Summary

The performance of contrast agents for conventional imaging modalities can be limited by the less than perfect partitioning in diseased tissues of interest. The use of fluorescent, time-dependent optical imaging techniques and algorithms, as demonstrated with frequency-domain approaches shown herein, offers the ability for enhanced biomedical contrast owing to changing fluorescent properties of lifetime and quantum yield when localized in the tissue volume of interest. In this work, we have pointed out the possibility for enhanced contrast provided by fluorescence kinetics and suggest that contrast agents designed for biomedical optical imaging should employ these concepts for better detection, localization, and characterization in non-invasive NIR imaging.

VI. Year Two Activities

In year 2, we will couple the inversion algorithms with experimental measurements conducted with a image intensifier CCD camera. Our goal will be to perform analyte sensing from lifetime and quantum efficiency measurements.

VII. References

1. Wilson, B.C., E.M. Sevick, M.S. Patterson and B. Chance (1992) Time-dependent optical spectroscopy and imaging for biomedical applications. *Proc. IEEE*, **80**, 918-930.

2. Mordon, S., J.M. Devoisselle and V. Maunoury (1994) *In vivo* pH measurement and imagng of tumor tissue using a pH-sensitive fluoroscent probe (5,6-Carboxyfluorescein): Instrumental and Experimental Studies. *Photochem. & Photobiol.*, **60**, 274-279.

3. Russell, D.A., R.H. Pottier and D.P. Valenzeno (1994) Continuous, noninvasive measurement of *in vivo* pH in conscious mice. *Photochem. & Photobiol.*, **59**, 309-313.

4. Vinogradov, S.A., L.-W. Lo, W.T. Jenkins, S.M. Evans, C. Koch and D.F. Wilson (1996) Noninvasive imaging of the distribution in oxygen in tissue in vivo using near-infrared phosphors. *Biophysical J.*, **70**, 1609-1617.

5. Paithankar, D.Y., A.U. Chen, B.W. Pogue, M.S. Patterson and E.M. Sevick-Muraca, "Imaging of fluorescent yield and lifetime from multiply scattered light re-emitted from tissues and other random media. *Appl. Optics*, 36, 2260-2272.

6. O'Leary, M.A., D.A. Boas, B. Chance and A.G. Yodh (1996) Fluorescence lifetime imaging in turbid media. *Optics Letters*, **21**, 158-160.

7. Sevick-Muraca, E.M., C.L. Hutchinson and D.Y. Paithankar (1996) Optical tissue biodiagnostics using fluorescence lifetime. *Optics and Photonics News*, **7**, 25-28.

8. Reynolds, J.S., Troy, T.L., and E.M. Sevick-Muraca, "Multi-pixel techniques for frequency-domain photon migration imaging," Biotech. Progress, *in press.*

9. Troy, T.L., Reynolds, J.S., and E.M. Sevick-Muraca (1997) "Photon migration imaging using multi-pixel measurements," Proc. SPIE: Optical Tomography and Spectroscopy of Tissue: Theory, Instrumentation, Model, and Human Studies, II, vol. 2979.

10. Haglund, M.M., D.W. Hochman, A.M. Spence and M.S. Berger (1994) Enhanced Optical Imaging of Rat Gliomas and Tumor Margins. *Neurosurgery*, **35**, 930-939.

11. Sheridan, R.L., K.T. Schomacker, L.C. Lucchina, J. Hurley, L.M. Yin, R.G. Tompkins, M. Jerath, A. Torri, K. Greaves, D. Bua and N.S. Nishioka (1995) Burn depth estimation by use of indocyanine green fluorescence: initial human trial. *J. Burn Care Rehabil.* **16**, 602-604.

12. Benson, R.C. and H.A. Kues (1977) Absorption and fluorescence properties of cyanine dyes. *Journal of Chemical and Engineering Data*, **22,** 379-383.

Figure 1

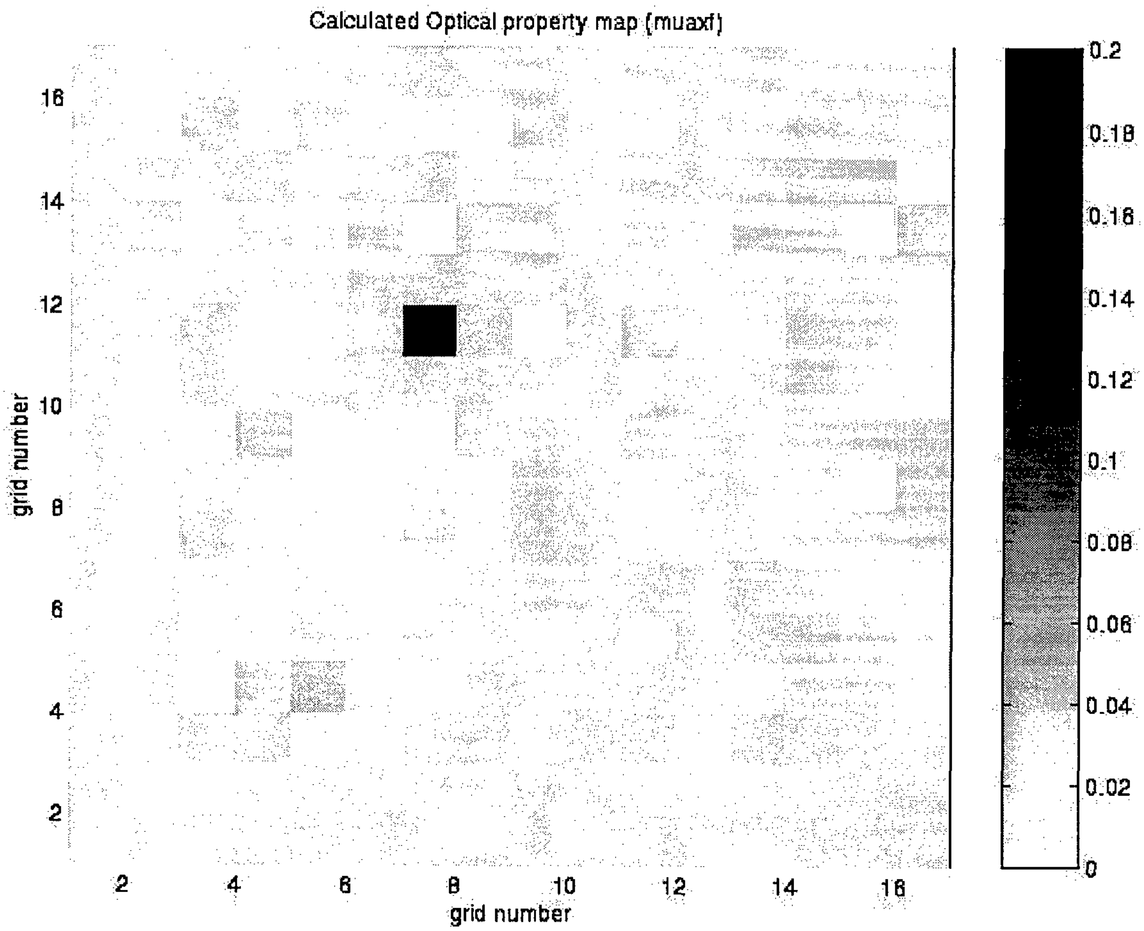

Calculated Optical property map (muaxf)
grid number
grid number
2
4
6
8
10
12
14
16
0
0.02
0.04
0.06
0.08
0.1
0.12
0.14
0.16
0.18
0.2

Figure 2

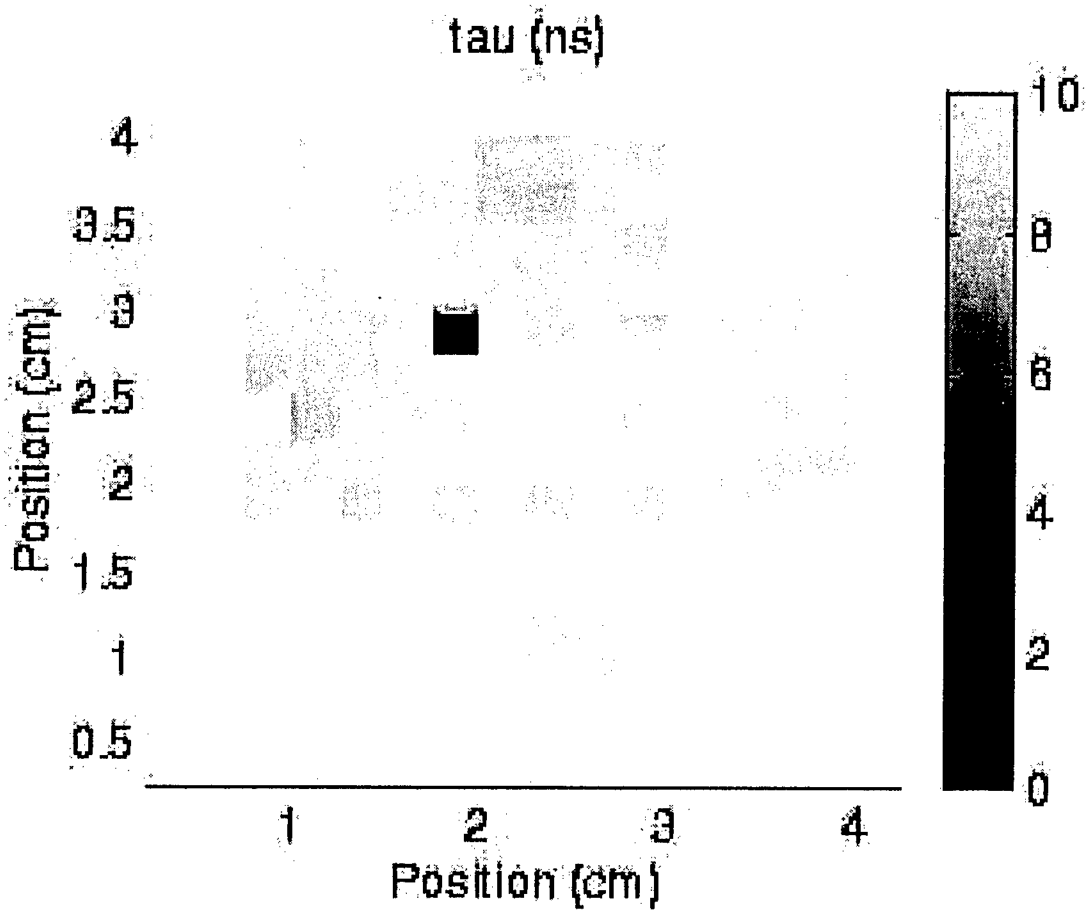

Figure 3

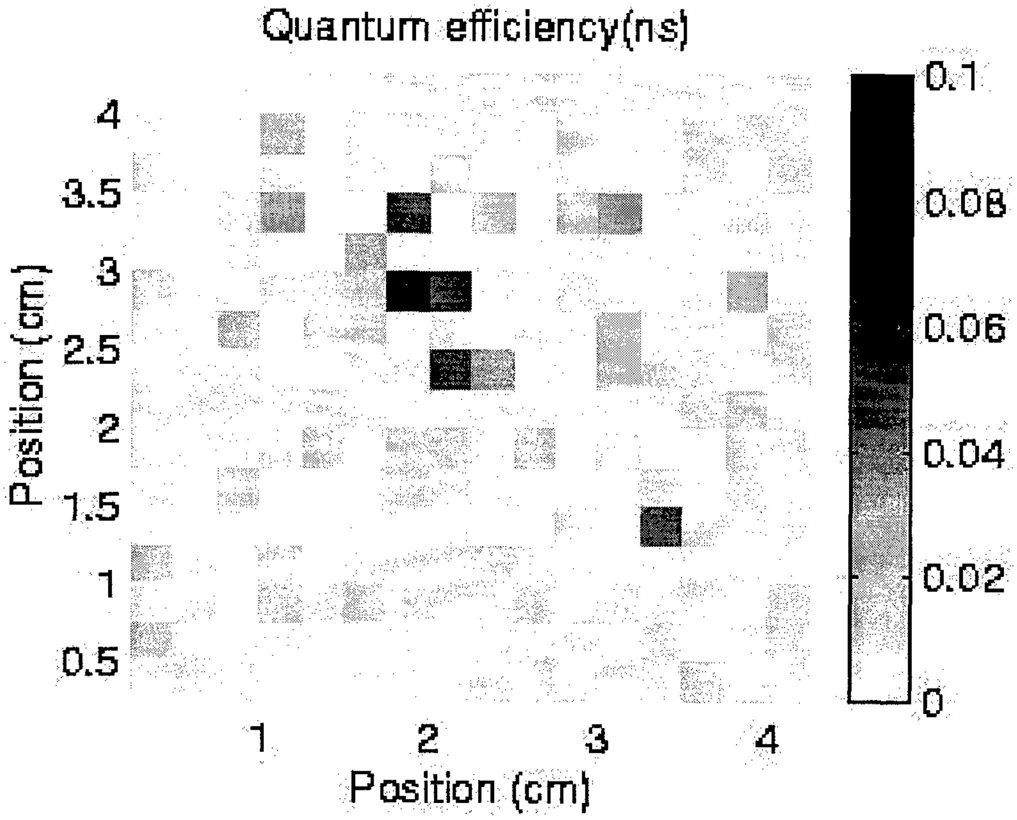
Quantum efficiency(ns)
4
3.5
3
2.5
2
1.5
1
0.5
Position (cm)
1
2
3
4
Position (cm)
0.1
0.08
0.06
0.04
0.02
0

Figure 4

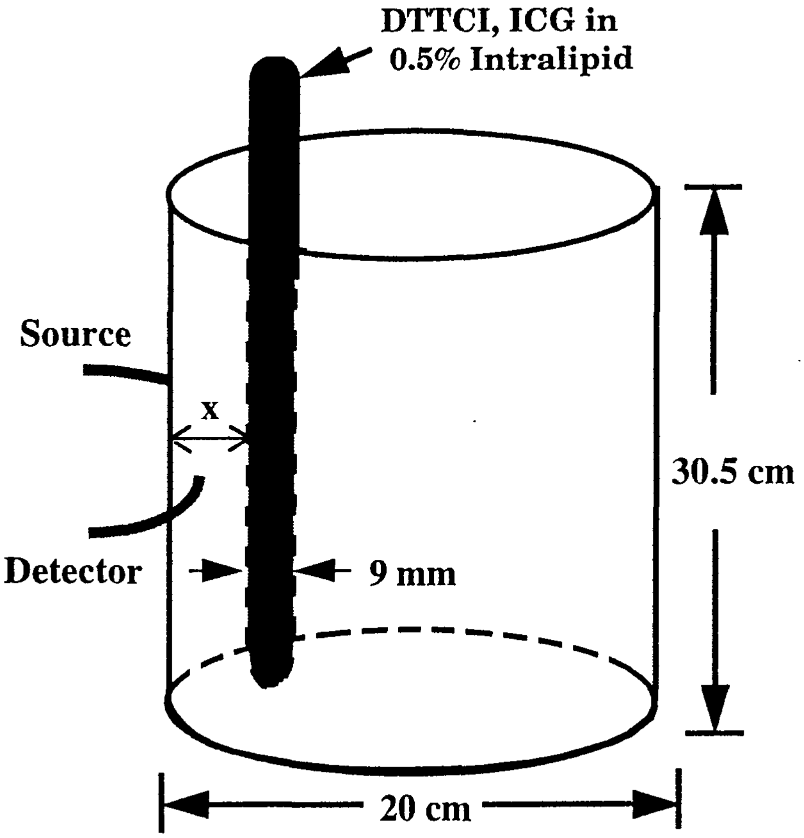
DTTCI, ICG in
0.5% Intralipid
Source
x
Detector
9 mm
30.5 cm
20 cm

Figure 5

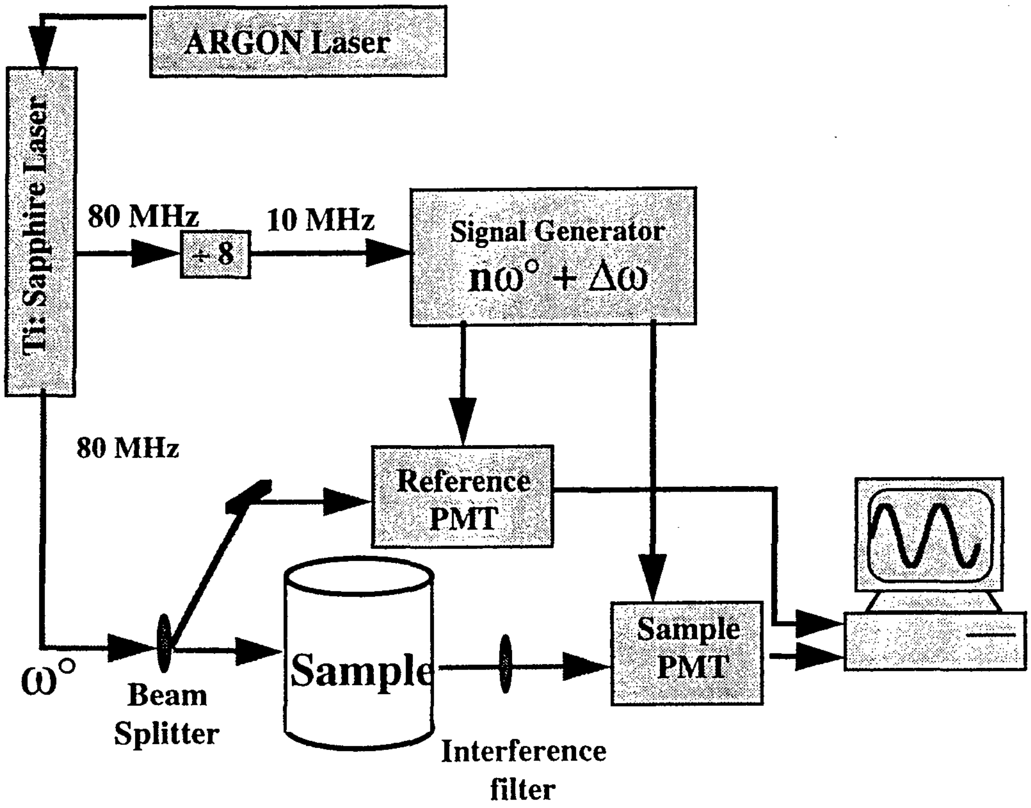
ARGON Laser
Ti: Sapphire Laser
80 MHz
÷ 8
10 MHz
Signal Generator
$n\omega^\circ + \Delta\omega$
80 MHz
Reference PMT
Sample
Sample PMT
ω°
Beam Splitter
Interference filter

Figure 6a

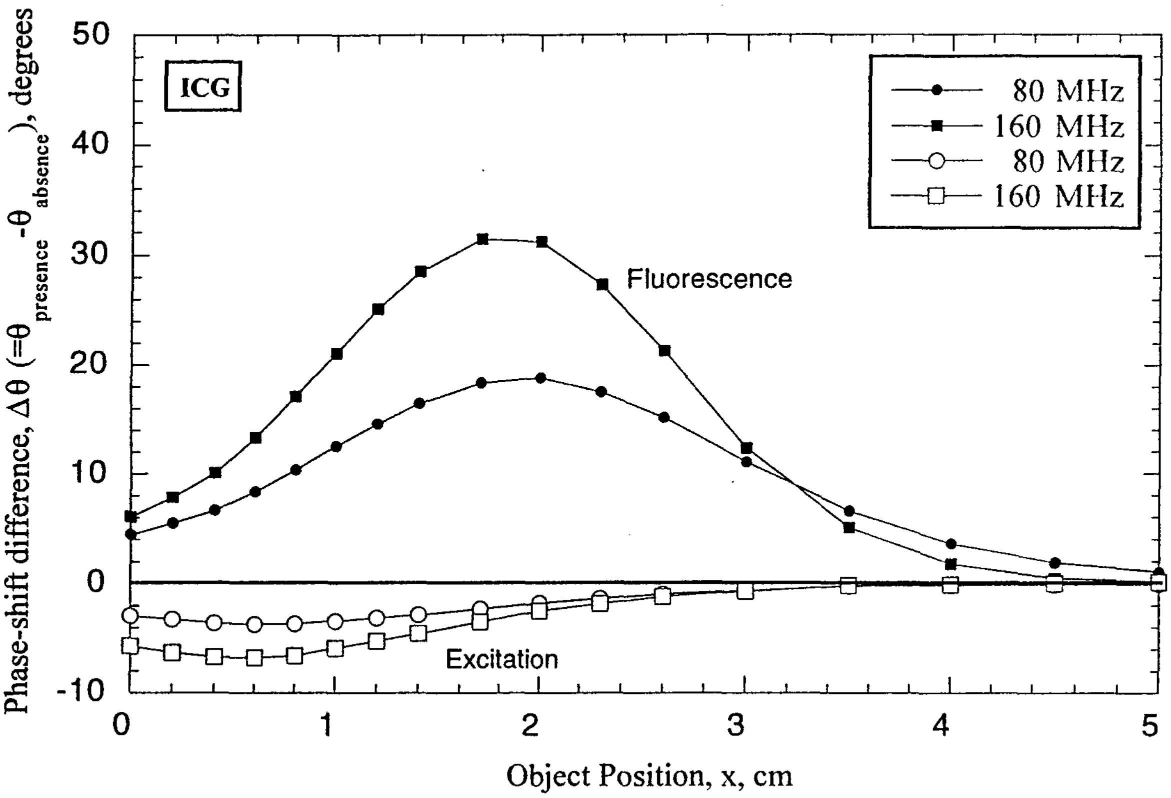
ICG
80 MHz
160 MHz
80 MHz
160 MHz
Fluorescence
Excitation
Phase-shift difference, Δθ (=θ presence -θ absence), degrees
50
40
30
20
10
0
-10
0
1
2
3
4
5
Object Position, x, cm

Figure 6b

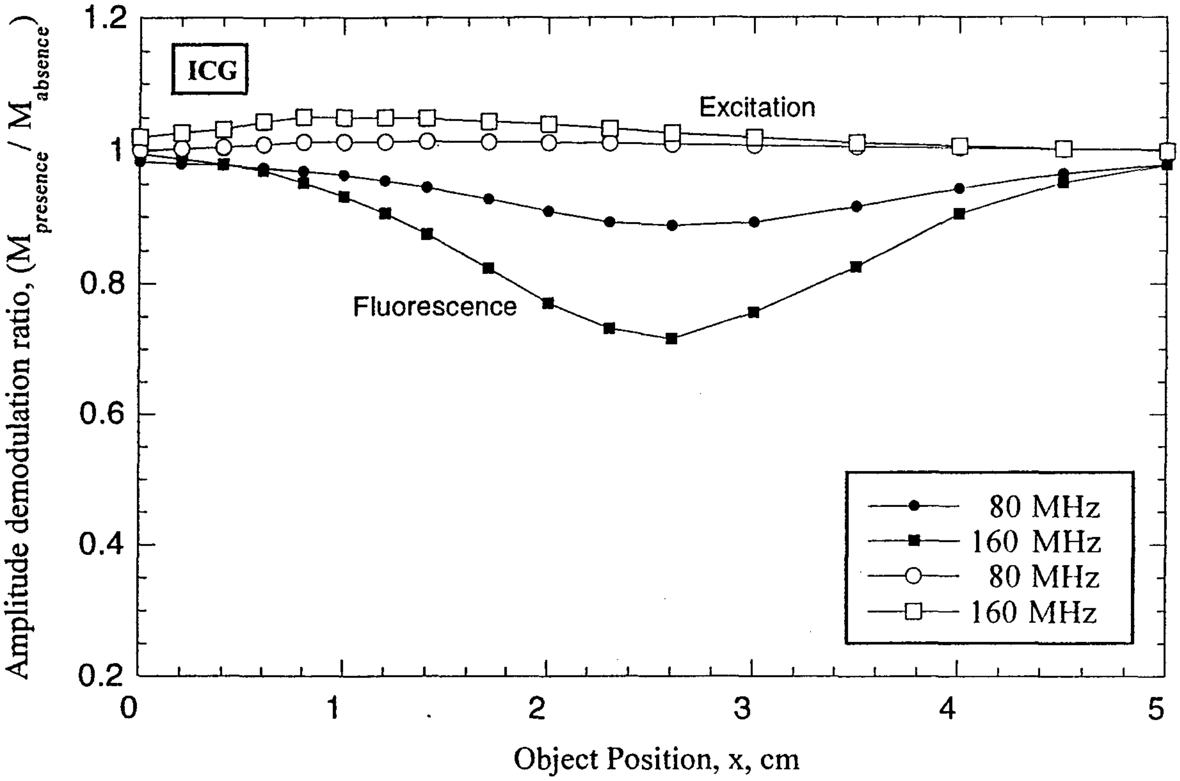
ICG
Excitation
Fluorescence
80 MHz
160 MHz
80 MHz
160 MHz
Amplitude demodulation ratio, ($M_{presence}$ / $M_{absence}$)
Object Position, x, cm
1.2
1
0.8
0.6
0.4
0.2
0
1
2
3
4
5

Figure 7a

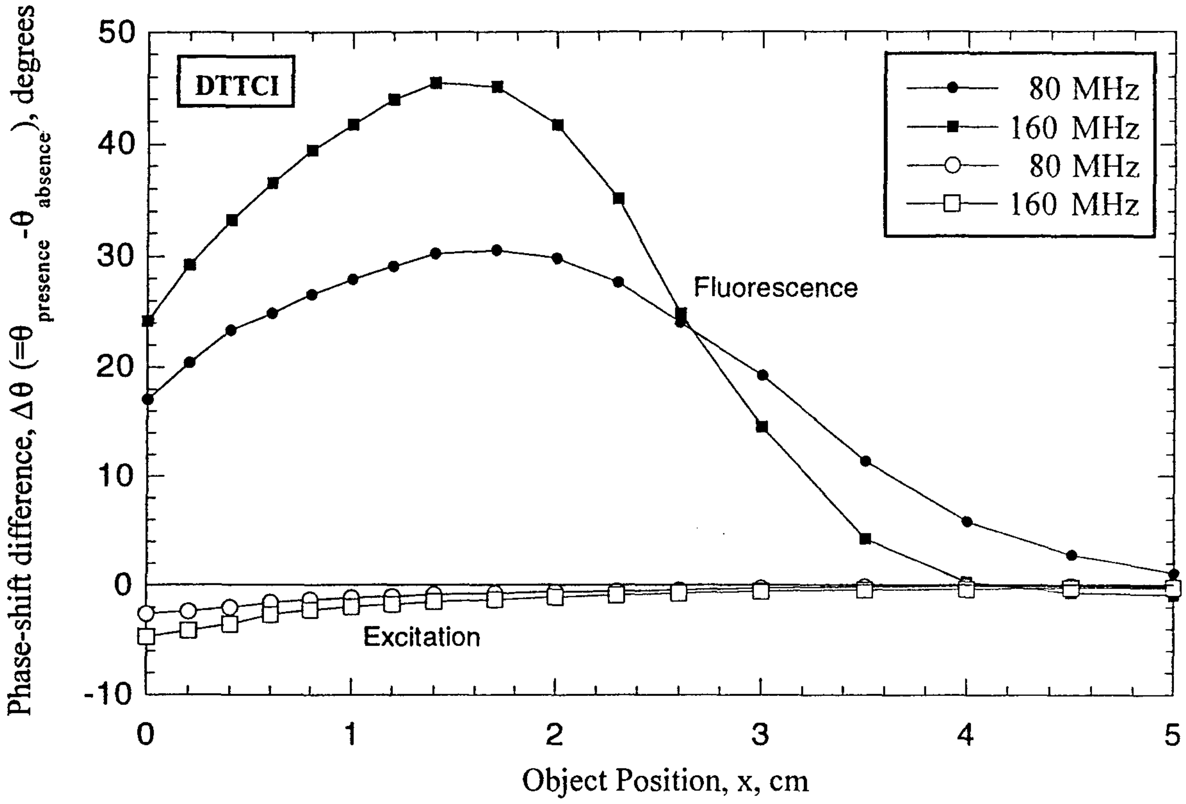

DTTCI
80 MHz
160 MHz
80 MHz
160 MHz
Fluorescence
Excitation
50
40
30
20
10
0
-10
0
1
2
3
4
5
Phase-shift difference, Δθ (=θ presence -θ absence), degrees
Object Position, x, cm

Figure 7b

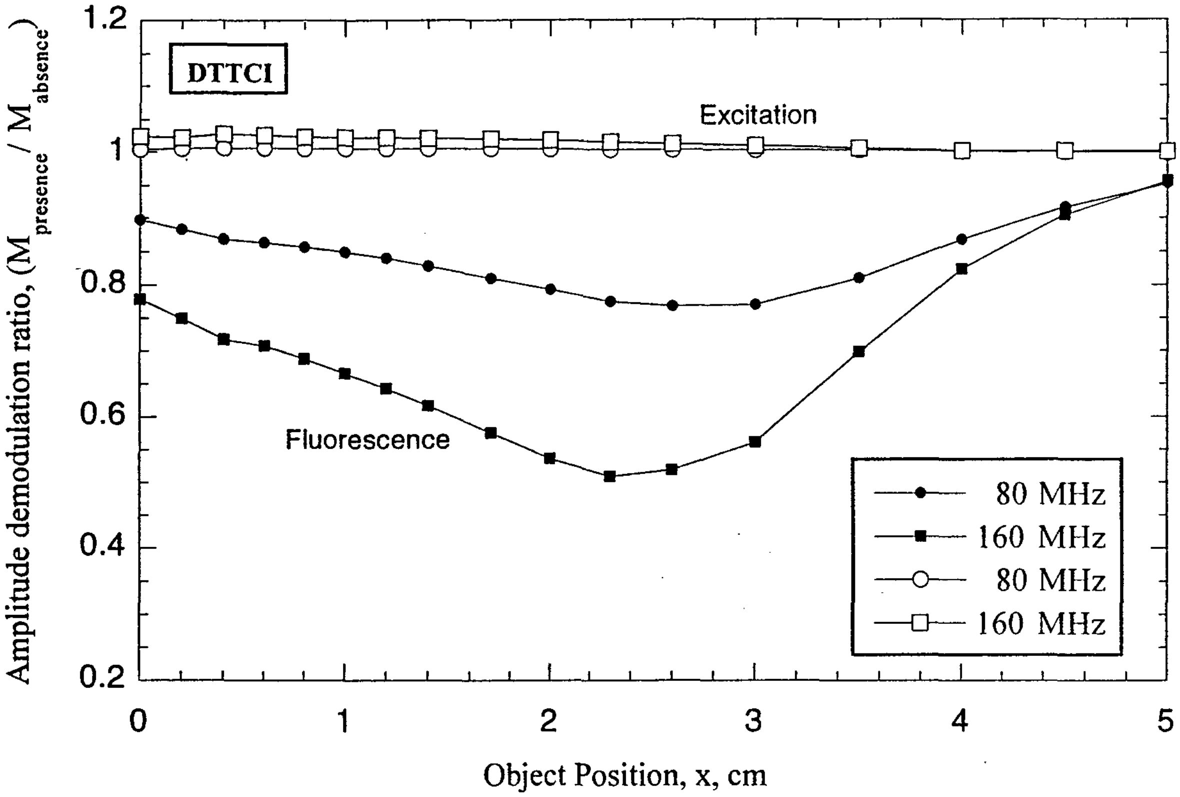
DTTCI
Excitation
Fluorescence
80 MHz
160 MHz
80 MHz
160 MHz
Amplitude demodulation ratio, ($M_{presence}$ / $M_{absence}$)
Object Position, x, cm
0.2
0.4
0.6
0.8
1
1.2
0
1
2
3
4
5

Figure 8a

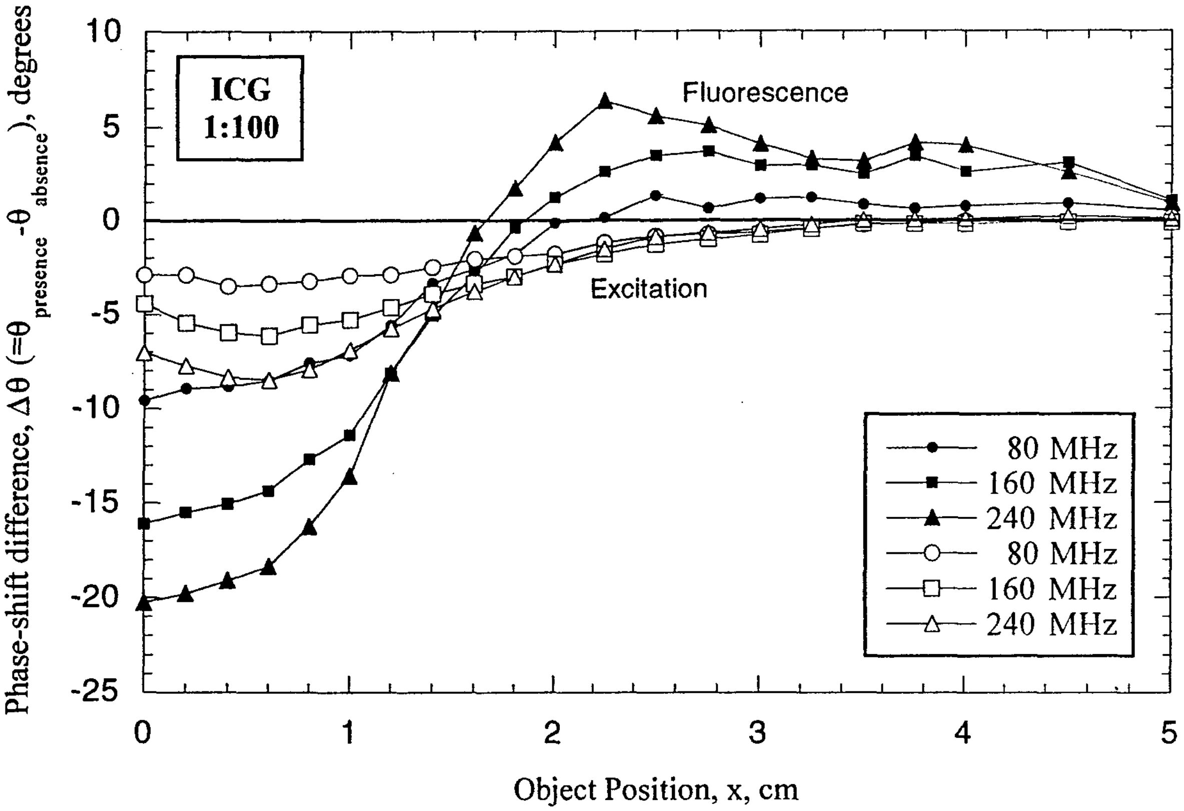

ICG
1:100
Fluorescence
Excitation
80 MHz
160 MHz
240 MHz
80 MHz
160 MHz
240 MHz
Phase-shift difference, Δθ (=θ presence -θ absence), degrees
Object Position, x, cm
10
5
0
-5
-10
-15
-20
-25
0
1
2
3
4
5

Figure 8b

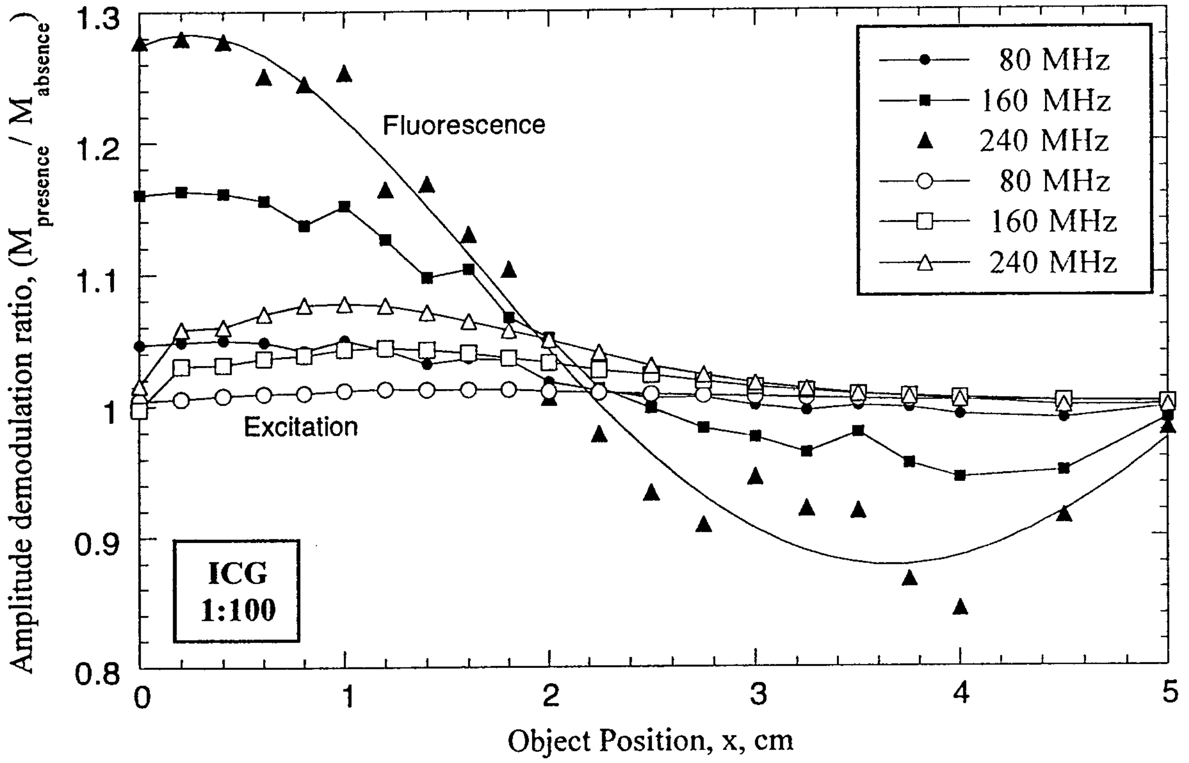

1.3
1.2
1.1
1
0.9
0.8
0
1
2
3
4
5
Amplitude demodulation ratio, ($M_{presence}$ / $M_{absence}$)
Object Position, x, cm
80 MHz
160 MHz
240 MHz
80 MHz
160 MHz
240 MHz
Fluorescence
Excitation
ICG
1:100

Figure 9a

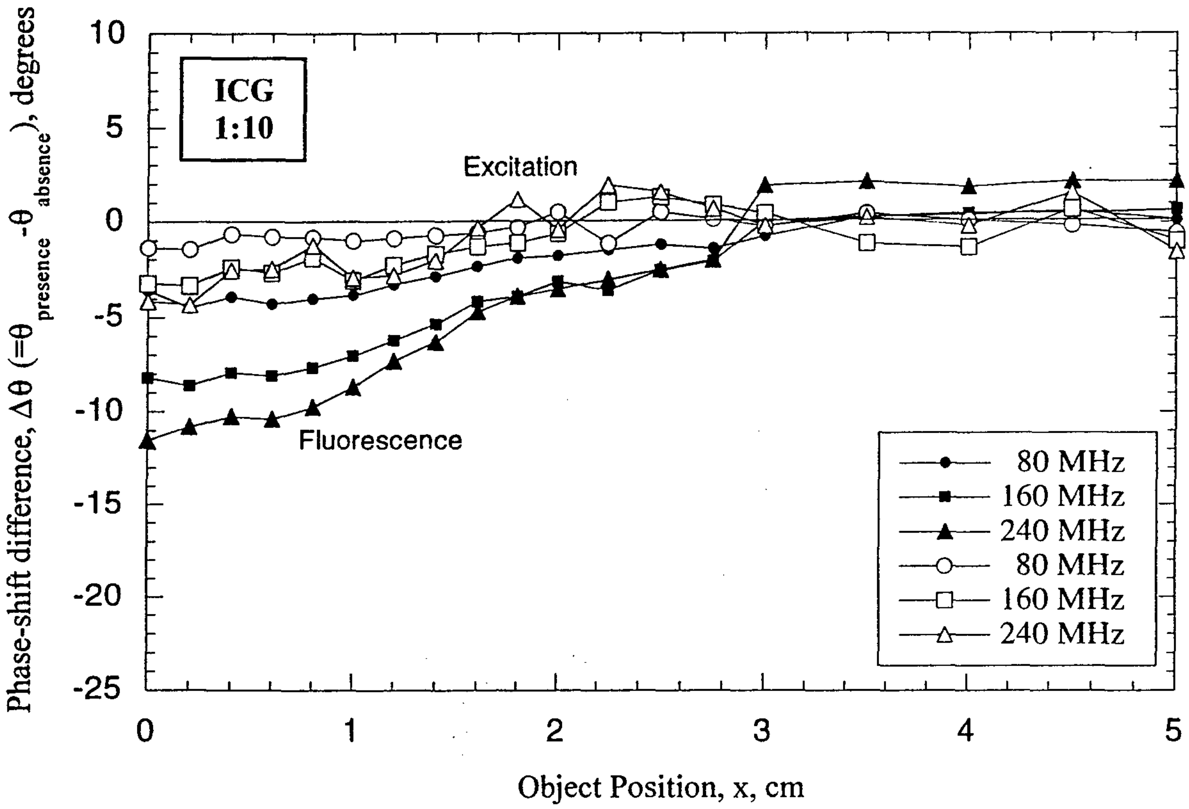
ICG
1:10
Excitation
Fluorescence
80 MHz
160 MHz
240 MHz
80 MHz
160 MHz
240 MHz
10
5
0
-5
-10
-15
-20
-25
0
1
2
3
4
5
Phase-shift difference, Δθ (=θ presence -θ absence), degrees
Object Position, x, cm

Figure 9b

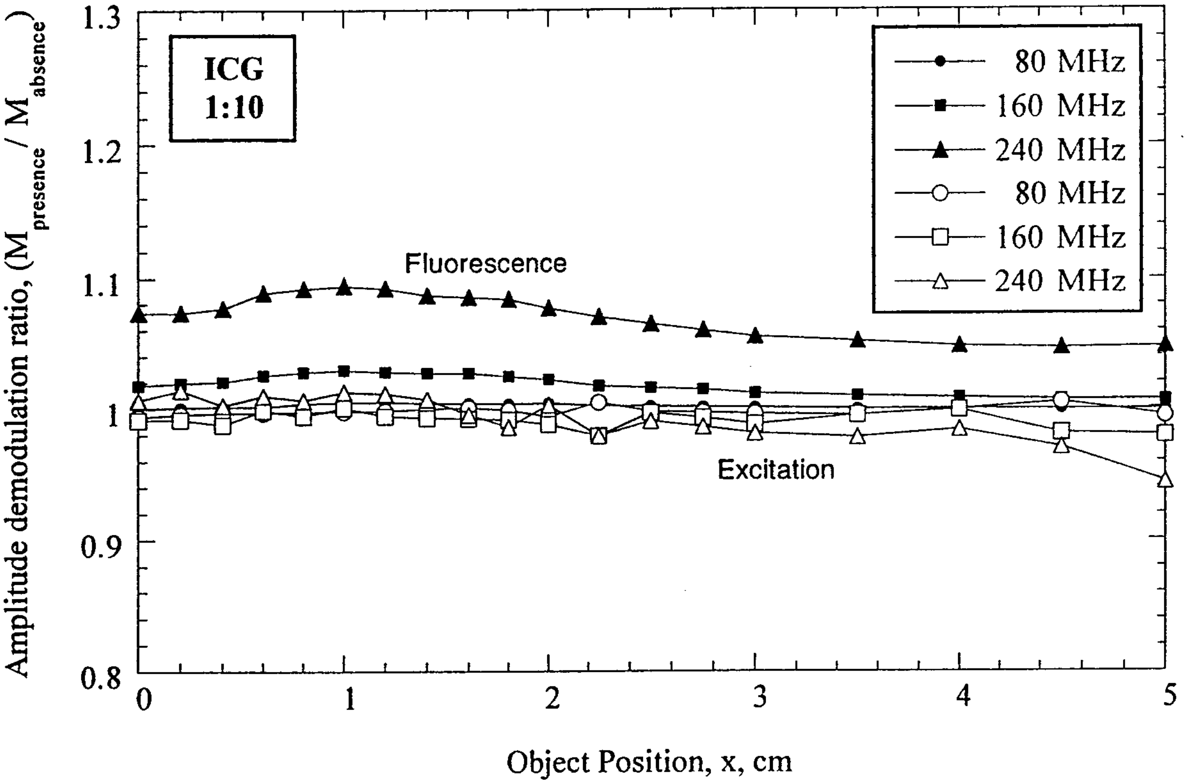
ICG
1:10
80 MHz
160 MHz
240 MHz
80 MHz
160 MHz
240 MHz
Fluorescence
Excitation
Amplitude demodulation ratio, ($M_{presence}$ / $M_{absence}$)
1.3
1.2
1.1
1
0.9
0.8
0
1
2
3
4
5
Object Position, x, cm

Figure 10a

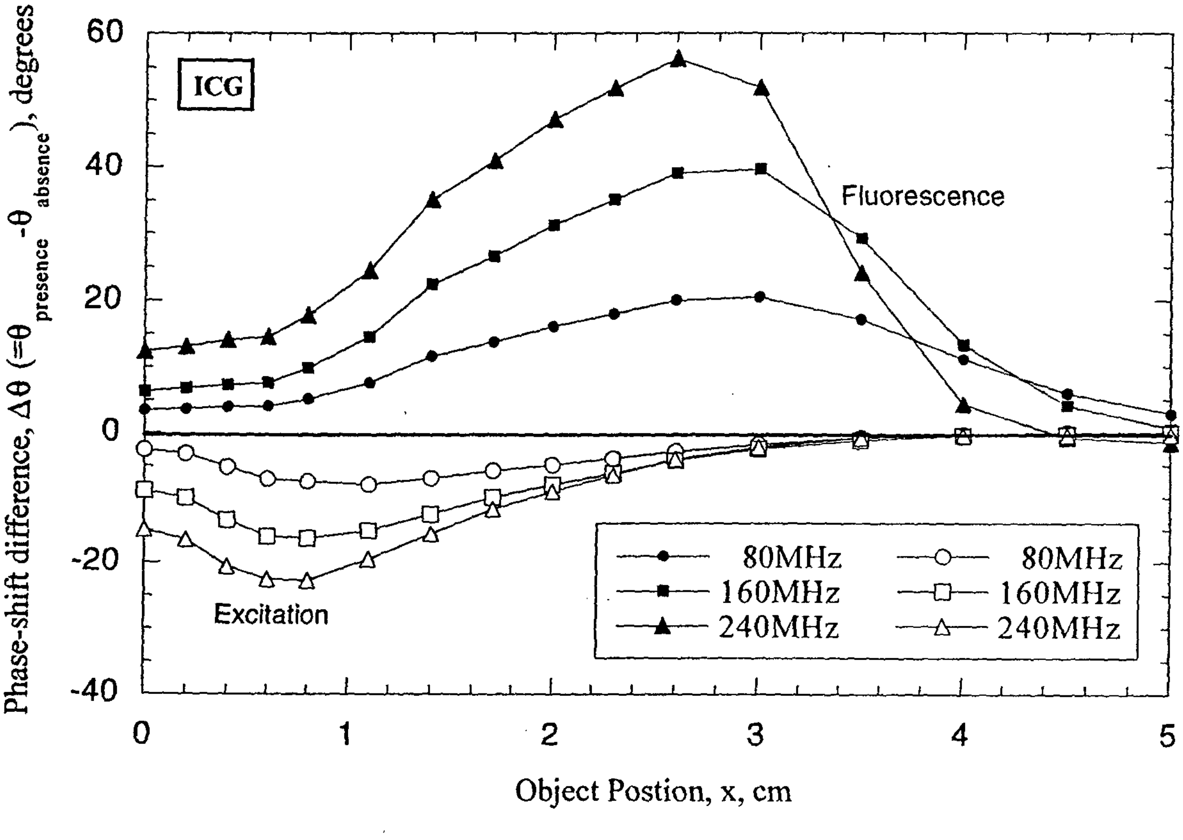
ICG
Fluorescence
Excitation
80MHz
160MHz
240MHz
80MHz
160MHz
240MHz
60
40
20
0
-20
-40
0
1
2
3
4
5
Phase-shift difference, Δθ (=θ presence -θ absence), degrees
Object Postion, x, cm

Figure 10b

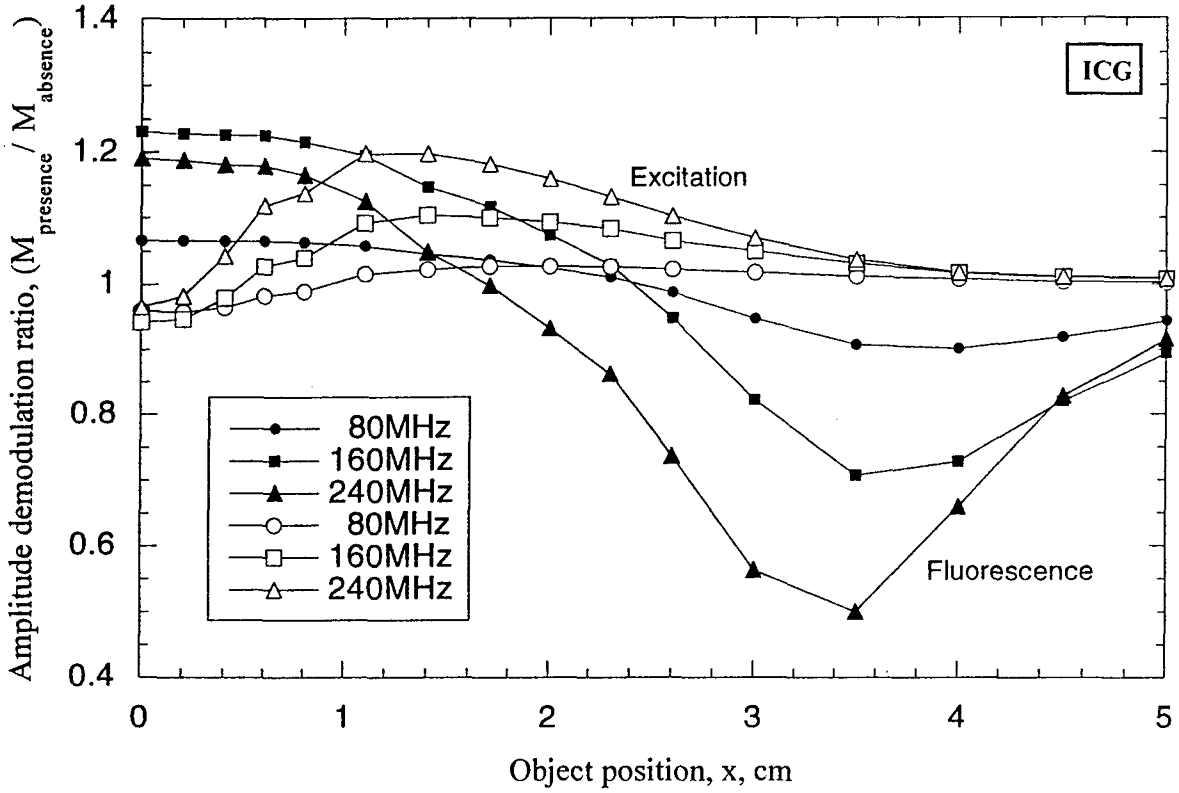

ICG
Excitation
Fluorescence
80MHz
160MHz
240MHz
80MHz
160MHz
240MHz
Amplitude demodulation ratio, ($M_{presence}$ / $M_{absence}$)
Object position, x, cm
1.4
1.2
1
0.8
0.6
0.4
0
1
2
3
4
5

Figure 11

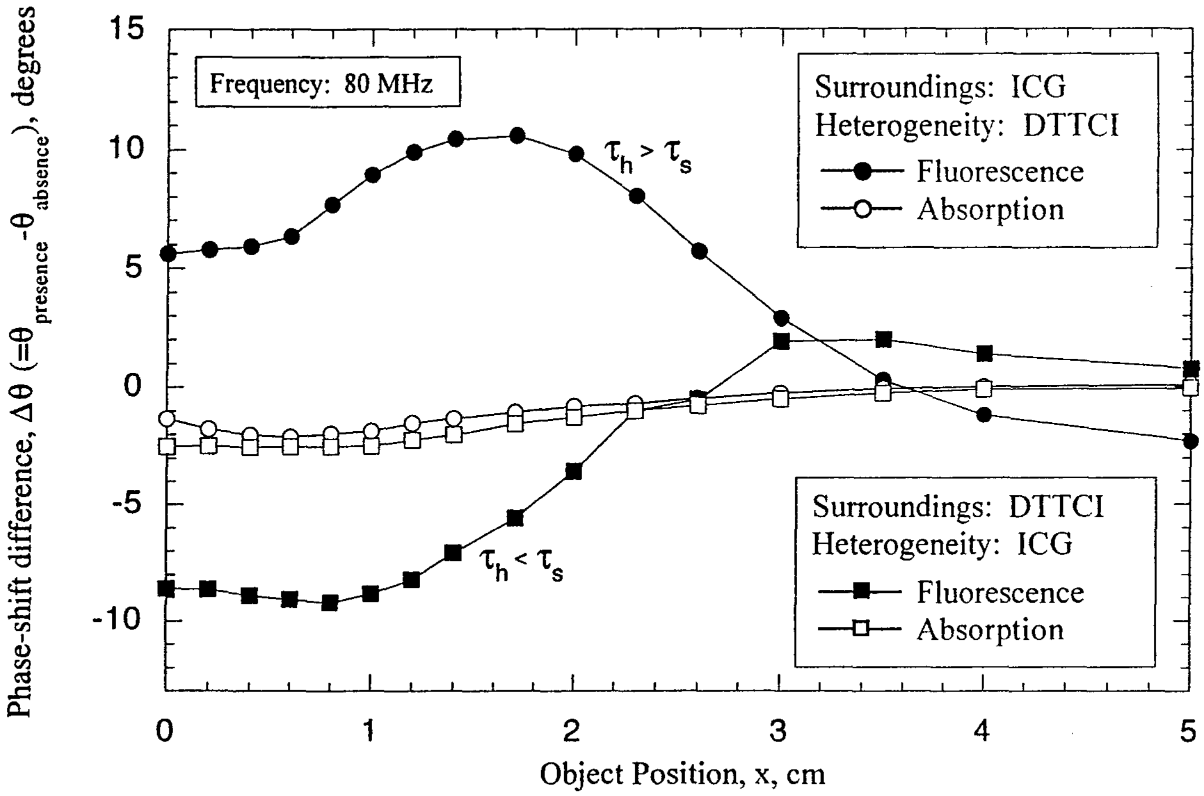

Phase-shift difference, $\Delta\theta$ (=$\theta_{presence}$-$\theta_{absence}$), degrees
15
10
5
0
-5
-10
Frequency: 80 MHz
Surroundings: ICG
Heterogeneity: DTTCI
● Fluorescence
○ Absorption
$\tau_h > \tau_s$
$\tau_h < \tau_s$
Surroundings: DTTCI
Heterogeneity: ICG
■ Fluorescence
□ Absorption
0
1
2
3
4
5
Object Position, x, cm

Figure 12

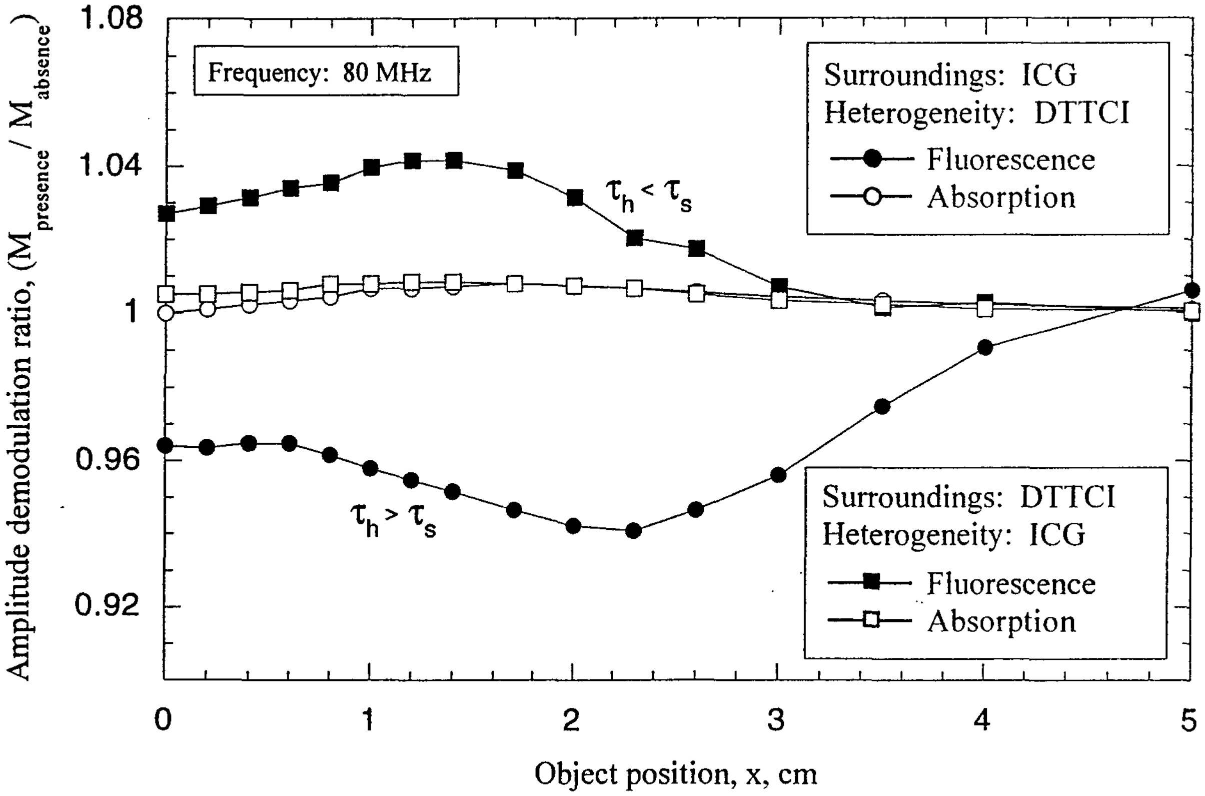

Frequency: 80 MHz
Surroundings: ICG
Heterogeneity: DTTCI
Fluorescence
Absorption
$\tau_h < \tau_s$
$\tau_h > \tau_s$
Surroundings: DTTCI
Heterogeneity: ICG
Fluorescence
Absorption
Amplitude demodulation ratio, ($M_{presence}$ / $M_{absence}$)
Object position, x, cm
1.08
1.04
1
0.96
0.92
0
1
2
3
4
5

Table 1

Dye	λ_x (nm)	λ_m (nm)	ε_{780} $(M*cm)^{-1}$	ε_{830} $(M*cm)^{-1}$	ϕ	τ (ns)
DTTCI	780	830	43,000	5,500	0.034	1.18
ICG	780	830	130,000	22,000	0.016	0.56

Table 2

Experiment	λ_x (nm)	λ_m (nm)	$[C]_{het}$ (μmol/L)	$[C]_{surr}$ (μmol/L)	$\mu_{a_{x-m}het}$ (cm^{-1})	$\phi_{het}\mu_{a_{x-m}het}$ (cm^{-1})
ICG Perfect Uptake	780	830	2.0	0	0.26	4×10^{-3}
DTTCI Perfect Uptake	780	830	4.2	0	0.18	6×10^{-3}
ICG 100:1 Uptake Ratio	780	830	2.3	0.023	0.30	5×10^{-3}
ICG 10:1 Uptake Ratio	780	830	2.3	0.23	0.30	5×10^{-3}
Perfect Absorber vs. Fluorescent Dye	780	830	3.0	0	0.39	6×10^{-3}
Heterogeneity: DTTCI Surroundings: ICG 100:1 Uptake Ratio	780	830	4.0	0.01	0.17	6×10^{-3}
Heterogeneity: ICG Surroundings: DTTCI 100:1 Uptake Ratio	780	830	1.0	0.04	0.13	2×10^{-3}

Imaging of fluorescent yield and lifetime from multiply scattered light reemitted from random media

D. Y. Paithankar, A. U. Chen, B. W. Pogue, M. S. Patterson, and E. M. Sevick-Muraca

The feasibility of employing fluorescent contrast agents to perform optical imaging in tissues and other scattering media has been examined through computational studies. Fluorescence lifetime and yield can give crucial information about local metabolite concentrations or environmental conditions within tissues. This information can be employed toward disease detection, diagnosis, and treatment if noninvasively quantitated from reemitted optical signals. However, the problem of inverse image reconstruction of fluorescence yield and lifetime is complicated because of the highly scattering nature of the tissue. Here a light propagation model employing the diffusion equation is used to account for the scattering of both the excitation and fluorescent light. Simulated measurements of frequency-domain parameters of fluorescent modulated ac amplitude and phase lag are used as inputs to an inverse image-reconstruction algorithm, which employs the diffusion model to predict frequency-domain measurements resulting from a modulated input at the phantom periphery. In the inverse image-reconstruction algorithm, a Newton–Raphson technique combined with a Marquardt algorithm is employed to converge on the fluorescent properties within the medium. The successful reconstruction of both the fluorescence yield and lifetime in the case of a heterogeneous fluorophore distribution within a scattering medium has been demonstrated without *a priori* information or without the necessity of obtaining absence images. © 1997 Optical Society of America

Key words: Fluorescence imaging, biomedical optics, image reconstruction, fluorescence lifetime, fluorescence yield.

1. Introduction

Over the past decade, several investigators have explored the use of exogenous fluorescent dyes as contrast agents to differentiate diseased and normal tissues from noninvasive or endoscopic optical measurements. The diagnosis of burn depth following Indocyanine Green dye administration[1] and the demarcation of neoplastic tissues following intravascular porphyrin dye administration[2–4] are possible because of their leakage from vessels corrupted by insult or disease. The concomitant increase in fluorescence from the dye can be detected at the tissue surface and permits the detection of disease. With the development of dyes and photodynamic agents that excite and reemit in the near-infrared red wavelength regime, the noninvasive detection of diseased tissues located deep within tissues may also be possible because red excitation and reemission light can travel significant distances to and from the tissue–air interface.[5] However, a long-standing problem has been the low uptake or leakage into neoplastic tissues, providing insufficient contrast for the detection of diseased tissues. Although targeted delivery may improve uptake ratios and contrast imparted by these otherwise therapeutic agents, these approaches have been elusive even in conventional imaging modalities such as magnetic resonance imaging (MRI) and x-ray computed tomography. Investigators have sought to alleviate the optical contrast uptake problem by employing dyes that fluoresce differently in diseased tissues than in normal tissues. The use of agents whose reemission characteristics vary with tissue pH[6,7] and pO_2[8] may not only provide detection of diseased tissues by the nature of differing fluores-

---

B. Pogue is with Wellman Laboratories of Photomedicine, Massachusetts General Hospital, Harvard Medical School, 50 Blossom Street, Boston, Massachusetts 02111. M. Patterson is with the Hamilton Regional Cancer Centre and McMaster University, 699 Concession Street, Hamilton, Ontario L8V 5C2, Canada. The other authors are with the School of Chemical Engineering, Purdue University, West Lafayette, Indiana 47907-1283.

Received 22 May 1996; revised manuscript received 5 September 1996.

0003-6935/97/102260-13$10.00/0

© 1997 Optical Society of America

cent properties but may also contain diagnostic information. The difficulty lies in measuring the multiply scattered reemitted light and reconstructing an image that differentiates tissues on the basis of fluorescent properties, such as fluorescent yield and lifetime.

In this study we investigate the combination of photon migration imaging techniques with fluorescence spectroscopy to examine the feasibility of fluorescence lifetime imaging (FLI).[9] FLI may be considered an optical analog to MRI. Whereas MRI depends on monitoring the spatial variation in the relaxation time of spin–spin states to provide high-resolution imaging in tissues, FLI depends on monitoring the spatial variation in the fluorophore lifetime and yield. The complication with FLI in tissues arises from the excitation and fluorescent photon times of flight, which are similar in magnitude to the fluorescence lifetime. Herein we combine inverse imaging techniques (as developed previously by Pogue *et al.*[10]) and fluorescence lifetime spectroscopy to demonstrate the feasibility of FLI by using computational studies. We separately introduce the concepts of photon migration imaging and fluorescence spectroscopy in Section 2 and then describe the combination of techniques in our computational approach to FLI. Our reconstructed images show the ability to image both fluorescence lifetime and fluorescence yield independent of any *a priori* information and point to the development of fluorescent dyes whose reemission characteristics are environmentally sensitive and provide contrast for the optical detection of diseased tissues.

2. Background: Photon Migration Imaging and Fluorescence Spectroscopy

The ability to reconstruct an internal map of absorption optical properties from continuous wave[11] and absorption and scattering properties from frequency-domain[10,12,13] measurements has been successfully demonstrated by using multiply scattered light from random media. Continuous wave measurements consist of noninvasively monitoring the attenuation of light as a function of position around the periphery of a heterogeneous tissue phantom model in response to a constant intensity source, whereas frequency-domain measurements consist of monitoring the phase and amplitude modulation of multiply scattered light at various peripheral positions in response to an incident modulated light source. Both approaches employ a perturbation analysis whereby the absorption and scattering properties at each pixel position within the tissue phantom are individually and independently adjusted until the measurements of reemitted light at the periphery of the tissue phantom match those predicted by a model for diffusive light propagation in random media. These studies show the potential for image reconstruction of hidden tissue heterogeneities when the contrast caused by either absorption or scattering coefficients is as low as 2:1.[13] However, Troy *et al.*[14] conducted *in vitro* measurements of normal and diseased breast tissues and showed that the endogenous optical contrast between 120 normal and diseased breast tissues is not significantly different for consistent detection with optical techniques. These measurements were conducted *ex vivo* and consequently may underestimate the contrast available *in vivo* caused by increased tumor vasculature and absorption caused by hemoglobin. Nonetheless, these results suggest the need for optical contrast agents.

Previously, we experimentally demonstrated the increased sensitivity for detecting heterogeneities on the basis of fluorescence as opposed to absorption when time-dependent measurements are employed.[15] Indeed, the augmentation of optical contrast that is due to the lifetime of a fluorophore or phosphorescent probe has been recognized by Wu *et al.*[16] in tissue phantom studies. The localization of a fluorescing body has been performed by various researchers.[17–19] Upon activation into a higher electronic state by the absorption of light, an activated fluorophore may undergo nonradiative decay or radiative decay; the latter results in the reemission of a fluorescent photon. The yield is defined by the fractional number of fluorescent photons reemitted for each excitation photon absorbed or the fraction of decay events that results in the emission of a fluorescent photon. The lifetime is defined as the mean survival time of the activated fluorophore or the mean time between the absorption of an excitation photon and the reemission of a fluorescent photon. Because the stability of the activated fluorophore depends on its environment, both yield and lifetime are also dependent on the (bio) chemical environment in which the fluorophore resides. Consequently, the lifetime can provide contrast based on the differences in biochemical environments of normal and diseased tissues, similar to the contrast provided by relaxation times in nuclear magnetic resonance imaging.

The use of lifetime for contrast in optical imaging in tissues is not new. In studies demonstrating the noninvasive differentiation of hematoporphyrin-laden tumors from normal tissue, Cubeddu *et al.*[20] employed the comparatively long lifetime ($>$15 ns) of reemitted fluorescence caused by increased porphyrin uptake in tumors over the lifetime of endogenous compounds ($>$7 ns) in normal tissues in order to provide discrimination of the two tissue types. These microscopy studies involved unscattered light that provided correct reemission kinetics of measured fluorescence. In this computational study, we employ contrast that is due to increased uptake as well as lifetime in order to differentiate diseased tissue by using multiply scattered light reemitted from tissues that involve deeply seated tissue volumes. The reemission kinetics of phosphorescent probes do not permit an interrogation deep into tissue with time-domain approaches.[21] Our preliminary frequency-domain computations (unpublished) suggest that the simultaneous determination of location and lifetime is difficult when long-lived phosphorescent probes are used. In Section 3 we underscore the magnitude of the problem by describing the forward imaging problem (i.e., prediction of the frequency-domain measurements given the location, optical properties, and fluorescent properties of the random media) as well as our adapted approach for solving the inverse problem (i.e., prediction of the location, optical properties, and fluorescent properties of the medium from measurements of frequency-domain light propagation).

3. Forward Problem and the Solution Methodology

The spatial and temporal transport of light in tissues or multiply scattering media can be accurately described by the diffusion approximation to the radiative transport equation. A coupled frequency-domain diffusion equation can be used to predict the excitation and emission fluence rates, $\Phi_x(r, \omega)$ and $\Phi_m(r, \omega)$, at any location r within a tissue phantom by Eqs. (1) and (2), respectively.[22–24]

$$\nabla \cdot [D_x(r)\nabla\Phi_x(r, \omega)] - [\mu_{a_x}(r) + i\omega/c_n] \times \Phi_x(r, \omega) + S_x(r, \omega) = 0, \quad (1)$$

$$\nabla \cdot [D_m(r)\nabla\Phi_m(r, \omega)] - [\mu_{a_m}(r) + i\omega/c_n] \times \Phi_m(r, \omega) + S_m(r, \omega) = 0. \quad (2)$$

The source term for excitation light $S_x(r, \omega)$ is due to the sinusoidally modulated light at frequency $\omega = 2\pi f$, where f is usually in the megahertz range. The first term in both equations represents the diffusive or random-walk transport of light where $D_{x,m}$ is the optical diffusion coefficient, i.e.,

$$D_{x,m} = [3(\mu_{a_{x,m}} + \mu_{s_{x,m}}{}')]^{-1}, \quad (3)$$

and μ_a and $\mu_s{}'$ are the absorption and isotropic scattering coefficients, respectively. The optical properties are dependent on the wavelength of light and thus are different for the excitation (subscript x) and fluorescent (subscript m) light. The total absorption coefficient at the excitation wavelength, μ_{a_x}, is due to contributions from nonfluorescing chromophores as well as from fluorescent dye. The total absorption coefficient is given by the sum of absorption coefficients that are due to nonfluorescing chromophores, $\mu_{a_{x\to}}$, and fluorophores, $\mu_{a_{x\to m}}$. We assume that the absorption experienced at the fluorescent wavelength primarily is due to nonfluorescing chromophores. The velocity of light in tissue is $c_n = c/n$, where n is the average index of refraction. The source term for the fluorescent light is dependent on the excitation light fluence, $\Phi_x(r, \omega)$, and is given by

$$S_m(r, \omega) = \eta\mu_{a_{x\to m}}(r)\Phi_x(r, \omega)\,\frac{1 - i\omega\tau(r)}{1 + \omega^2\tau(r)^2}. \quad (4)$$

This term arises from the Fourier transform of the single-exponential fluorescence decay term $(1/\tau)\exp(-t/\tau)$ in the time domain following an incident pulse of excitation light where τ is the fluorophore lifetime. Here η is the quantum yield and the absorption coefficient, $\mu_{a_{x\to m}}$, is the product of the extinction coefficient, $\log_e 10$, and the concentration of the fluorophore in the ground state. For the purposes of this study, the combined product, $\eta\mu_{a_{x\to m}}$, is termed the fluorescent yield and is proportional to the generated fluorescence fluence. Note that multiexponential time decay can also be handled with this procedure by a simple extension.

In the source term for fluorescent light given in Eq. (4), $\mu_{a_{x\to m}}$ changes as the relative fractions of the fluorophore in the ground and excited states change. The saturation effects would have to be handled by taking into account the relative amounts of fluorophore in the ground and excited states. We neglect the saturation effects and assume single-exponential decay kinetics in this initial study.

Furthermore, μ_{a_x} in Eq. (1) is the sum of $\mu_{a_{x\to}}$ and $\mu_{a_{x\to m}}$. In what follows, images of lifetime, τ, and images of $\eta\mu_{a_{x\to m}}$ are obtained. There is a difficulty in the estimation of μ_{a_x} that is given by $\mu_{a_x} = \mu_{a_{x\to}} + \mu_{a_{x\to m}}$, because the explicit values of $\mu_{a_{x\to m}}$ are not known (the values of the product of η and $\mu_{a_{x\to m}}$ are known). Because the major contribution to μ_{a_x} is from $\mu_{a_{x\to}}$ and not $\mu_{a_{x\to m}}$, we have used an approximate expression for μ_{a_x}, $\mu_{a_x} = \mu_{a_{x\to}} + \eta\mu_{a_{x\to m}}$ and have chosen η as 1 only for the purposes of calculation of μ_{a_x}. Our approach can be extended to permit imaging of η, $\mu_{a_{x\to m}}$, $\mu_{a_{x\to}}$, and τ from measurements conducted at both excitation and fluorescent wavelengths. Although reconstruction from fluorescent measurements provides $\eta\mu_{a_{x\to m}}$, excitation measurements can provide $\mu_{a_{x\to}}$ (in the absence of a fluorophore) and $\mu_{a_{x\to m}} + \mu_{a_{x\to}}$ (in the presence of a fluorophore). From these images, maps of η and $\mu_{a_{x\to m}}$ can be obtained in principle.

Both Eqs. (1) and (2) are linear complex elliptic equations that can be solved as boundary value problems for complex quantities $\Phi_x(r, \omega)$ and $\Phi_m(r, \omega)$. We employ the method of finite differences in which we place a grid over the space domain and obtain an approximation to the solution at each grid point, j. One of the fastest methods to solve these linear elliptic boundary value problems is the multigrid solution (see the review by Fulton *et al.*[25]). In the procedure for the multigrid solution, an initial solution is obtained quickly for coarse grids that is then further refined for a better solution for finer grids. This is an involved procedure in which we have elected to use MUDPACK routines.[26] MUDPACK routines are flexible and allow placement of sources either at the surface or inside the phantom. For the equations to be solved, it is assumed that $\Phi_{m,x}(r, \omega) = 0$ on the tissue surface, which is known as the zero-fluence boundary condition. This is implemented by assigning the absorption coefficient for both excitation and fluorescent light at all the grid points in the square grid lying outside the circular tissue phantom to a large value. The source was simulated by setting the value of Φ_x to an arbitrary complex number at a grid point on the surface where the source is located. The solution of Eqs. (1) and (2) yields a complex number for Φ_m at each grid point, j. The detected signal at the surface is proportional to the normal component of the gradi-

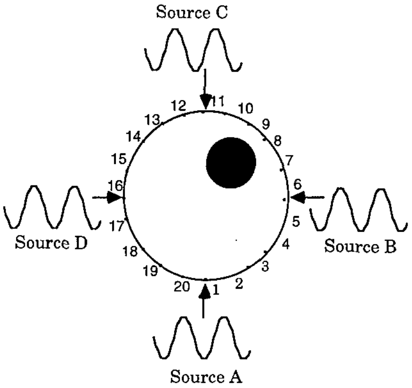

Fig. 1. Schematic of the circular simulated tissue phantom interrogated by four sources, one source at a time. Twenty detectors are located on the periphery with uniform separation. A circular object that mimics a hidden diseased tissue volume, located within the tissue phantom, is also shown.

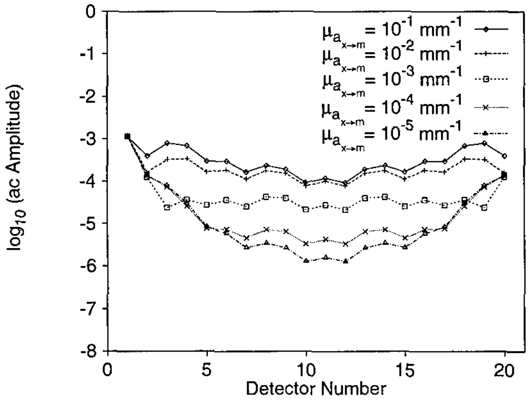

Fig. 2. Log plot of fluorescent light ac amplitude at 150 MHz at various detectors for a heterogeneous tissue phantom with a 30-mm-diameter object located at the center of the phantom for various object $\eta\mu_{a_{x\to m}}$ values. Absorption coefficient $\eta\mu_{a_{x\to m}}$ is 1×10^{-5} mm^{-1} for the background; lifetimes τ for both the object and the background are 1 ns.

ent. In this study, for evaluation of the signal at detector i located on the surface, we used the value of Φ_m at an internal grid point closest to the detector. This is reasonable in our initial approach because the normal component of the gradient is proportional to Φ_m just inside the surface.[10] The phase lag, θ_M, and the log of the ac amplitude, M_m, at the detectors were calculated with respect to the phase and the ac amplitude of the source. The computational time required to solve for the fluorescent fluence on a SunSparc 10 for a 17 × 17 grid is 0.04 s, and that for a 33 × 33 grid is 0.165 s. Different grid sizes were used in the testing phase of the solution of the equations, and the solutions were in agreement within the numerical error caused by the finite grid size.

Before attempting to solve the inverse problem for the simulated phantom illustrated in Fig. 1, we must first understand the effects of changing the fluorescent optical properties of the tissue on θ_m and M_m measured at a detector or series of detectors located on its surface. Solutions to Eqs. (1) and (2) were obtained in two dimensions for a 65 × 65 grid covering a 100-mm-diameter circular tissue phantom with a circular embedded heterogeneity of 30 mm diameter and located at the center of the tissue phantom. The simulated measurements of fluorescent phase shift and ac amplitude are reported for 20, equally spaced, circumferentially located detectors. The modulation frequency, f, was set equal to 150 MHz. The optical properties of the heterogeneity and the background are shown in Table 1.

A. Effect of $\eta\mu_{a_{x\to m}}$ on θ_m and M_m

In order to evaluate the influence of $\eta\mu_{a_{x\to m}}$, θ_m and M_m were computed at each detector as the value of $\eta\mu_{a_{x\to m}}$ in the heterogeneity increased from 10^{-4} mm^{-1} to 10^{-1} mm^{-1} and as $\eta\mu_{a_{x\to m}}$ in the background was maintained constant. The modulation frequency was chosen as 150 MHz. The lifetime, τ, was set equal to 1 ns for both the object and the background causing contrast resulting solely from differences in $\eta\mu_{a_{x\to m}}$. The plots of θ_m and M_m are shown in Figs. 2 and 3, respectively, for one source located at position A. The curves for M_m are not smooth because the circular surface is approximated by joining discrete grid points closest to the circumference by straight lines. Furthermore, the curves for both θ_m and M_m are symmetric for detectors 2 and 20, 3 and 19, 4 and 18, and so on because these detector pairs are symmetric with respect to the source. The detectors near the source are unaffected by the presence of an object because the photon sampling volume does not include the region occupied by the heterogeneity. At the other detector locations, the fluorescent ac amplitude increases as $\eta\mu_{a_{x\to m}}$ of the heterogeneity increases. As $\eta\mu_{a_{x\to m}}$ of the heterogeneity increases to high values, the ac amplitude approaches an upper limit that is due to high absorption coefficient μ_{a_x}, which is a sum of $\mu_{a_{x\to m}}$ and $\mu_{a_{x\to}}$. This is similar to the inner-filter effect in which the high absorption in the heterogeneity shields the interior of the heterogeneity from excitation photons.[27] Figure 3 illustrates changes in fluorescent phase shift, θ_m, as a

Table 1. Optical Properties and Experimental Parameters for the Forward Problem

μ_{a_x} (mm^{-1})	μ_{a_m} (mm^{-1})	$\mu_{s_x}{}'$ or $\mu_{s_m}{}'$ (mm^{-1})	$\mu_{a_{x\to}}$ (mm^{-1})	$\eta\mu_{a_{x\to m}}$ Background (mm^{-1})	τ Background (ns)	Frequency (MHz)
$\mu_{a_{x\to}} + \mu_{a_{x\to m}}$	0.0	1.0	0.0	1.0×10^{-5}	1.0	150.0

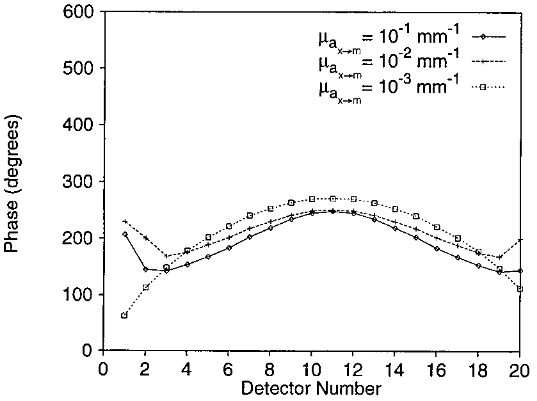

Fig. 3. Plot of fluorescent light phase shift at 150 MHz at various detectors for a heterogeneous tissue phantom with a 30-mm-diameter object located at the center of the phantom for various object $\eta\mu_{a_{x\to m}}$ values. Absorption coefficients and lifetimes are the same as in Fig. 2.

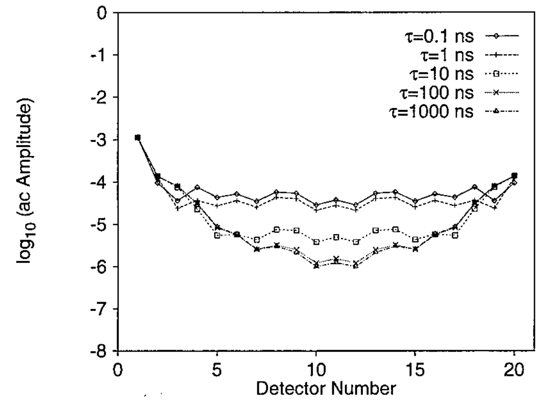

Fig. 4. Log plot of fluorescent light ac amplitude at 150 MHz at various detectors for a heterogeneous tissue phantom with a 30-mm-diameter object located at the center of the phantom for various object τ values. Background lifetime τ is 1 ns and absorption coefficients $\eta\mu_{a_{x\to m}}$ are 1×10^{-5} mm^{-1} for the background and 1×10^{-3} mm^{-1} for the object.

function of the fluorescent yield that is due to the fluorophore, $\eta\mu_{a_{x\to m}}$. As $\eta\mu_{a_{x\to m}}$ is increased from 10^{-3} mm^{-1} to 10^{-1} mm^{-1} (when the background value is 10^{-5} mm^{-1}), little change in phase shift occurs. Because the phase shift of reemitted fluorescence in dilute, nonscattering solutions is a function of lifetime and is not dependent on concentration [$\theta \sim \tan^{-1}(\omega\tau)$], one might expect similar trends in scattering media. Indeed, as shown in Fig. 3, phase-shift changes caused by fluorophore concentration differences are small. Consequently, the changes in phase shift with increasing $\eta\mu_{a_{x\to m}}$ of the heterogeneity can be attributed to the alteration in photon migration as a result of the presence of heterogeneities with a high absorption of excitation light.[28] The presence of heterogeneities with high absorption reduces the effective path length of photon migration and reduces the phase shift, though this reduction is small in magnitude. In summary, M_m is directly and strongly dependent on changes in $\eta\mu_{a_{x\to m}}$ of a simulated tissue heterogeneity, whereas θ_m is indirectly and weakly dependent on $\eta\mu_{a_{x\to m}}$ because of changes in photon migration.

B. Effect of τ on M_m and θ_m

In order to evaluate the influence of τ, M_m and θ_m were calculated at each detector as the values of τ in the heterogeneity varied from 10^{-1} ns to 10^{3} ns and the value of τ in the background was held at 1 ns. The modulation frequency was at 150 MHz. Background $\eta\mu_{a_{x\to m}}$ was set to 10^{-5} mm^{-1}, and $\eta\mu_{a_{x\to m}}$ for the object was set to 10^{-3} mm^{-1}. As shown in Fig. 4, the detected ac amplitude increases as τ decreases. Because M_m of reemitted fluorescence in a dilute, nonscattering solution is a function of lifetime (and also fluorophore concentration), one would expect that in the presence of scatter, similar trends would be observed. Figure 5 illustrates the values of the fluorescent phase shift at each detector as the lifetime of the heterogeneity is changed from 0.1 ns to 1000 ns. At the given modulation frequency (150 MHz in this calculation), θ_m first increases, reaches a maximum, and then subsequently decreases as τ is increased from 0.1 ns to 1000 ns. There is a complex interplay of the signal coming from the object for which we are changing the lifetime and the signal from the background that leads to the behavior described. In summary, both M_m and θ_m at each detector are directly and strongly influenced by the value of lifetime in the heterogeneity.

Detailed analytical expressions for fluorescence amplitude and phase shift for infinite and semi-infinite media with spherical heterogeneities have been provided by Li *et al.*[29] Our numerical computational methods provide a simulation of finite media and arbitrary shaped hidden objects. Our numerical results agree with the general predictions provided by Li *et al.*[29]

The solution of the forward problem was used as inputs to the solution of the inverse problem de-

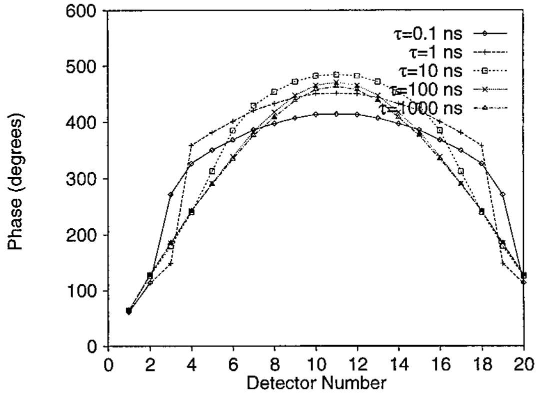

Fig. 5. Plot of fluorescent light phase shift at 150 MHz at various detectors for a heterogeneous tissue phantom with a 30-mm-diameter object located at the center of the phantom for various object τ values. Background lifetime τ is 1 ns and absorption coefficients $\eta\mu_{a_{x\to m}}$ are 1×10^{-5} mm^{-1} for the background and 1×10^{-3} mm^{-1} for the object.

Table 2. Optical Properties Used to Generate the Simulated Experimental Data as Inputs to the Inverse Image-Reconstruction Algorithm

Case	$\mu_{a_{x\to}}$ (mm^{-1})	μ_{a_m} (mm^{-1})	$\mu_{s_x}{}'$ or $\mu_{s_m}{}'$ (mm^{-1})	τ Background (ns)	$\eta\mu_{a_{x\to m}}$ Background (mm^{-1})	σ_M Gaussian Noise in Log of ac Amplitude	σ_θ Gaussian Noise in Phase (deg)
5.A	0.0	0.0	1.0	10.0	1.0×10^{-5}	0.01	0.1
5.B	1.0×10^{-3}	1.0×10^{-3}	1.0	10.0	1.0×10^{-5}	0.01	0.1
5.C	0.0	0.0	1.0	10.0	1.0×10^{-5}	0.01	1.0
5.D	1.0×10^{-3}	1.0×10^{-3}	1.0	10.0	1.0×10^{-5}	0.01	0.1

scribed in Section 4. Forward solutions in two dimensions were computed for the three cases outlined in Tables 2 and 3 for the source and detector geometry in a 100-mm-diameter simulated tissue phantom (Fig. 1). Values of θ_m and M_m were computed at each detector in response to four sources of excitation light located at the periphery modulated at a single frequency of 150 MHz. Consequently, the forward solution predicted 80 values of θ_m and M_m, each at detector i ($i = 1, 20$) in response to source k ($k = 1, 4$). Gaussian noise with a standard deviation of 0.1° (or a liberal 1°) in θ_m and 1% in M_m was superimposed on the solution of the forward problem. These obtained data sets are used as the simulated experiments as input to the reconstruction algorithm described below.

4. Inverse Problem and the Solution Methodology

We begin our inverse calculations from a uniform starting guess of a fluorescence yield, $(\eta\mu_{a_{x\to m}})_j$, and lifetime, $(\tau)_j$, at all the grid points within the tissue phantom. With the initial guess of an optical property map, one can evaluate the complex fluence at the various detector locations. There are two approaches that one can follow: one involves minimizing the difference between the complex number that is calculated from the ac magnitude and phase, and the other uses the ac magnitude and phase information itself. The two approaches are equivalent, and we have chosen the second approach of using the ac magnitude and phase. With the starting guess of optical properties, we compute a prediction of phase shift $(\theta_m)_i$ and log of ac amplitude $(M_m)_i$ at each detector i. Values of $(\eta\mu_{a_{x\to m}})_j$ and $(\tau)_j$ are iteratively adjusted at each grid point to minimize the error between the predicted and simulated experimental values of $(\theta_m)_i$ and $(M_m)_i$ resulting from each source, k, $k = 1, 4$. The choice of appropriate functions to be minimized for our reconstructions is now discussed. Section 3 describes at length how changes in the fluorescent yield and lifetime affect the measured values of ac magnitude and phase. Changes in fluorescent yield, $\eta\mu_{a_{x\to m}}$, have a direct and strong influence on the ac magnitude and only an indirect and weak influence on the phase. Hence we have chosen to adjust iteratively the values of $(\eta\mu_{a_{x\to m}})_j$ in order to minimize the merit function, $\chi_\mu{}^2$, that depends on the ac magnitude measurements:

$$\chi_\mu{}^2 = \frac{1}{4}\sum_{k=1}^{4}\frac{1}{20}\sum_{i=1}^{20}\left(\frac{M_{m_{\mathrm{obs},i}} - M_{m,i}}{\sigma_M}\right)^2, \tag{5}$$

where σ_M is the typical standard deviation of noise in M_m, taken to be 0.01.

The value of $M_{m_{\mathrm{obs},i}}$ is the simulated experimental value computed in Section 3 with added Gaussian noise. The goal of the algorithm is to minimize $\chi_\mu{}^2$ by appropriate updates of $(\eta\mu_{a_{x\to m}})_j$. After an iteration of the $(\eta\mu_{a_{x\to m}})_j$ update, values of $(\tau)_j$ were adjusted in the next iteration in order to minimize a second merit function, $\chi_\tau{}^2$:

$$\chi_\tau{}^2 = \frac{1}{4}\sum_{k=1}^{4}\frac{1}{20}\sum_{i=1}^{20}\left[\left(\frac{M_{m_{\mathrm{obs},i}} - M_{m,i}}{\sigma_M}\right)^2 + \left(\frac{\theta_{m_{\mathrm{obs},i}} - \theta_{m,i}}{\sigma_\theta}\right)^2\right], \tag{6}$$

where σ_θ is the typical standard deviation of noise in θ, taken to be 1°. The values of $\theta_{m_{\mathrm{obs},i}}$ are the simulated experimental values computed in Section 3 with added Gaussian noise. The above merit

Table 3. Location and Area of the Simulated Heterogeneities: Comparison of Expected and Reconstructed Values

	Object 1		Object 2	
Case	Area (mm^2)	Location (x, y) (mm)	Area (mm^2)	Location (x, y) (mm)
5.A	706.0 (expected) 742 (obtained)	(60, 60) (expected) (61, 59) (obtained)	not applicable	not applicable
5.B	706.0 (expected) 683 (obtained)	(60, 60) (expected) (59, 58) (obtained)	not applicable	not applicable
5.C	314.1 (expected) 381 (obtained)	(32.3, 67.7) (expected) (34, 68) (obtained)	314.1 (expected) 342 (obtained)	(67.7, 32.3) (expected) (65, 35) (obtained)
5.D	706.0 (expected) 693 (obtained)	(60, 60) (expected) (61, 57) (obtained)	not applicable	not applicable

function is chosen because changes in lifetime τ have a direct and strong influence on both the ac magnitude and phase. Hence we have chosen to adjust iteratively the values of $(\tau)_j$ in order to minimize the merit function that consists of both ac magnitude and phase measurements. The goal of this part of the algorithm is to minimize χ_τ^2 by appropriate choice of $(\tau)_j$ as described below. In Eq. (5), the choice of the value of σ_M does not affect the minimization–update process. We have chosen the typical noise values for M and θ, σ_M and σ_θ, respectively, to be factors for converting to dimensionless numbers. In fact σ_M and σ_θ are simply scale factors that assess confidence in measurement. For example, when σ_θ is smaller for a given σ_M, the θ residuals are weighted more heavily in the inversion as compared with the M residuals. Thus, factor σ is necessary to normalize the individual sum of residuals of M and θ so the two can be added in Eq. (6).

To update values of $(\eta\mu_{a_{x\to m}})_j$ and $(\tau)_j$, one needs the Jacobian matrices that describe the sensitivity of the detector response at position i to changes in $(\tau)_j$ and $(\eta\mu_{a_{x\to m}})_j$ at each grid point, j. The elements of the three Jacobian matrices employed, $\bar{\bar{J}}(M, \eta\mu_{a_{x\to m}})$, $\bar{\bar{J}}(M, \tau)$, and $\bar{\bar{J}}(\theta, \tau)$, are given by $j_{i,j} = [\partial M_i/\partial(\eta\mu_{a_{x\to m}})_j]$, $j_{i,j} = (\partial M_i/\partial\tau_j)$, and $j_{i,j} = (\partial\theta_i/\partial\tau_j)$, respectively. One calculates these elements by solving the forward problem four times for each grid point, j to obtain $M_{m,i}$ and $\theta_{m,i}$ calculated with $(\tau)_j$ and $(\tau + \Delta\tau)_j$ and with $(\eta\mu_{a_{x\to m}})_j$ and $(\eta\mu_{a_{x\to m}} + \Delta\eta\mu_{a_{x\to m}})_j$. From the least-squares minimization, one can show that the update in $\eta\mu_{a_{x\to m}}$ and τ can be calculated by using an algorithm (Newton's method) similar to that suggested by Yorkey *et al.*[30] for the reconstruction of images obtained by electrical impedance tomography.

Equations (7) and (8) provide updates

$$\left[\frac{\bar{\bar{J}}(M, \eta\mu_{a_{x\to m}})^T\bar{\bar{J}}(M, \eta\mu_{a_{x\to m}})}{{\sigma_M}^2} + \lambda_1\bar{\bar{I}}\right][\overline{\Delta\eta\mu_{a_{x\to m}}}] = \left[\frac{\bar{\bar{J}}(M, \eta\mu_{a_{x\to m}})^T}{{\sigma_M}^2}(\bar{M}_{m_{\text{obs}}} - \bar{M}_m)\right], \quad (7)$$

$$\left[\frac{\bar{\bar{J}}(M, \tau)^T\bar{\bar{J}}(M, \tau)}{{\sigma_M}^2} + \frac{\bar{\bar{J}}(\theta, \tau)^T\bar{\bar{J}}(\theta, \tau)}{{\sigma_\theta}^2} + \lambda_2\bar{\bar{I}}\right][\overline{\Delta\tau}] = \left[\frac{\bar{\bar{J}}(M, \tau)^T}{{\sigma_M}^2}(\bar{M}_{m_{\text{obs}}} - \bar{M}_m) + \frac{\bar{\bar{J}}(\theta, \tau)^T}{{\sigma_\theta}^2}(\bar{\theta}_{m_{\text{obs}}} - \bar{\theta}_m)\right], \quad (8)$$

$[\overline{\Delta\eta\mu_{a_{x\to m}}}]$, and $[\overline{\Delta\tau}]$ to the yield $[\overline{\eta\mu_{a_{x\to m}}}]$ and lifetime $[\bar{\tau}]$ vectors at each iteration. The update of $[\overline{\eta\mu_{a_{x\to m}}}]$ is based on the ac amplitude data, whereas that of $[\bar{\tau}]$ is based on both the ac amplitude and phase data. This follows from the discussion in the previous section on the forward problem. $\bar{M}_{m_{\text{obs}}}$ and $\bar{M}_m$ are the experimentally simulated and calculated vectors consisting of the log of the ac amplitude at each of the i detectors, respectively. Because of the ill-conditioned nature of the Jacobian matrices, terms $\lambda_1\bar{\bar{I}}$ or $\lambda_2\bar{\bar{I}}$ are added ($\bar{\bar{I}}$ is an identity matrix) to make the matrices more diagonally dominant and the solution of the algebraic equations more robust. Parameters λ_1 or λ_2 are adjusted by means of a Marquardt–Levenberg type of algorithm.[31] Lower triangular–upper triangular decomposition and backsubstitution are employed to solve the simultaneous linear algebraic equations given in Eqs. (7) and (8).[31] At each iteration, the merit functions, the Jacobian matrices, and the updates in the fluorescent yield and lifetime are evaluated and the iterations are continued until the convergence criterion is met. Convergence is achieved when any of the following three quantities, i.e., χ^2, change in χ^2 in successive iterations, and relative change in χ^2 in successive iterations, is lower than a predetermined value of 1.0×10^{-5}.

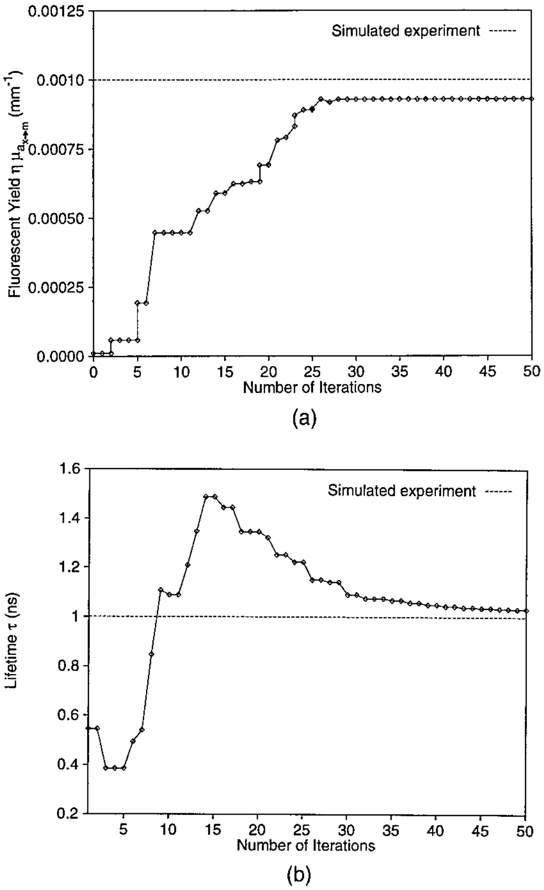

Fig. 6. Graphs depicting the convergence of (a) $\eta\mu_{a_{x\to m}}$, (b) τ versus the number of iterations during the image reconstruction for the case described in Subsection 5.A. Convergence is seen to be achieved within 20 iterations for (a) and 50 iterations for (b).

5. Results and Discussion

The performance of FLI by using the inversion algorithms described above is depicted in Figs. 6–9 for the case studies listed in Tables 2 and 3. Simulated experiment 5.A was designed to reconstruct $(\tau)_j$ and $(\eta\mu_{a_{x\to m}})_j$ with no absorption that is due to nonfluo-

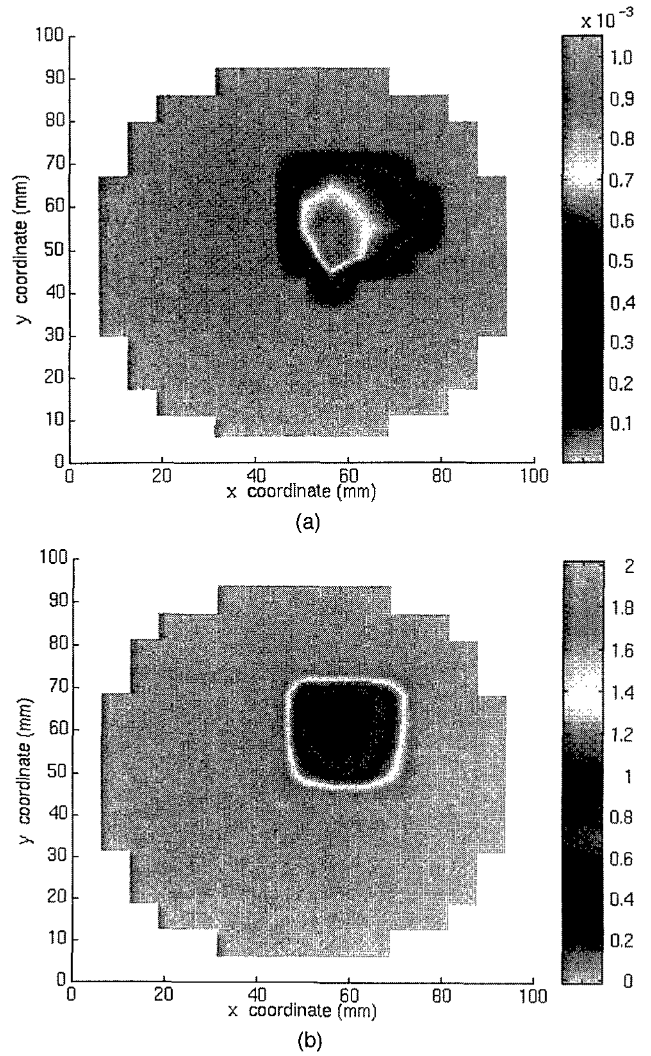

(a)

(b)

Fig. 7. Reconstructed spatial map of fluorescence (a) yield, $\eta\mu_{a_{x\to m}}$, (b) lifetime, τ, on a two-dimensional, 17 × 17 grid for the case described in Subsection 5.A. $\mu_{a_{x\to}}$ at the excitation wavelength not accounting for fluorophore absorption is zero; μ_{a_m} at the emission wavelength is also zero. The average values of $\eta\mu_{a_{x\to m}}$ and τ within the object were 1×10^{-3} mm^{-1} and 1 ns, respectively (expected) and 0.93×10^{-3} mm^{-1} and 1.03, respectively (reconstructed). Spurious unphysically high values of $\eta\mu_{a_{x\to m}}$ and τ have been replaced by the average background fluorescence yield and lifetime, respectively, obtained from the inversion.

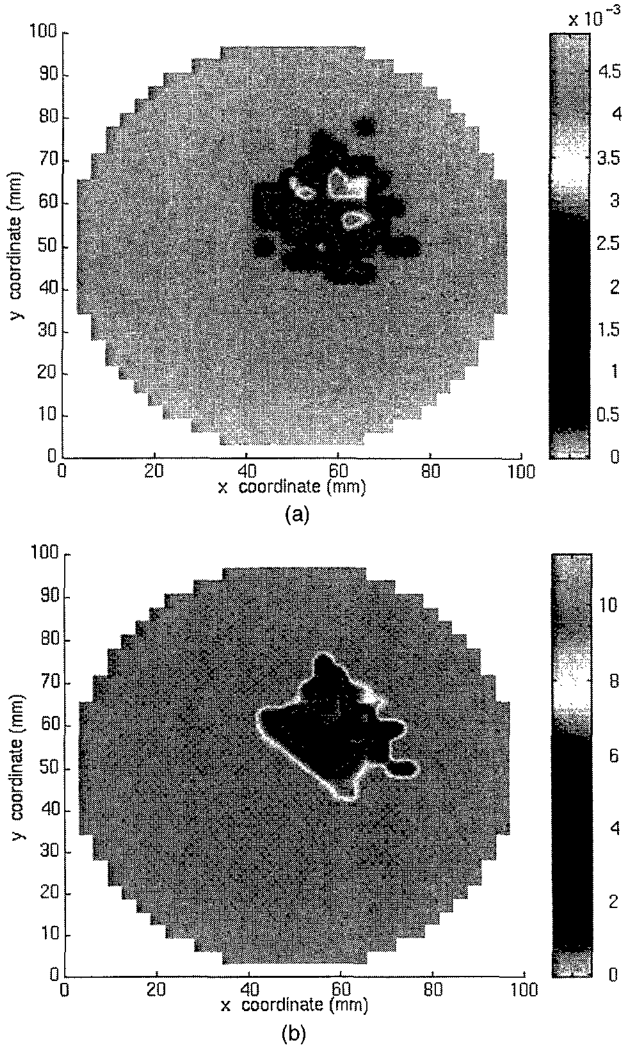

(a)

(b)

Fig. 8. Reconstructed spatial map of fluorescence (a) yield, $\eta\mu_{a_{x\to m}}$, (b) lifetime, τ, on a two-dimensional, 17 × 17 grid for the case described in Subsection 5.B. $\mu_{a_{x\to}}$ at the excitation wavelength not accounting for fluorophore absorption is 1×10^{-3} mm^{-1}; μ_{a_m} at the emission wavelength is zero. The average values of $\eta\mu_{a_{x\to m}}$ and τ within the object were 1×10^{-3} mm^{-1} and 1 ns, respectively (expected) and 0.8×10^{-3} mm^{-1} and 0.7 ns, respectively (reconstructed). Spurious unphysically high values of $\eta\mu_{a_{x\to m}}$ and τ have been replaced by the average background fluorescence yield and lifetime, respectively, obtained from the inversion.

rescing chromophores, whereas simulated experiment 5.B included a finite chromophore absorption of excitation and fluorescent light that could be considered physiological. Finally, simulated experiment 5.C evaluated the ability to determine the location of two hidden objects within the tissue phantom, whereas 5.D examined the reconstruction when the uptake ratio (ratio of fluorescent yield in heterogeneity to that in the background) was 20.

A. Single Heterogeneity with Optical Contrast from $(\tau)_j$ and $(\eta\mu_{a_{x\to m}})_j$ with Absorption of Excitation and Fluorescent Light by Chromophores

To calculate the experimental data for the first case, the fluorescence yields, $\eta\mu_{a_{x\to m}}$, for the background and a single object were chosen as 1×10^{-5} mm^{-1} and 1×10^{-3} mm^{-1}, respectively, and the lifetimes, τ, for the background and the object were chosen as 10 and 1 ns, respectively. During the inverse image reconstruction, no *a priori* knowledge of either the object location or the background fluorescence properties was assumed and a uniform guess of 1×10^{-5} mm^{-1} and 10 ns was given for $\eta\mu_{a_{x\to m}}$ and τ, respectively. Convergence was achieved in fewer than 50 iterations (computational time on a SunSparc 10 was 2 h) for a two-dimensional 17 × 17 grid. The average values of $\eta\mu_{a_{x\to m}}$ and τ in the grid points that occupy the simulated object converge within 50 iterations to the values of $\eta\mu_{a_{x\to m}} = 0.93 \times 10^{-3}$ mm^{-1} and $\tau = 1.03$ ns, which are close to the

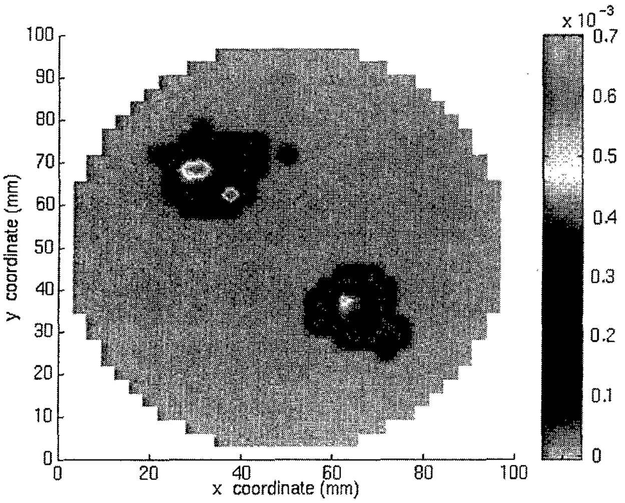

Fig. 9. Reconstructed spatial map of fluorescence yield, $\eta\mu_{a_{x\to m}}$, on a two-dimensional, 33 × 33 grid for the case described in Subsection 5.C. $\mu_{a_{x\to}}$ at the excitation wavelength not accounting for fluorophore absorption is zero; μ_{a_m} at the emission wavelength is also zero. The Gaussian noise that was introduced in the phase had a standard deviation of 1°. The object locations and sizes are recovered correctly. The average values of $\eta\mu_{a_{x\to m}}$ within the two objects were top left, 1×10^{-3} mm^{-1} (expected) and 2×10^{-3} mm^{-1} (reconstructed); bottom right, 2×10^{-3} mm^{-1} (expected) and 1.8×10^{-3} mm^{-1} (reconstructed). Spurious unphysically high values of $\eta\mu_{a_{x\to m}}$ have been replaced by the average background fluorescence yield obtained from the inversion.

correct values of $\eta\mu_{a_{x\to m}} = 1 \times 10^{-3}$ mm^{-1} and $\tau =$ 1 ns, as shown in Figs. 6(a) and 6(b) and listed in Table 4. Figures 7(a) and 7(b) illustrate the reconstructed images of $\eta\mu_{a_{x\to m}}$ and τ, respectively, and are representative of the expected images. The images were smoothed by interpolation in this and subsequent cases. During the reconstruction, it was observed that some grid points, often on or close to the periphery, had unphysically high values of the yield as well as lifetime. Typically, these grid points were loners and were surrounded by grid points with reasonable yield and lifetime values. The high values of lifetime lead to a lower magnitude of fluorescence generation and offset the effect of high yield values. We believe that additional criteria, such as smoothness of the reconstructed maps, may alleviate the spurious background peak values. In this study, these spurious values were replaced by the average background fluorescence yield and lifetime obtained from the inversion. In the subsequent reconstructions, spurious values were similarly handled.

Table 4. Fluorescence Lifetime τ and Yield $\eta\mu_{a_{x\to m}}$ of the Simulated Heterogeneities: Comparison of Expected and Reconstructed Values

Case	$\eta\mu_{a_{x\to m}}$ (Object) (mm^{-1})	τ (Object) (ns)
5.A	1.0×10^{-3} (expected)	1.0 (expected)
	0.93×10^{-3} (obtained)	1.03 (obtained)
5.B	1.0×10^{-3} (expected)	1.0 (expected)
	2.1×10^{-3} (obtained)	4.1 (obtained)
5.C		
Top left object	1.0×10^{-3} (expected)	1.0 (expected)
	2×10^{-3} (obtained)	4.1 (obtained)
Bottom right object	2.0×10^{-3} (expected)	2.0 (expected)
	1.8×10^{-3} (obtained)	3.5 (obtained)
5.D	2.0×10^{-4} (expected)	1.0 (expected)
	7.0×10^{-4} (obtained)	4 (obtained)

The average values of $\eta\mu_{a_{x\to m}}$ in the grid points that occupy the simulated background converge within 50 iterations to 9×10^{-5} mm^{-1} in comparison with the correct value of 1×10^{-5} mm^{-1} (data not shown for brevity). The value of background τ converges to 5.4 ns, which is also far from the correct value of 10 ns. Both discrepancies are attributed to the fact that most of the signal contribution is due to the object, with the object-to-background uptake ratio being 100:1. The dependence of the final images on the choice of the initial guess was examined by providing an initial uniform guess of 1×10^{-4} mm^{-1} and 10 ns for $\eta\mu_{a_{x\to m}}$ and τ, respectively. This resulted in images similar to those obtained with the first guess.

The location of the heterogeneity was identified as consisting of all the grid points with $\eta\mu_{a_{x\to m}}$ higher than 35% (arbitrarily chosen) of the peak value of $\eta\mu_{a_{x\to m}}$ [Fig. 7(a)]. The average of the coordinates of all the identified object grid points was the position (60.8, 58.5), which is close to position (60, 60) that was used to simulate the experimental data. As listed in Table 3, the area of the heterogeneity based on our arbitrary definition for identification was 742 mm^2, close to that used to generate our simulated experimental data. In addition, upon inspection of Fig. 7(a), one can note that values of $\eta\mu_{a_{x\to m}}$ for the object on grid points closer to the center of the phantom were higher than those toward the periphery. This is due to a reduction of signal contributions of grid points located farthest away from source and detectors. This is reflected in a smaller value in the Jacobian matrices and results in a poorer reconstruction at the center of the phantom.

B. Single Heterogeneity with Optical Contrast from $(\tau)_j$ and $(\eta\mu_{a_{x\to m}})_j$ with Absorption of Excitation and Fluorescent Light by Chromophores

The same hidden object location as well as optical parameters were used as described in Subsection 5.A, except that a uniform background chromophore absorption coefficient of the excitation light, $\mu_{a_{x\to}}$ of 1×10^{-3} mm^{-1}, and of the fluorescent light, μ_{a_m} of 1×10^{-3} mm^{-1}, was used to generate the simulated experimental data. Although excitation light propagation was not employed for image reconstruction, we considered this optical property known to estimate the best possible performance for inverse image reconstruction under physiological conditions. The two-dimensional reconstructed spatial map of the fluorescence yield, $\eta\mu_{a_{x\to m}}$, and lifetime, τ, are shown in Figs. 8(a) and 8(b), respectively. The image quality is slightly inferior with respect to both the size as well as the shape of the hidden object. As shown in Table 3, the mean value of location of the object according to our criterion based on $\eta\mu_{a_{x\to m}}$ occurred at position (59, 58), consistent with the conditions used to simulate the experimental data. The dimension of the heterogeneity based on our arbitrary definition for identification (all grid points with $\eta\mu_{a_{x\to m}}$ higher than 35% of the maximum) was 683 mm^2, which is close to that used to generate our simulated experimental data. The average values of $\eta\mu_{a_{x\to m}}$ and τ in the grid points that occupy the simulated object converge within 50 iterations to the values of $\eta\mu_{a_{x\to m}} = 2.1 \times 10^{-3}\ \text{mm}^{-1}$ and $\tau = 4$ ns, which are slightly higher than the values used to generate the simulated experimental data (see Table 4). The average values of $\eta\mu_{a_{x\to m}}$ and τ in the grid points that occupy the simulated background converge within 50 iterations to values similar to those reported in Case 5.A.

C. Two Heterogeneities with Optical Contrast from $(\tau)_j$ and $(\eta\mu_{a_{x\to m}})_j$ with No Absorption of Excitation and Fluorescent Light by Chromophores

In Case 5.C, the same optical parameters were used in forward calculations as described in Subsection 5.A, except that the fluorescence yields, $\eta\mu_{a_{x\to m}}$, for objects 1 and 2 were chosen as $1 \times 10^{-3}\ \text{mm}^{-1}$ and $2 \times 10^{-3}\ \text{mm}^{-1}$, respectively, and lifetimes, τ, for the objects were chosen as 1 ns and 2 ns, respectively. Two 20-mm-diameter circular objects were placed along a diagonal at the coordinates shown in Table 3 within a 100-mm-diameter circular tissue phantom.

Again during the reconstruction, no *a priori* knowledge of either the object location or the background fluorescence properties was assumed and the values of yield $\eta\mu_{a_{x\to m}}$ and lifetime τ were found at all the grid points on a 33 × 33 grid. The two-dimensional reconstructed spatial map of the fluorescence yield, $\eta\mu_{a_{x\to m}}$, is shown in Fig. 9. The object locations (x, y) obtained are given in Table 3 and match well with the conditions used to generate the simulated experimental data. The areas of the objects from the reconstructed image (all grid points with $\eta\mu_{a_{x\to m}}$ higher than 35% of the maximum) were 381 mm^2 (top left, object 1) and 342 mm^2 (bottom right, object 2), slightly larger than inputs to the forward problem. The average values of $\eta\mu_{a_{x\to m}}$ and τ in the grid points that occupy the simulated object converge within 100 iterations to the values of $\eta\mu_{a_{x\to m}} = 2 \times 10^{-3}\ \text{mm}^{-1}$ and $\eta\mu_{a_{x\to m}} = 1.8 \times 10^{-3}\ \text{mm}^{-1}$ for objects 1 and 2, respectively, which again is close to the expected values of $1 \times 10^{-3}\ \text{mm}^{-1}$ and $2 \times 10^{-3}\ \text{mm}^{-1}$. Lifetimes of the two objects were found to be 4.1 and 3.5 ns, respectively, whereas the expected values were 1 and 2 ns, respectively. The quantitative values of $\eta\mu_{a_{x\to m}}$ and τ obtained from the inverse solution are currently unsatisfactory, and research is in progress to improve the solution procedure. The background value of $\eta\mu_{a_{x\to m}}$ agrees well with the expected value of $1.0 \times 10^{-5}\ \text{mm}^{-1}$, whereas the value of the background lifetime was poorly reconstructed.

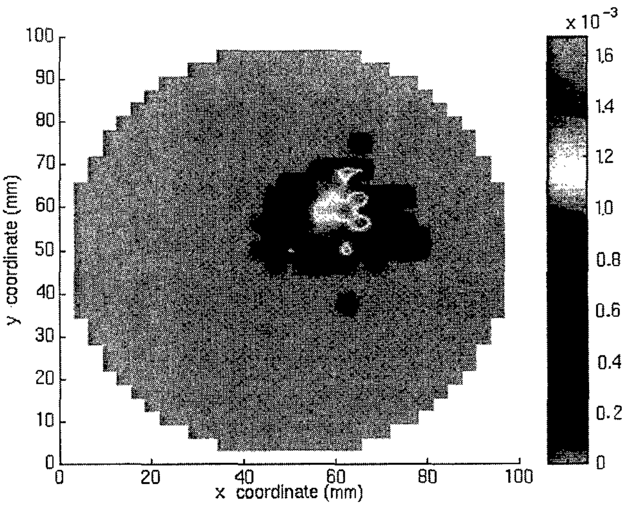

Fig. 10. Reconstructed spatial map of fluorescence yield, $\eta\mu_{a_{x\to m}}$, on a two-dimensional, 33 × 33 grid for the case described in Subsection 5.D. $\mu_{a_{x\to}}$ at the excitation wavelength not accounting for fluorophore absorption is $1 \times 10^{-3}\ \text{mm}^{-1}$; μ_{a_m} at the emission wavelength is the same. The average value of $\eta\mu_{a_{x\to m}}$ within the object was $2 \times 10^{-4}\ \text{mm}^{-1}$ (expected) and $7.0 \times 10^{-4}\ \text{mm}^{-1}$ (reconstructed). Spurious unphysically high values of $\eta\mu_{a_{x\to m}}$ have been replaced by the average background fluorescence yield obtained from the inversion.

D. Single Heterogeneity with Optical Contrast from $(\tau)_j$ and $(\eta\mu_{a_{x\to m}})_j$ with Absorption of Excitation and Fluorescent Light by Chromophores and an Uptake Ratio of 20

The same hidden object location as well as optical parameters were used as described in Subsection 5.A, except that a uniform background chromophore absorption coefficient, $\mu_{a_{x\to}}$, of $1 \times 10^{-3}\ \text{mm}^{-1}$ as well as μ_{a_m} at the emission wavelength of $1 \times 10^{-3}\ \text{mm}^{-1}$ were used to generate the simulated experimental data, and Gaussian noise was added as discussed above. Also, the values of $\eta\mu_{a_{x\to m}}$ for the background and the object were chosen as $1 \times 10^{-5}\ \text{mm}^{-1}$ and $2 \times 10^{-4}\ \text{mm}^{-1}$, thus giving an uptake ratio of 20. Again, although excitation light propagation was not employed for image reconstruction, we considered this optical property to be known in order to estimate the best possible performance for inverse image reconstruction under physiological conditions. The two-dimensional reconstructed spatial map of the fluorescence yield, $\eta\mu_{a_{x\to m}}$, is shown in Fig. 10. The image quality with respect to both the size as well as the shape of the hidden object is good. As shown in Table 3, the mean value of location of the object according to our criterion based on $\eta\mu_{a_{x\to m}}$ occurred at position (61, 57), consistent with the conditions used to simulate the experimental data. The dimension of the heterogeneity based on our arbitrary definition for identification (all grid points with $\eta\mu_{a_{x\to m}}$ higher than 35% of the maximum) was 693 mm^2, which is close to that used to generate our simulated experimental data. The average values of

$\eta\mu_{a_{x\to m}}$ and τ in the grid points that occupy the simulated object converge within 50 iterations to the values of $\eta\mu_{a_{x\to m}} = 7 \times 10^{-4}$ mm^{-1} and $\tau = 4$ ns, which are slightly higher than the values used to generate the simulated experimental data (see Table 4). The average values of $\eta\mu_{a_{x\to m}}$ and τ in the grid points that occupy the simulated background converge within 50 iterations to values similar to those reported in Case 5.A. Nonetheless, it is shown that image reconstruction may be successful even in the case of uptake ratio as small as 20.

The performance of the inverse imaging algorithm may be improved by including additional information obtained from multifrequency measurements and from excitation wavelength measurements. In addition, the appropriate weighting of grid point contributions based on the signal strength may also improve reconstruction results.

6. Conclusions

The fluorescent yield and lifetime of an endogenous fluorophore may be sensitive to local environments, providing specificity for contrast of diseased over normal tissues and optimal detection of disease by using optical techniques.[32] Our simulated experiments show that it is possible to reconstruct the fluorescent yield and lifetime of embedded fluorophores in tissue-mimicking scattering media from frequency-domain measurements of fluorescent phase shift and ac amplitude or amplitude modulation. As we have shown in Subsection 5.C, the reconstruction of lifetime can be problematic by using the reemitted fluorescent signal at one modulation frequency. This is in agreement with O'Leary *et al.*,[33] who resorted to the need for measurements in the absence of fluorophore (background properties) as well as in its presence for lifetime reconstruction as suggested from multipixel measurements for photon migration imaging.[34] Currently, we are experimentally investigating the implementation of FLI by using both excitation and fluorescent wavelengths as well as multifrequency measurements to improve inverse solutions that predict both fluorescent yield and lifetime.

Appendix A: Nomenclature

c,	velocity of light
$D(r)$,	optical diffusion coefficient
f,	modulation frequency
$\bar{\bar{I}}$,	identity matrix
i,	detector number, $i = 1, 20$
$\bar{\bar{J}}$,	Jacobian matrix relating the sensitivity of optical parameters to the detector response
j,	grid point number
$j_{i,j}$,	individual elements of Jacobian matrix $\bar{\bar{J}}$
k,	source number, $k = 1,4$
M,	log of ac amplitude of modulated fluorescent light
r,	position
$S(r, \omega)$,	source term for the modulated light at position r and frequency ω

Greek

χ^2,	merit function representing the least-squares error
$\Phi(r, \omega)$,	complex number representing the photon flux in the frequency domain at position r and frequency ω
η,	quantum yield of the fluorescent probe or dye
μ_a,	average absorption coefficient of the tissue
μ_{a_m},	absorption coefficient of the fluorescence light by both the nonfluorescing chromophores and fluorophore
μ_{a_x},	absorption coefficient of the excitation light by both the nonfluorescing chromophores and fluorophore
$\mu_{a_{m\to}}$,	absorption coefficient of the fluorescence light by both the nonfluorescing chromophores
$\mu_{a_{x\to}}$,	absorption coefficient of the excitation light by the nonfluorescing chromophores
$\mu_{a_{x\to m}}$,	absorption coefficient of the excitation light by the fluorophore
μ_s',	effective scattering coefficient of the tissue
θ,	phase shift of the modulated light wave with respect to the modulated wave at the source
σ,	standard deviation of the Gaussian noise representing the experimental uncertainty
$\tau(r)$,	lifetime of the activated probe or dye at location r
ω,	angular modulation frequency, given by $2\pi f$

Subscripts

obs,	observed or experimental data
x,	excitation light
m,	fluorescence or emission light

Appendix B: Jacobian Matrices

We provide more details about the elements of the Jacobian matrices introduced in Section 4. Element $j_{i,j}$ of a Jacobian matrix represents the sensitivity of the response of detector i to changes in the optical property at grid point j. Here as an example we show the response of detector 16 for source A (see Fig. 1) to changes in τ and $\eta\mu_{a_{x\to m}}$ at all the grid points for the case described in Subsection 5.A for the first iteration during inversion when $\mu_{a_{x\to}}$ was chosen as zero. Similar results are observed for other cases. Figures 11(a) and 11(b) show the elements of Jacobian matrices $\bar{\bar{J}}(\theta, \tau)$ and $\bar{\bar{J}}(M, \tau)$, respectively, where τ at each of the grid points was increased by 5%. Similarly, Fig. 11(c) shows the elements of Jacobian matrix $\bar{\bar{J}}(M, \eta\mu_{a_{x\to m}})$, where $(\eta\mu_{a_{x\to m}})$ at each of the grid points was increased by 1%. Most of the elements of $\bar{\bar{J}}(\theta, \tau)$ and $\bar{\bar{J}}(M, \eta\mu_{a_{x\to m}})$ are positive, whereas most of the elements of $\bar{\bar{J}}(M, \tau)$ are negative. This is according to our expectation of systems with no scattering. The dependence on scatter has, of course, been taken into account in the above example.

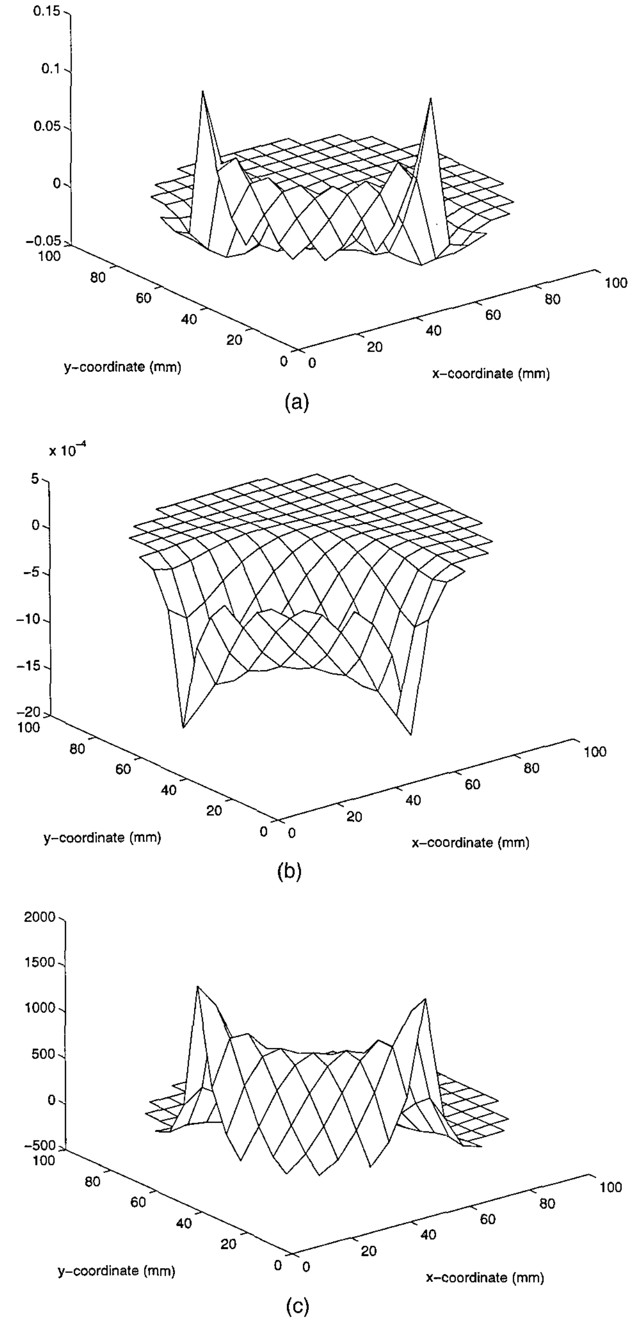

Fig. 11. Jacobian (a) $\bar{\bar{J}}(\theta, \tau)$, (b) $\bar{\bar{J}}(M, \tau)$, (c) $\bar{\bar{J}}(M, \eta\mu_{a_{x\to m}})$ for the case described in Subsection 5.A for source A, detector 16, and iteration 1. During the computation of the Jacobians, the values of τ for (a) and (b) and $\eta\mu_{a_{x\to m}}$ for (c) at each individual grid point were increased by 5%, 5%, and 1%, respectively.

This research was supported in part by National Institutes of Health grants NIH K04CA68374 and NIH R01CA61413 and by the U.S. Department of Defense grant DOD RP951661.

References

1. R. L. Sheridan, K. T. Schomaker, L. C. Lucchina, J. Hurley, L. M. Yin, R. G. Tompkins, M. Jerath, A. Torri, K. Greaves, D. Bua, and N. S. Nishioka, “Burn depth estimation by use of indocyanine green fluorescence: initial human trial,” J. Burn Care Rehabil. **16,** 602–604 (1995).
2. W. Poon, K. T. Schomaker, T. F. Deutsch, and R. L. Martuza, “Laser-induced fluorescence: experimental intraoperative delineation of tumor resection margins,” J. Neurosurg. **76,** 679–686 (1992).
3. S. Andersson-Engels, J. Johansson, U. Stenram, K. Svanberg, and S. Svanberg, “Time-resolved laser-induced fluorescence spectroscopy for enhanced demarcation of human atherosclerotic plaques,” J. Photochem. Photobiol. **4,** 363–369 (1990).
4. S. Andersson-Engels, J. Ankerst, J. Johansson, K. Svanberg, and S. Svanberg, “Laser-induced fluorescence in malignant and normal tissue of rats injected with benzoporphryin derivative,” Photochem. Photobiol. **57,** 978–983 (1993).
5. B. C. Wilson, E. M. Sevick, M. S. Patterson, and B. Chance, “Time-dependent optical spectroscopy and imaging for biomedical applications,” Proc. IEEE **80,** 918–930 (1992).
6. S. Mordon, J. M. Devoisselle, and V. Maunoury, “In vivo pH measurement and imaging of a pH-sensitive fluorescent probe (5-6-carboxyfluorescein): instrumental and experimental studies,” Photochem. Photobiol. **60,** 274–279 (1994).
7. D. A. Russell, R. H. Pottier, and D. P. Valenzeno, “Continuous noninvasive measurement of in vivo pH in conscious mice,” Photochem. Photobiol. **59,** 309–313 (1994).
8. S. A. Vinogradov, L. W. Lo, W. T. Jenkins, S. M. Evans, C. Koch, and D. F. Wilson, “Noninvasive imaging of the distribution in oxygen in tissue in vivo using near-infrared phosphors,” Biophys. J. **70,** 1609–1617 (1996).
9. E. M. Sevick-Muraca, C. L. Hutchinson, and D. Y. Paithankar, “Optical tissue biodiagnostics using fluorescence lifetime,” Opt. Photon. News **7,** 25–28 (1996).
10. B. W. Pogue, M. S. Patterson, H. Jiang, and K. D. Paulsen, “Initial assessment of a simple system for frequency domain diffuse optical tomography,” Phys. Med. Biol. **40,** 1709–1729 (1995).
11. R. L. Barbour, H. L. Graber, Y. Wang, J. Chang, and R. Aronson, “Perturbation approach for optical diffusion tomography using continuous-wave and time-resolved data,” in *Medical Optical Tomography: Functional Imaging and Monitoring,* G. Müller, B. Chance, R. Alfano, S. Arridge, J. Beuthan, E. Gratton, M. Kaschke, B. Masters, S. Svanberg, and P. Vander Zee, eds. (SPIE, Bellingham, Wash., 1993), pp. 87–120.
12. M. A. O’Leary, D. A. Boas, B. Chance, and A. G. Yodh, “Experimental images of heterogeneous turbid media by frequency-domain diffusing photon tomography,” Opt. Lett. **20,** 426–428 (1995).
13. H. Jiang, K. D. Paulsen, U. L. Osterberg, B. W. Pogue, and M. S. Patterson, “Optical image reconstruction using frequency-domain data: simulations and experiments,” J. Opt. Soc. Am. **13,** 253–266 (1996).
14. T. L. Troy, D. L. Page, and E. M. Sevick-Muraca, “Optical properties of normal and diseased breast tissues: prognosis for optical mammography,” J. Biomed. Opt. **1,** 342–355 (1996).
15. G. Lopez, T. L. Troy, C. L. Hutchinson, J. S. Reynolds, and E. M. Sevick-Muraca, “Fluorescent contrast agents for biomedical optical imaging using frequency-domain techniques,” J. R. Lakowicz and R. B. Thompson, eds., Proc. SPIE **2980** (1997).
16. J. Wu, Y. Wang, L. Perelman, I. Itzkan, R. Dasari, and M. Feld, “Three-dimensional imaging of objects embedded in turbid media with fluorescence and Raman spectroscopy,” Appl. Opt. **34,** 3425–3430 (1995).
17. K. M. Yoo, Z.-H. Zang, S. A. Ahmed, and R. R. Alfano, “Imaging objects hidden in scattering media using a fluorescence-absorption technique,” Opt. Lett. **16,** 1252–1254 (1991).
18. A. Knuttel, J. M. Schmitt, R. Barnes, and J. R. Knutson, “Acousto-optic scanning and interfering photon density waves for precise localization of an absorbing (or fluorescent) body in a turbid medium,” Rev. Sci. Instrum. **64,** 638–644 (1993).
19. M. A. O’Leary, D. A. Boas, B. Chance, and A. G. Yodh, “Re-

radiation and imaging of diffuse photon density waves using fluorescent inhomogeneities," J. Lumin. **60&61,** 281–286 (1994).

20. R. Cubbedu, G. Canti, P. Taroni, and G. Valentini, "Time-gated fluorescence imaging for the diagnosis of tumors in a murine model," Photochem. Photobiol. **57,** 480–485 (1993).
21. E. M. Sevick-Muraca and C. L. Burch, "The origin of phosphorescent and fluorescent signals in tissues," Opt. Lett. **19,** 1928–1930 (1994).
22. M. S. Patterson and B. W. Pogue, "A mathematical model for time-resolved and frequency-domain fluorescence spectroscopy in tissues," Appl. Opt. **33,** 1963–1974 (1994).
23. C. L. Hutchinson, J. R. Lakowicz, and E. M. Sevick-Muraca, "Fluorescence lifetime based sensing in tissues: a computational study," Biophys. J. **68,** 1574–1582 (1995).
24. C. L. Hutchinson, T. L. Troy, and E. M. Sevick-Muraca, "Fluorescence-lifetime determination in tissues or other scattering media from measurement of excitation and emission kinetics," Appl. Opt. **35,** 2325–2332 (1996).
25. S. R. Fulton, C. E. Ciesielski, and W. H. Schubert, "Multigrid methods for elliptic problems: a review," Mon. Weather Rev. **114,** 943 (1986).
26. J. C. Adams, "MUDPACK: multigrid portable Fortran software for the efficient solution of linear elliptic partial differential equations," Appl. Math. Comp. **34,** 133 (1989).
27. R. A. Day, Jr. and A. L. Underwood, *Quantitative Analysis*, 6th ed. (Prentice-Hall, Englewood Cliffs, N.J., 1991), p. 446.
28. E. M. Sevick, J. K. Frisoli, C. L. Burch, and J. R. Lakowicz, "Localization of absorbers using frequency-domain measurements of time-dependent photon migration," Appl. Opt. **33,** 3562–3570 (1994).
29. X. D. Li, M. A. O'Leary, D. A. Boas, B. Chance, and A. G. Yodh, "Fluorescent diffuse photon density waves in homogeneous and heterogeneous turbid media: analytic solutions and applications," Appl. Opt. **35,** 3746–3758 (1996).
30. T. J. Yorkey, J. G. Webster, and W. J. Tompkins, "Comparing reconstruction algorithms for electrical impedance tomography," IEEE Trans. Biomed. Eng. **BME-34,** 843–852 (1987).
31. W. H. Press, S. A. Teukolsy, W. T. Vetterling, and B. P. Flannery, *Numerical Recipes: The Art of Scientific Computing* (Cambridge U. Press, New York, 1992).
32. E. M. Sevick-Muraca, D. Y. Paithankar, C. L. Hutchinson, and T. L. Troy, "Analysis of photon migration for optical diagnosis," in *Ultrasensitive Biochemical Diagnostics*, G. E. Cohn, S. A. Soper, and C. Chen, eds., Proc. SPIE **2680,** 114–123 (1996).
33. M. A. O'Leary, D. A. Boas, D. X. Li, B. Chance, and A. G. Yodh, "Fluorescence lifetime imaging in turbid media," Opt. Lett. **21,** 158–160 (1996).
34. E. M. Sevick, J. R. Lakowicz, H. Szamacinski, K. Nowaczyk, and M. L. Johnson, "Frequency domain imaging of absorbers obscured by scattering," J. Photochem. Photobiol. B **16,** 169–185 (1992).

The Role of Higher Order Scattering in Solutions to the Forward and Inverse Optical Imaging Problems in Random Media

E.M. Sevick-Muraca*, D. L. Heintzelman, J. Lee, T. L. Troy,
and D. Y. Paithankar.

School of Chemical Engineering
Purdue University
West Lafayette, IN 47907
sevick@ecn.purdue.edu

Keywords: photon migration imaging, image reconstruction, frequency-domain, inverse problem, biomedical optical imaging

submitted to *Applied Optics*
8/15/96
revised manuscript to *Applied Optics*
5/22/97

Abstract

From analytical and numerical solutions predicting the scattering of diffuse photon density waves and from experimental measurements of changes in phase-shift, θ, and AC amplitude demodulation, M, due to the presence of single and double cylindrical heterogeneities, we show that second and higher order perturbations can impact the prediction of the propagation characteristics of diffuse photon density waves. Our experimental results for perfect absorbers in a lossless medium suggest that the performance of fast inverse imaging algorithms which employ first order Born or Rytov approximations may have inherent limitations as compared to inverse solutions that employ iterative solutions of a linear perturbation equation or numerical solutions of the diffusion equation.

**To whom correspondence should be addressed*

1.0 Introduction

With the development of near-infrared red (NIR) emitting laser diodes and the realization that NIR light can travel several centimeters through tissue, numerous groups have embarked upon the development of optical imaging as a new medical imaging modality. While approaches vary from monitoring the vanishingly small component of coherent light using sophisticated techniques of Kerr-filtering,[1] time-gating,[2] and conservation of light polarization,[3] other approaches focus on monitoring the predominant optical signal re-emitted from tissues: the multiply scattered signal. Continuous wave (CW),[4] time-domain,[5] and frequency-domain[6-8] measurements of multiply scattered light have been performed in simulated and experimental tissue phantom studies as well as in human studies.[9] However, the use of these measurements to reconstruct maps of internal tissue optical properties for diagnostic imaging has been problematic, since the geometric correlation between incident and detected radiation is destroyed by multiple scattering.

While some investigators have used direct image reconstruction approaches employing measured optical data to directly form an image,[9-11] others have sought full solution to the inverse imaging problem, which relates external time-dependent measurements made at the periphery to an optical property map of interior volumes via the optical diffusion equation[6-8, 12-16]. Two approaches to solve the inverse solution have been adopted. In the first approach, the fluence associated with a propagating photon density wave launched at source position, ρ_s and detected at the tissue periphery at position

ρ_d (denoted $\Phi(\rho_s, \rho_d)$), is related to the fluence assumed in the absence of any optical heterogeneities (denoted $\Phi_{inc}(\rho_s, \rho_d)$) and the internal optical property perturbation map, $\Delta(\rho)$, through an Fredholm integral equation of the first kind:

$$\Phi(\rho_s,\rho_d) = \Phi_{inc}(\rho_s,\rho_d) + \int G(\rho,\rho_d)\Phi_o(\rho_s,\rho_d)\Delta(\rho)\partial^3\rho \qquad (1)$$

where $G(\rho,\rho_d)$ is the Green's function to the diffusion equation $\left(= \exp\left[\frac{\sqrt{(-\mu_a + i\omega / c_n)/D}}{4\pi D(\rho - \rho_d)}(\rho - \rho_d)\right]\right.$ describing the propagation of light from position ρ to the detector at ρ_d and Φ_o is the incident wave impinging at position ρ. If one assumes that the incident wave impinging upon the position ρ can be approximated by the fluence predicted in the absence of heterogeneities (i.e., $\Phi_o \rightarrow \Phi_{inc}$, known as the Born approximation), then upon measurement of fluence at a variety of source-detector separations and upon discretization of Eqn (1), an optical map of perturbations, $\Delta(\rho)$, can be obtained to a first order approximation.[15] However, the Born approximation $\Phi_o \rightarrow \Phi_{inc}$ does not account for second and higher order effects which may arise from the re-scattering of photon density waves associated with neighboring inhomogeneities. In addition, this approach assumes that perturbations in optical properties at a position ρ_j does not influence the propagation of light from position ρ_{j+1} to detector ρ_d as described by the Green's function, $G(\rho,\rho_d)$.

The Born iterative method (BIM) tends to account for strong perturbations and for second and higher order scattering effects by using the first order approximation of optical property perturbations, $\Delta(\rho)$, to recalculate Φ_0 or the fluence incident at position ρ. Yao and coworkers have shown that the Born iterative method tends to compensate for the underprediction of the scattering and absorption properties of a single heterogeneity in an otherwise uniform medium that would occur when the Born approximation (or single iteration) is used. In addition to the Born iterative methods, the Distorted Born iterative (DIBM) method represents a refinement in that it also recompiles the Green's functions, $G(\rho,\rho_d)$ to reflect changes in light propagation and should speed convergence. Yet to date, there has been no investigation to address how these iterative reconstruction algorithms impact the resolution, or more concisely how these linear perturbation approaches can be used to accurately image closely positioned, multiple heterogeneities between which non-linear, second and higher order scattering effects exist.

In contrast to this inversion approach, Jiang, *et al.*[7,8] and Arridge, *et al.,*[14] have utilized full numerical solution to the diffusion equation which describes the interdependence of voxel optical properties and their contribution to the re-emitted optical signal detected from CW and frequency-domain measurements. Using this approach, the second and higher order scattering arising from multiple inhomogeneities which are not accounted for in the first iterations of Born and Rytov approximations, are incorporated in the forward and inverse solutions. The inversion consists of relating spatial changes of optical properties on detected frequency-domain measurements through numerical solution of the diffusion equation and then solving an update to the map of optical properties from the difference between the signals that are measured and those that are predicted by the forward solution to the diffusion equation. It is important to note that convergence upon the optical properties is achieved with these numerical approaches and *not* with the iterative Born and Rytov approaches. Nonetheless, while the computational investment of iterative, but analytical-based inversions is less than that involving full numerical solution of the diffusion equation, the relative performance of these two inverse solution approaches has yet to be evaluated.

For this reason, we embarked on a study to assess the contributions of neighboring heterogeneities using experimental, numerical, and analytical computations of scattered photon density waves from perfect light absorbing cylinders. Specifically, we experimentally and computationally monitor the multiple scattering of photon density waves between two neighboring perfect cylindrical absorbers embedded in a tissue-mimicking scattering medium in order to assess the higher order perturbation effects upon a re-emitted, detected photon density wave. In the following, we briefly review the theory of higher order perturbation effects as predicted from the experimental frequency-domain measurements as well as from the Helmholtz equations. In addition, we present experimental measurements and numerical solutions of the optical diffusion equation which show the errors introduced by neglecting second order effects which can be significant. These errors can define the limits of resolution for two perfect absorbers in the inverse solution approaches which do not employ BIM, DBIM, or the full numerical solution of the optical diffusion equation. We comment upon these effects when contrast is owing to mechanisms other than a perfect absorber.

2.0 Theoretical background for perturbations associated with diffuse photon density waves

Our work to assess the contributions of higher order perturbations has been motivated by the work of Boas, *et al.*[15] Their approach for image reconstruction from diffusely propagating photon density waves employs analytical expressions to describe the complex fluence of a propagating photon density wave, $\Phi(\rho)$, in the presence of m heterogeneities by superposition of incident, $\Phi_{inc}(\rho)$, and scattered waves, $\Phi^{n}_{scat,k}(\rho)$, from body k and of order n:

$$\Phi(\rho) = \Phi_{inc}(\rho) + \sum_{n=1}^{\infty} \sum_{k=1}^{m} \Phi^{n}_{scat,k}(\rho) \qquad (2)$$

Figure 1 is reproduced from the work of Boas and coworkers to pictorially describe the second order effects due to the scattering of a photon density wave between two objects and to delineate their contribution to the detected photon density wave, $\Phi(\rho)$. Second and higher order scattering effects arise from the re-scattering of an incident wave between the two bodies. These authors assume that second order scattering effects (denoted by the dotted line in Figure 1) are negligible under most circumstances. In our work, we explore this assumption using experimental, numerical, and analytical predictions of second order contributions.

2.1 Analysis of experimental measurements of photon density waves

In order to measure second order contributions, we experimentally measured the detected photon density wave in the presence of one light absorbing object alone, Φ_{k1}; object two alone, Φ_{k2}; and with both objects present, $\Phi_{k1,k2}$ as a function of object positions, ρ_1, and ρ_2, and separation between the two objects, ρ_1-ρ_2 (See Figure 2). From Eqn (2), expressions can be written for measurements of Φ_{k1} and Φ_{k2} made at detector position, ρ_d, in the presence of single objects:

$$\Phi_{k1}(\rho_d) = \Phi_{inc}(\rho_d) + \Phi^{n=1}_{scat,k1}(\rho_d) \tag{3}$$

$$\Phi_{k2}(\rho_d) = \Phi_{inc}(\rho_d) + \Phi^{n=1}_{scat,k2}(\rho_d) \tag{4}$$

where *k1* denotes the presence of the first body alone and *k2* denotes the presence of the second body. With simple algebraic manipulation of Eqns. (2) through (4), an expression accounting for higher order scattering effects can be written for the photon density wave in the presence of both objects, $\Phi_{k1,k2}(\rho_d)$:

$$\begin{aligned}\Phi_{k1,k2}(\rho_d) = \Phi_{k1}(\rho_d) + \Phi_{k2}(\rho_d) - \Phi_{inc}(\rho_d) + \\ \Phi^{n=2}_{scat,k1,k2}(\rho_d) + \Phi^{n=3}_{scat,k1,k2}(\rho_d) + \ldots\end{aligned} \tag{5}$$

For the purposes of this study, it is assumed that third and higher order scattered waves are considered to have insignificant contributions to the measured fluence when compared to first and second order scattered waves.

From frequency-domain measurements of phase-shift, θ, and AC amplitude, M, values of the complex fluence, $\Phi = Me^{i\theta}$ can be obtained (i) in the presence of the first object alone $\Phi_{k1}(\rho_d)$, (ii) in presence of the second object alone $\Phi_{k2}(\rho_d)$, (iii) in the presence of both objects, $\Phi_{k1,k2}(\rho_d)$; and in the absence of any inhomogeneities, $\Phi_{inc}(\rho_d)$. If second order effects, i.e.,

$\Phi^{n=2}_{scat,k1,k2}(\rho_d)$, are negligible, then from Eqn (5) it follows that measurements of $\Phi_{k1,k2}(\rho_d)$ should be predicted by measurements of $\Phi_{k1}(\rho_d)$, $\Phi_{k2}(\rho_d)$, and $\Phi_{inc}(\rho_d)$:

$$\Phi_{k1,k2}(\rho_d) = \Phi_{k=1}(\rho_d) + \Phi_{k=2}(\rho_d) - \Phi_{inc}(\rho_d) \qquad (6)$$

Since we report our results in terms of phase-shift and amplitude demodulation, Eqn (6) can be written as:

$$\theta_{k1,k2}(\rho_d) = \tan^{-1}\left[\frac{M_{k1}\sin\theta_{k1} + M_{k2}\sin\theta_{k2} - M_{inc}\sin\theta_{inc}}{M_{k1}\cos\theta_{k1} + M_{k2}\cos\theta_{k2} - M_{inc}\cos\theta_{inc}}\right] \qquad (7)$$

$$M_{k1,k2}(\rho_d) = \sqrt{\begin{array}{c}[M_{k1}\cos\theta_{k1} + M_{k2}\cos\theta_{k2} - M_{inc}\cos\theta_{inc}]^2 + \\ [M_{k1}\sin\theta_{k1} + M_{k2}\sin\theta_{k2} - M_{inc}\sin\theta_{inc}]^2\end{array}} \qquad (8)$$

2.2 Analysis of analytical predictions of phase-shift and amplitude modulation owing to two perfect absorbing cylinders

The complex fluence describing the propagation of a photon density wave can also be computed analytically from the Helmholtz equations.[15,16] The complex fluence propagating from a source point at ρ_s, through an infinite random medium, and received at position, ρ, in the absence of an optical heterogeneity is given by:

$$\Phi_{inc}(\rho) = S_{source}(\rho_s)\frac{\exp\{i\sqrt{\frac{-\mu_a + i\omega / c_n}{D}}\left[\rho - \rho_d\right]\}}{4\pi D\left[\rho - \rho_d\right]} \tag{9}$$

where S_{source} describes the phase and strength of modulation of the source located at position ρ_s; c_n is the speed of light in the medium; and D is the "optical diffusion coefficient" which is governed by the absorption, μ_a, and isotropic scattering, μ'_s, coefficients of the continuous or homogeneous medium:

$$D = \frac{1}{3[\mu_a + \mu'_s]} \tag{10}$$

In this study, we approximate a point modulated source at the periphery of a large cylinder as a point modulated source located at the interface of a semi-infinite medium. In this case, the fluence is written in cylindrical coordinates and at the surface (z=0) given by:[17]

$$\Phi_{inc}(\rho_d) = S_{source}(\rho_s)\frac{1}{4\pi D}\left\{\begin{array}{c}\dfrac{\exp\left[-\sqrt{\dfrac{\mu_{a+i\omega/c_n}}{D}}\left((\rho_s - \rho_d)^2 + (z - z_o)^2\right)^{\frac{1}{2}}\right]}{\sqrt{((\rho_s - \rho_d)^2 + (z - z_o)^2}} \\ -\dfrac{\exp\left[-\sqrt{\dfrac{\mu_{a+i\omega/c_n}}{D}}\left((\rho_s - \rho_d)^2 + (z + z_o)^2\right)^{\frac{1}{2}}\right]}{\sqrt{((\rho_s - \rho_d)^2 + (z + z_o)^2}}\end{array}\right\} \tag{11}$$

where z_o is one isotropic scattering length ($1/\mu'_s$).

The first order (n=1) scattered wave from the *k1* infinitely long cylinder in an infinite medium is given by:[15,18]

$$\Phi^{n=1}_{scat,k1}(\rho_d) = -\Phi_{inc} \sum_{m=1}^{\infty} \int_{0}^{\infty} \cos(m\vartheta)\cos(pz) K_m\left(\sqrt{p^2 + \left(\frac{-\mu_a + i\omega / c_n}{D}\right)}\rho_d\right)$$
$$\bullet K_m\left(\sqrt{p^2 + \left(\frac{-\mu_a + i\omega / c_n}{D}\right)}\rho_s\right)$$
$$\bullet\left[\frac{D x I'_m(x) I_m(y) - D'_{k1} y I_m(x) I'_m(y)}{D x K'_m(x) I_m(y) - D'_{k1} y K_m(x) I'_m(y)}\right]dp \qquad (12)$$

where D_k' is the optical diffusion coefficient within the cylinder, *k*; I_m and K_m are modified Bessel functions; $x = \sqrt{p^2 + \left[\frac{-\mu_a + i\omega / c_n}{D}\right]}a_k$; $y = \sqrt{p^2 + \left[\frac{-\mu_a' + i\omega / c_n}{D_k'}\right]}a_k$; and a_k is the radius of cylinder *k1*. Radius ρ_d, angle ϑ, and length z denote the coordinates of the detector relative to the center of the infinite cylinder, *k1* (Figure 2). The incident wave upon the infinite cylinder, Φ_{inc}, is computed from Eqn (11). A similar expression can be written for $\Phi^{n=1}_{scat,k2}$.

Second order scattering contributions were calculated by evaluating the scattered wave originating from the second object (*k2*) as the incident wave upon the first object (*k1*). In other words,

$$\Phi^{n=2}_{scat,k1}(\rho_d) = -\Phi^{n=1}_{scat,k2}\sum_{m=1}^{\infty}\int_0^{\infty}\cos(m\vartheta)\cos(pz)K_m\left(\sqrt{p^2+\left(\frac{-\mu_a+i\omega/c_n}{D}\right)}\rho_d\right)$$

$$\bullet K_m\left(\sqrt{p^2+\left(\frac{-\mu_a+i\omega/c_n}{D}\right)}\rho_s\right)$$

$$\bullet\left[\frac{DxI'_m(x)I_m(y)-D'_{k1}yI_m(x)I'_m(y)}{DxK'_m(x)I_m(y)-D'_{k1}yK_m(x)I'_m(y)}\right]dp \tag{13}$$

where the incident wave upon cylinder k1 is now the first order scattered wave $\Phi^{n=1}_{scat,k2}$ that is computed from Eqn (12). A similar expression can be written for $\Phi^{n=2}_{scat,k2}$. Since the optical properties and diameter of the two cylinders were identical in this study, we consider the case where $D'_1 = D'_2$ and a_1=a_2.

Using the approach described above, the fluence detected at position ρ_d can be computed inclusive of first order scattering effects (i.e., $\Phi(\rho_d) = \Phi_{inc}(\rho_d) + \sum_{k=1}^{2}\Phi^{n=1}_{scat,k}(\rho_d)$), as well as second order scattering effects (i.e., $\Phi(\rho_d) = \Phi_{inc}(\rho_d) + \sum_{n=1}^{2}\sum_{k=1}^{2}\Phi^{n}_{scat,k}(\rho_d)$). From final values of complex fluence, the phase-shift and amplitude demodulation can be predicted from the simple relationships:

$$\theta(\rho_d) = \tan^{-1}\frac{\mathrm{Im}[\Phi(\rho_d)]}{\mathrm{Re}[\Phi(\rho_d)]} \tag{14}$$

$$M(\rho_d) = \sqrt{[\mathrm{Im}\{\Phi(\rho_d)\}]^2 + [\mathrm{Re}\{\Phi(\rho_d)\}]^2} \tag{15}$$

3.0 Materials and Methods

3.1 Experimental measurements of phase-shift owing to two cylindrical absorbers

In order to experimentally measure $M_{k1,k2}(\rho_d)$, $M_{k1}(\rho_d)$, $M_{k2}(\rho_d)$, $M_{inc}(\rho_d)$, $\theta_{k1,k2}(\rho_d)$, $\theta_{k1}(\rho_d)$, $\theta_{k2}(\rho_d)$, and $\theta_{inc}(\rho_d)$, frequency domain measurements were made using an apparatus employing picosecond pulsed light at 780 nm with an average power of 1.3 watts. Details of the apparatus are described elsewhere.[19] The phantom consisted of a plexiglass cylinder (with a 16.5 cm diameter and 20 cm height), filled with a 0.5% Intralipid solution (Kabi Pharmacia, Inc., Clayton, NC). As illustrated in Figure 3, light was delivered to a peripheral point on the cylinder using a 1000 micron fiber (HCP-M1000T-08, Spectron Specialty Optics, Co., Avon, Conn) and collected via a second fiber located 4 circumferential cm from the incident source. Bakelite plastic rods (diameter = 3.175 mm) were painted black to provide perfectly light absorbing inhomogeneities. Measurements of $\theta(\rho_d)$ and $M(\rho_d)$ at 80 MHz were conducted as the rods were moved in tandem along the plane perpendicular to a line connecting the source and detector. Positioning was achieved with a motion controller (PMC200-P, Newport Corp., Irvine, CA) and a motorized actuator (Newport 850B). The actuator position was accurate to within 0.0050 mm. Phase and AC modulation were recorded as the distance between the center of the first absorbing cylinder and the wall of the phantom was varied from 0 cm to 5 cm in 20 increments. When the two objects were moved in tandem, their separation distances $(\rho_1 - \rho_2)$ between the centers of the two perfect absorbers were 6 mm, 10 mm, and 20 mm. Three measurements were taken at each position. Measurements of phase-shift and AC amplitude demodulation are reported relative to the absence case or θ_{inc} or M_{inc}.

3.2 Analytical prediction of phase-shift and amplitude modulation owing to two absorbing cylinders

In addition to the measurements of second-order interactions with the experimental approach described above, predictions of interactions between absorbers were computed analytically using Eqns. (11) through (15) upon employing a modified version of an algorithm written by D.A. Boas and available through the internet (http://www.lrsm.upenn.edu/pmi/PMI/pmi/html). Complex fluence incorporating first and second order scattering contributions were used to calculate phase-shift owing to two infinite cylinders that effectively act as perfect absorbers (μ_a = 2 cm^{-1}, μ_s'=10 cm^{-1}) in a turbid, semi-infinite medium mimicking our phantom (μ_a = 0.02 cm^{-1}, μ_s'=10 cm,$^{-1}$). Zero fluence boundary conditions were assumed and employed in the algorithm.

3.3 Numerical prediction of phase-shift and amplitude demodulation owing to two absorbing heterogeneities

In addition to experimental measurements and analytical calculations, two dimensional finite element computations were conducted in order to predict the phase-shift and amplitude demodulation owing to first order and second order interactions. The computations were performed on an Ultra 2 Sun Sparc workstation using a MATLAB® partial differential equation toolbox. The frequency domain diffusion equation for light propagation was solved to determine the fluence from an 80 MHz sinusoidally modulated light source. The simulated phantom was an infinite cylinder 16.5 cm in diameter. The optical properties of the medium were set to mimic the experimental conditions of 0.02 cm^{-1} for the absorption coefficient, μ_a, and 10 cm^{-1} for the isotropic scattering coefficient, μ'_s. The nearly perfect absorbers in these computations were modeled as infinite cylindrical rods and approximated by increasing the absorption coefficient to one hundred times that of the surrounding medium ($\mu_a = 2.0$ cm^{-1}). The scattering coefficient for the object was set to that of the surroundings ($\mu'_s = 10$ cm^{-1}) to mimic the analytical computations. The phantom was discretized into 66048 triangular elements containing 33281 nodes. A partial current boundary condition was used to approximate light reflection and transmission across the boundary of the phantom as would be expected in the experimental measurements. While our meshing did not permit representation of the perfect absorber as a volume excluded for light transport, we approximated the heterogeneity with a high absorption coefficient since others have shown that the propagation characteristics are comparable.[18] It is noteworthy that while these computations do not exactly mimic the experimental measurements described below, they nonetheless adequately describe the contributions of second order scattering effects. The forward solution was obtained for each absorbing cylinder alone and then in combination. The results were analyzed similar to the experimental results using Eqns. (7) and (8).

4.0 Results and Discussion

4.1 Experimental results

Figures 4a through 4c and Figures 5a through 5c illustrate the phase-shift and amplitude demodulation changes as a function of position of the pair of perfect absorbers whose centers are separated by 6 mm, 10 mm, and 20 mm. The symbols denote individual measurements of phase-shift difference in the presence of the two hidden objects while the symbols connected by the lines denote the phase-shift and amplitude demodulation calculated from Eqns (7) and (8) with measurements made in the absence and in the presence of a single individual absorber. The measured values of phase-shift and amplitude demodulation denoted by the open symbols are therefore reflective of higher order contributions while the solid line reflects only first order contributions. Paired student t-test shows that there is significant difference ($p<0.005$) between the set of phase-shift and amplitude demodulation measurements and that predicted by Eqns (7) and (8) for two perfect light absorbing objects separated by 6, 10, and 20 mm and positioned at varying distances away from the source and detector (Figures 4a through 5c). Our results also show that second order effects are greatest for two absorbing heterogeneities spaced 6 mm apart and become smaller in magnitude at 10 and 20 mm. Paired t-test indicate there are significant differences at the 99.5% confidence levels (indicated by the astericks in Figure 4) between individual experimental phase-shift values that reflect first and higher order scattering contributions to the detected signal and those computed values that are indicative of first order effects only. From the data for 6 mm absorber separation illustrated in Figure

4a, it can be seen that the actual experimental measurements of phase-shift change due to two objects is smaller than that predicted by Eqn (7) in which second and higher order perturbations are not accounted for. At greater distances away from the source and detector, agreement between experimental and predicted phase-shift change suggests that second order effects may indeed be negligible, even in the case of the smallest separation, but only in a region where the objects' contribution to the detected signal is comparatively small. This is reasonable since second order effects are expected to increase with proximity to the source and detector. From our studies, it appears that separations greater than 20 mm are necessary for their accurate resolution via perturbative reconstruction approaches when perfect absorbers are involved.

4.2 Analytical computations

Our experimental results are also validated by the analytical predictions which account for first and second order scattering contributions. Figures 6a through 6c depict the qualitative trends seen in the experimental data presented for phase difference in Figures 4a through 4c. There appears to be good agreement between the trends observed experimentally with varying separation distances and analytical predictions. Specifically, higher order contributions significantly perturb the detected phase-shift values when the separations between the center of two absorbing cylinders are 6 mm (Figure 6a) and 10 mm (Figure 6b). The contribution of higher order scattering from cylindrical absorbers is not significant when the separation distance is 20 mm (Figure 6c). However upon comparison to experimental results, there are differences in the absolute magnitude and shape of the phase shift change versus object distance. These distances are most likely due to the differences in the boundary conditions, geometry, and absorber strength between the analytical and experimental results. Nonetheless, the trends confirm experimental results that the presence of second order perturbations reduces the phase shift change owing to two light-absorbing bodies. Neglecting second order effects could cause an underestimation of absorption strength or size when reconstruction algorithms based upon first order perturbations are used.

In addition, we investigated the variation of second order perturbations with modulation frequency as shown in Figure 7. The simulated data of phase-shift change versus position of the heterogeneities is depicted for two cylindrical absorbers (d = 3.125 mm, μ_a=2 cm^{-1}) separated by 6 mm in a semi-infinite medium Again, the phase-shift is reported relative to the absence case and the distance is reported from the wall to the center of the first cylinder. Three frequencies were evaluated: 80, 160, and 240 MHz. The absolute value of phase shift increases with frequency, but the contribution of second order effect remains roughly the same absolute value. Consequently, the error in assuming negligible second order scattering effects becomes smaller at increasing frequencies. This is expected since increased damping of a re-scattered photon density wave occurs at higher modulation frequencies. While these results intimately depend upon the choice of optical properties, they nonetheless point out that the error in neglecting second order scattering contributions in analytically-based reconstructions becomes smaller with increasing modulation frequencies. Of course, the error reduction occurs at the expense of interrogating a smaller volume of tissue with a source modulated at an increased frequency.[20]

4.3 Finite element computations

Our experimental results were not only validated by analytical predictions but also with finite element computations. Figures 8a - 9c show the numerical computations that correspond to the experimental phase-shift data presented in Figures 4a-5c. Again there appears to be good agreement between the trends of the experimental and analytical results with that of the numerical solutions. Also, higher order contributions perturb the detected phase-shift values when the separation distance between the two rods are 6 mm (Figure 8a) and 10 mm (Figure 8b). The contribution of higher order scattering from the cylindrical absorbers is not significant when the separation distance is 20 mm (Figure 8c). Figures 9a- 9c show the amplitude demodulation relative to an absence condition. The modulation data also shows similar results to that obtained experimentally. These computations results confirm that the presence of second order perturbations are important for two light absorbing objects that are less than 20 mm apart.

5.0 Conclusions

In summary, our experimental measurements show that the contributions of higher order scattering of propagating photon density waves may not always be insignificant. While our analytical and numerical computations do not exactly reproduce experimental conditions (i.e., 2-D finite element, semi-infinite geometry, etc.), they nonetheless demonstrate that the experimental trends can be attributed to second order effects. Under conditions of high contrast owing to absorption, analytical approaches to the inverse imaging algorithm may restrict the resolution and sensitivity of biomedical optical imaging performed in the frequency-domain. An analogy can also be drawn for time-domain and CW reconstruction approaches which do not deploy full solutions to the diffusion equation to account for the interdependence of voxel optical properties on measured fluences. Certainly, our results are based upon the worst case scenario of perfect absorbers, and may have less impact on the image reconstructions involving imperfect absorbers. Under conditions in which multiple heterogeneities are contrasted from their surroundings on the basis of scattering or fluorescence, the first order perturbation assumption may not be as restrictive. Indeed, if the non-linearity associated with second order scattering effects are small, then non-iterative Born and Rytov approximations are especially attractive since image reconstruction are not computational intensive. Nonetheless, our results suggest that inverse imaging algorithms that depend solely upon first order perturbations due to local changes in tissue absorption properties may not provide as accurate a reconstruction when compared to those algorithms that depend upon the full numerical calculation of the diffusion equation with specified boundary conditions.

6.0 Nomenclature

a_k	Radius of cylinder k, [cm].
c_n	Speed of light through the medium, [cm/sec].
D	Optical diffusion coefficient of homogeneous medium, [cm].
D_k'	Diffusion coefficient inside the cylinder, [cm].
I_n	Modified Bessel function.
I_n'	Derivative of modified Bessel function, I_n.
K_n	Modified Bessel function.
K_n'	Derivative of modified Bessel function, K_n.
M	AC demodulation of the incident light, [mW/cm^2].
m	Number of objects.
p	Integration variable in Helmholtz equation. describing scatter from an infinite cylinder, [cm^{-1}].
S_{source}	Strength of modulated source at position ρ_s, represented as a complex number of amplitude and phase[mW] .
x	Variable in Helmholtz equation describing scatter from an infinite cylinder, [cm^{-1}].
y	variable in Helmholtz equation describing scatter from an infinite cylinder, [cm^{-1}].
z	Axial direction of the cylindrical heterogeneities, [cm].

Greek:

Φ	Photon fluence, [mW/cm^2].
Φ_{inc}	Photon fluence of incident wave or in the absence of heterogeneities, [mW/cm^2].
Φ_{scat}	Photon fluence arising from scattered wave, [mW/cm^2].
ρ	Position vector, [cm].
ρ_s	Position of the source, [cm].
ρ_d	Position of detector, [cm].
ρ_k	Center position of object k, [cm].
θ	Phase shift of light wave, [degrees or radians].
ϑ	Angle between ρ_s and ρ_d.
μ_a	Absorption coefficient of homogeneous surroundings, [cm^{-1}].
μ_s'	Isotropic scattering of homogeneous surroundings, [cm^{-1}].
μ_a'	Absorption coefficient of cylinder, [cm^{-1}].
μ_s''	Isotropic scattering of cylinder, [cm^{-1}].

subscripts and superscripts

n	Order of perturbation or nth order scattering effect.
k	Index denoting cylindrical object one, k1, two, k2, or both objects k1,k2.
inc	Index denoting absence measurement or condition.

7.0 Acknowledgment

This work was supported in part by the National Institutes of Health, [R01 CA61413, R01 CA67176, K04 CA68374] and the U.S. Army Medical Research Breast Cancer Program, [DAMD17-96-1-6023].

8.0 References

1. Wang, L.M., Ho, P.P., and R.R. Alfano, "Double-stage picosecond Kerr gate for ballistic time-gated optical imaging in turbid media," Appl. Optics, 32, 535 (1994).

2. Das, B.B., Yoo, K.M., and R.R. Alfano, "Ultrafast time-gated imaging in thick tissues: a step toward optical mammography," Opt.Lett. 18, 1092-1094 (1993).

3. Demos, SG.; Savage, H.; Heerdt, Alexandra S.; Schantz, S., and R.R. Alfano, RR., "Time resolved degree of polarization for human breast tissue," Optics Communications v 124, 439-442 (1996).

4. Singer, J.R., F.A. Grunbaum, F.A., Kohn, P., and J.P. Zubelli, "Image Reconstruction of the interior of bodies that diffuse radiation," Science 248, 990-993 (1990).

5. Hebden, J.C., Kruger, R.A., and K.S. Wong, "Time-resolved imaging through a highly scattering medium," Appl. Opt. 30, 788-794 (1991).

6. O'Leary, M.A., D.A. Boss, B. Chance, and A.G. Yodh, "Experimental images of heterogeneous turbid media by frequency-domain diffusing photon tomography," Opt. Lett. 20, 426-428 (1995).

7. Jiang, H. , K.D. Paulsen, U.L. Osterberg, B.W. Pogue, and M.S. Patterson, "Simultaneous reconstruction of absorption and scattering maps in turbid media from near-infrared frequency-domain data," Opt. Lett. 20, 2128-2130 (1995).

8. Jiang, H., K.D. Paulsen, and U.L. Osterberg, "Optical image reconstruction using frequency domain data: simulations and experiments," J. Opt. Soc. Am. A13, 253-266 (1996).

9. Franceschini, M.A., Moesta, K.T., Fantini, S., Gaida, G., Gratton, E., Jess, H., Mantulin, W.W., Seeber, M., Schlag, P.M. and Kaschke, M."Frequency-domain techniques enhance optical mammography: initial clinical results. Proc. Natl. Acad. Sci. USA *in press.*

10. Sevick, E.M., J.R. Lakowicz, H. Szmacinski, K. Nowaczyk, and M.L. Johnson, "Frequency domain imaging of absorbers obscured by scattering," J. Photochem. Photobio., B: Biol 16, 169-185 (1992).

11. Gratton, E., W. Mantulin, M.J. van de Ven, J. Fishkin, M. Maris, and B. Chance, "A novel approach to laser tomography," Bioimaging 1, 40-46 (1993).

12. Barbour, R.L., H.L. Graber, Y. Wang, J.H. Chang, and R. Aronson, "A perturbation approach for optical diffusion tomography using continuous-wave and time resolved data," Proc. SPIE 1511, 87-120 (1993).

13. Arridge, S.R., van der Zee, P., Cope, M. and D.T. Delpy, "Reconstruction methods for infra-red absorption imaging," SPIE, 1431, 204-215 (1991).

14. Arridge, S.R., Schweiger, M., Hiraoka, M., and D.T. Delpy, "Performance of an iterative reconstruction algorithm for near-infrared absorption and scatter imaging," SPIE, 1888, 360-371 (1993).

15. Boas, D.A., O'Leary, B., Chance, B., and A.G. Yodh, "Scattering of diffuse photon density waves by spherical inhomogeneities within turbid media: analytical solution and applications," Proc. Natl. Acad. Sci., USA 91, 4887-4891 (1994).

16. Yao, Y. , Wang, Y., Pei, Y., Zhu, W., and R.L. Barbour, "Frequency-domain optical imaging of absorption and scattering distributions by a Born iterative method," JOSA 14, 325-342 (1997).

17. Arridge, S.R., Cope, M., and D.T. Delpy, "The theoretical basis for the determination of optical pathlengths in tissue: temporal and frequency-domain analysis," Phys. Med. Biol. 37, 1531-1560 (1992).

18. van de Hulst, H.C., Light scattering by small particles, Dover, New York, 1981.

19.Hutchinson, C.L., Troy, T.L., and E.M. Sevick-Muraca. "Fluorescence-lifetime determination in tissues and other random media from measurement of excitation and emission kinetics," Appl. Optics, 35, 2325-2332 (1996).

20. Sevick, E.M., Frisoli, J.K., Burch, C.L. and J. R. Lakowicz, "Localization of absorbers in scattering media by use of frequency-domain measurements of time-dependent photon migration," Appl. Optics 33, 3562-3570 (1994).

9.0 List of Figures

Figure 1 Schematic illustrating (i) the incident wave, Φ_{inc}, originating from the source at position, ρ_s (dashed lines); (ii) the first order scattered wave, $\Phi^{n=1}_{scat,k1}$ arising from the first heterogeneity (solid lines), and (iii) the second order wave, $\Phi^{n=2}_{scat,k2}$ arising from re-scatter of the first order wave off of the second heterogeneity.

Figure 2 Schematic detailing the geometry used in the calculation of scattered waves from analytical expression. The centroid of the cylinder is the origin with z denoting the length, angle ϑ denoting the angle in the plane containing the source and detector, and r denoting the radial direction.

Figure 3 Schematic illustrating the geometry of the experimental measurements.

Figure 4 Experimental values of $\theta_{k1,k2} - \theta_{inc}$ [degrees] relative to the

igure 4 Experimental values of $\theta_{k1,k2}$ - θ_{inc} [degrees] relative to the absence condition as a function of distance from the source-detector pair. The symbols denote individual measurements in the presence of two cylinders separated by a distance (a) 6 mm, (b) 10 mm, and (c) 20 mm while the line connects predictions from Eqn (7) and measurements of θ_{k1}, θ_{k2}, and θ_{inc}. The error bars denote the propagation of measurement errors (standard deviation) associated with θ_{k1}, θ_{k2}, and θ_{inc}. The x-axis is reported as the distance between the wall and the first cylinder (k1). The astericks denote significant difference ($p<0.005$, paired student t-test) between the values experimentally measured and obtained from Eqn (7).

Figure 5 Experimental values of $M_{k1,k2}$ / M_{inc} [arbitrary units] relative to the absence condition as a function of distance from the source-detector pair. The symbols denote individual measurements in the presence of two cylinders separated by a distance (a) 6 mm, (b) 10 mm, and (c) 20 mm while the line connects predictions from Eqn (8) and measurements of M_{k1}, M_{k2}, and M_{inc}. The error bars denote the propagation of measurement errors (standard deviation) associated with M_{k1}, M_{k2}, and M_{inc}. The x-axis is reported as the distance between the wall and the first cylinder (k1).

Figure 6 Values of $\theta_{k1,k2} - \theta_{inc}$ [degrees] predicted from analytical prediction of first order (solid line) and inclusive of second order (dashed line) scattering effects as a function of distance [cm] from the source-detector pair for two absorbing cylinders separated by (a) 6 mm, (b) 10 mm, and (c) 20 mm. The x-axis is reported as the distance between the wall and the first cylinder (k1) and the phase-shift reported relative to the absence case.

Figure 7 Finite element computations of $\theta_{k1,k2} - \theta_{inc}$ [degrees] relative to an absence condition for considering only first order (solid line) and including second order (dashed line) perturbations as a function of distance [cm] from the source-detector pair for absorbing cylinders separated by (a) 6 mm, (b) 10 mm and (c) 20 mm. The x-axis is reported as the distance between the wall and the first cylinder (k1) and the phase-shift reported relative to the absence case.

Figure 8 Finite element computations of $M_{k1,k2}/M_{inc}$ [arbitrary units] referenced to an absence condition for both the first order (solid line) and the second order (dashed line) perturbations as a function of distance [cm] from the source-detector pair for absorbing cylinders separated by (a) 6 mm, (b) 10 mm and (c) 20 mm. The x-axis is reported as the distance between the wall and the first cylinder (k1) and the modulation ratio reported relative to the absence case.

Figure 1

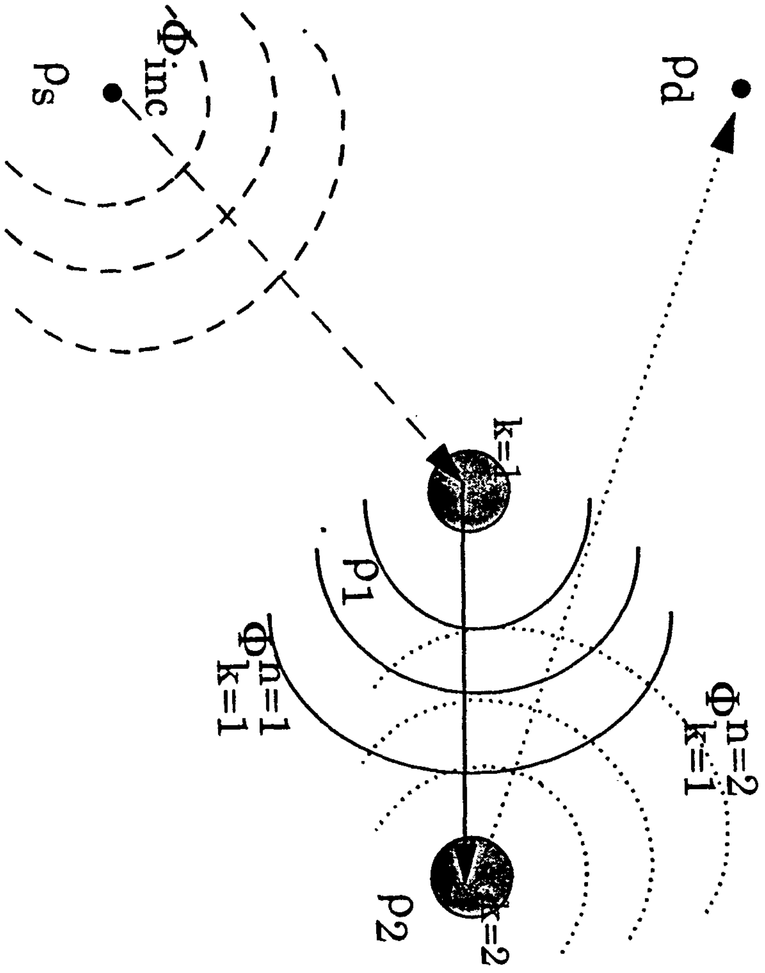

Φ_{inc}
ρ_s
ρ_d
k=1
ρ_1
$\Phi^{n=1}_{k=1}$
$\Phi^{n=2}_{k=1}$
ρ_2
k=2

Sevick-Muraca 1

Figure 2

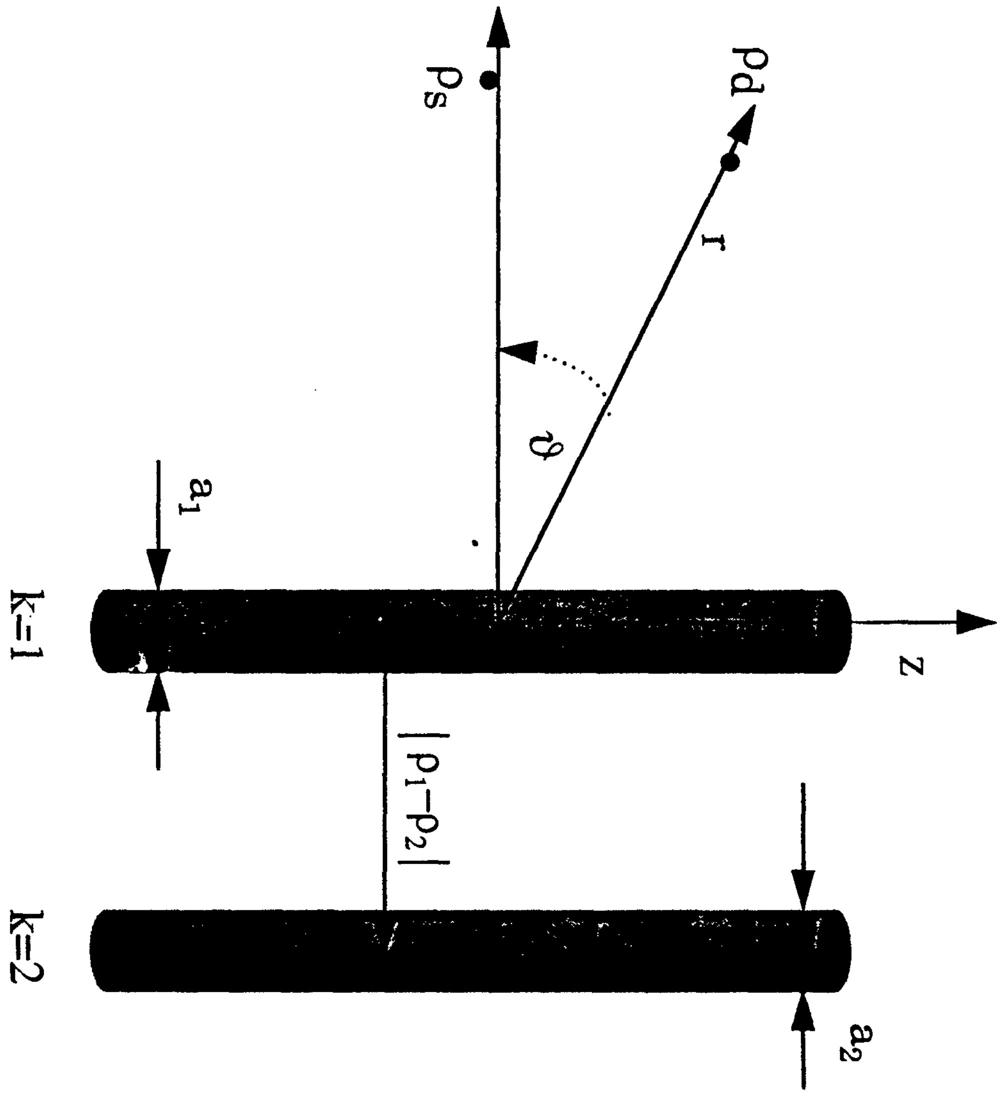
ρs
ρd
r
ϑ
a1
k=1
z
|ρ1−ρ2|
k=2
a2

Sevick-Muraca 2

Figure 3

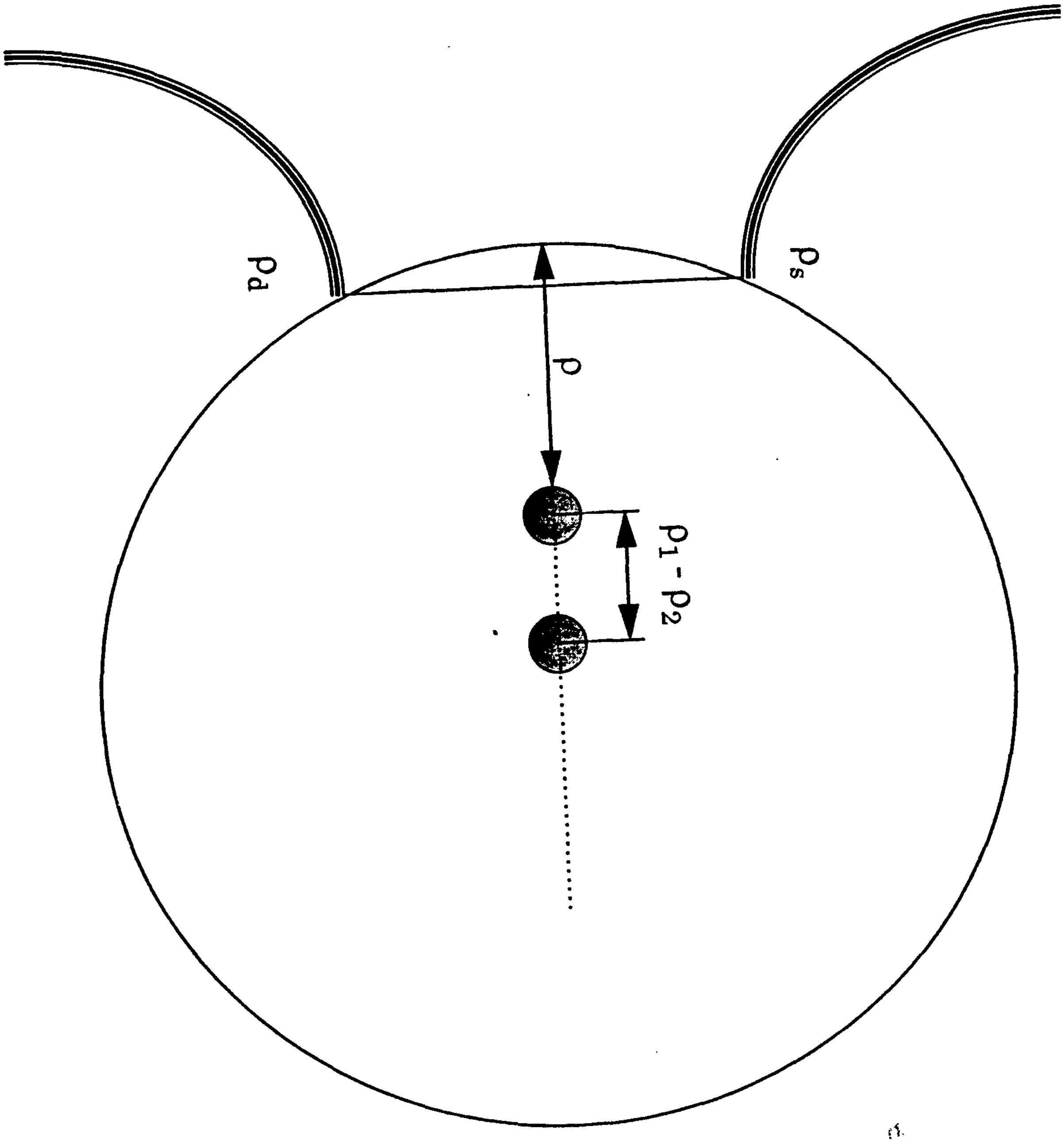
ρ_d
ρ_s
ρ
$\rho_1 - \rho_2$

Sevick-Muraca 3

Figure 4a

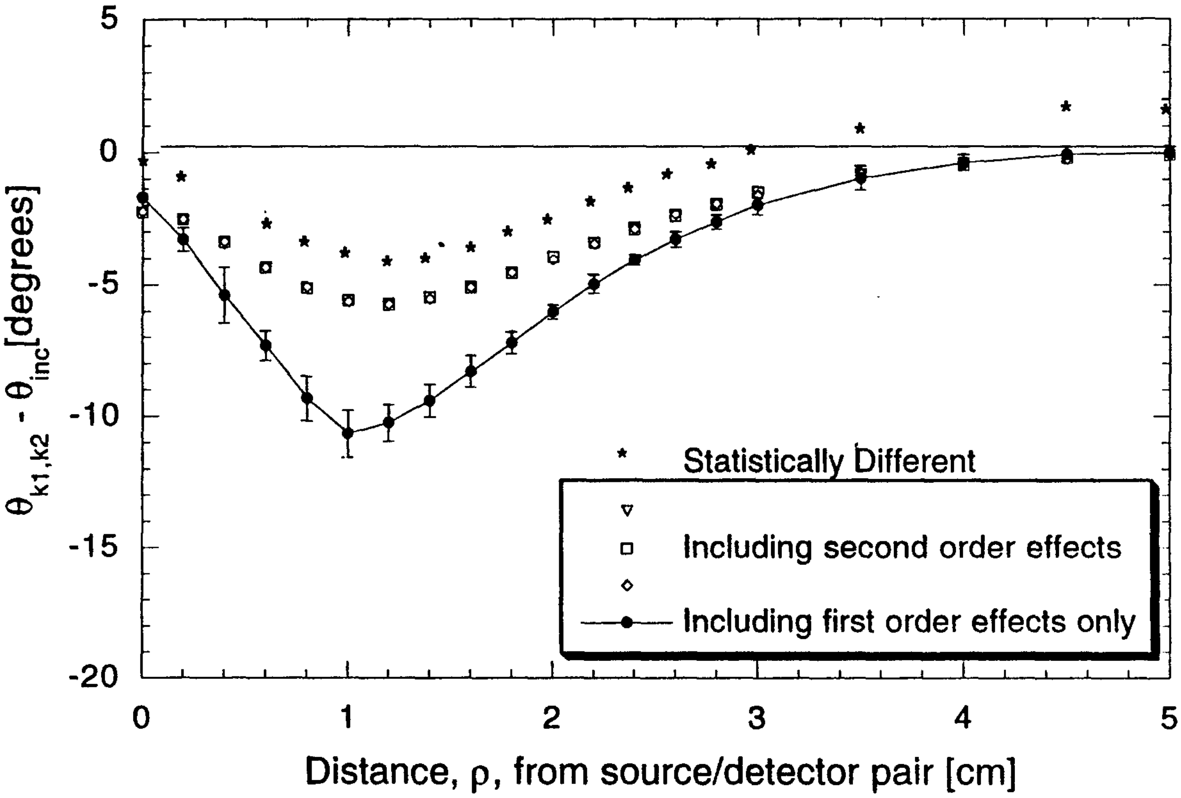

Sevick - Muraca 4a

Figure 4b

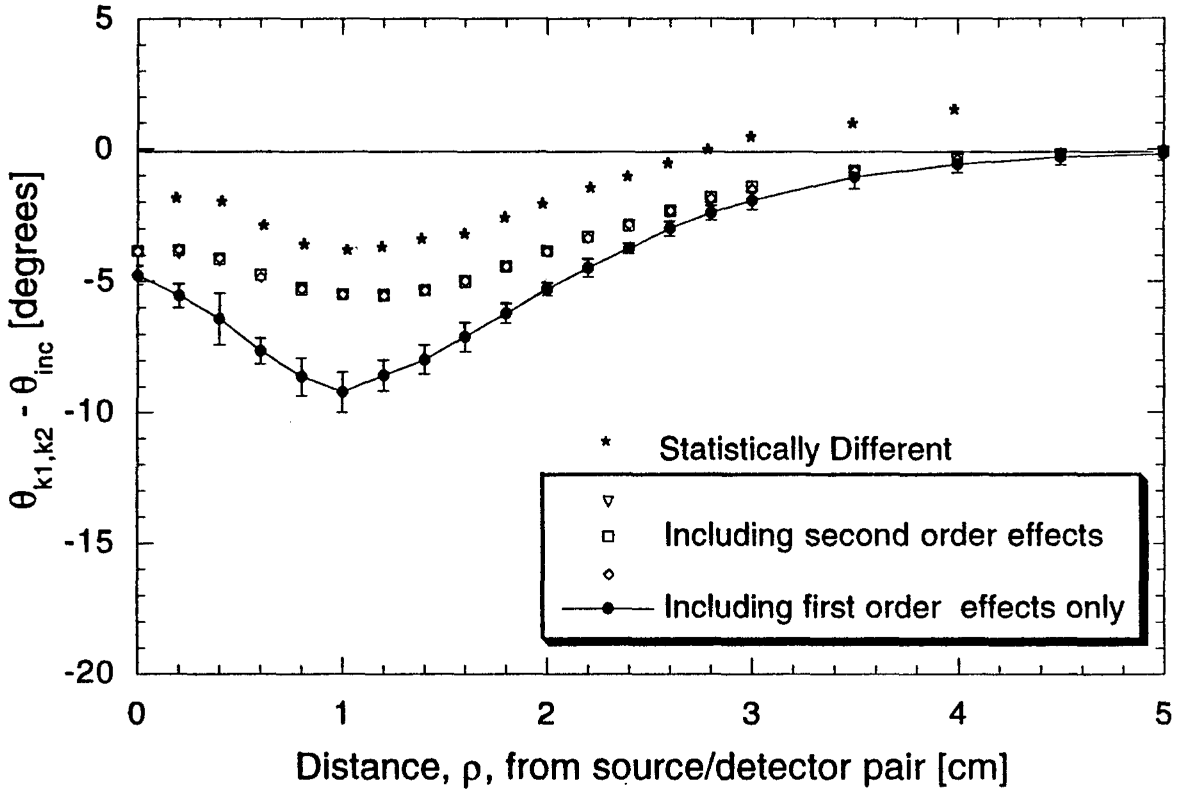

Sevick-Muraca 4b

Figure 4c

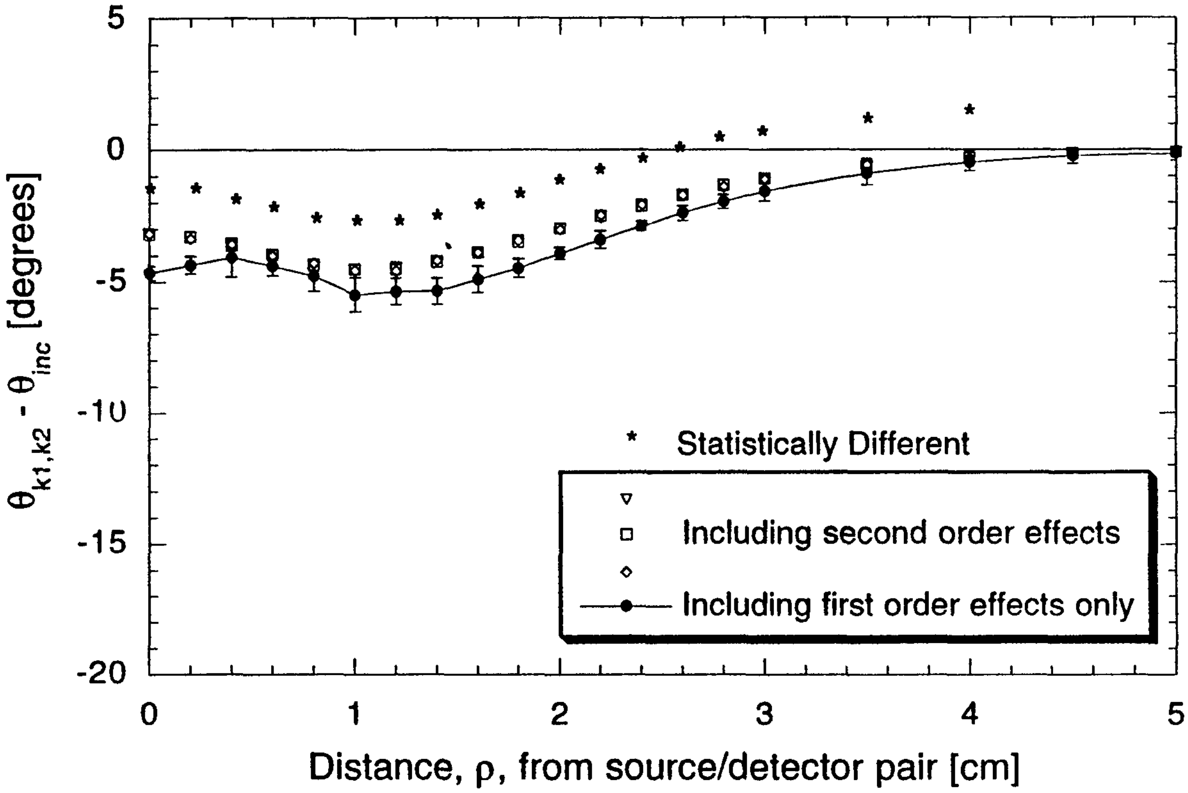

Sevick-Muraca 4c

Figure 5a

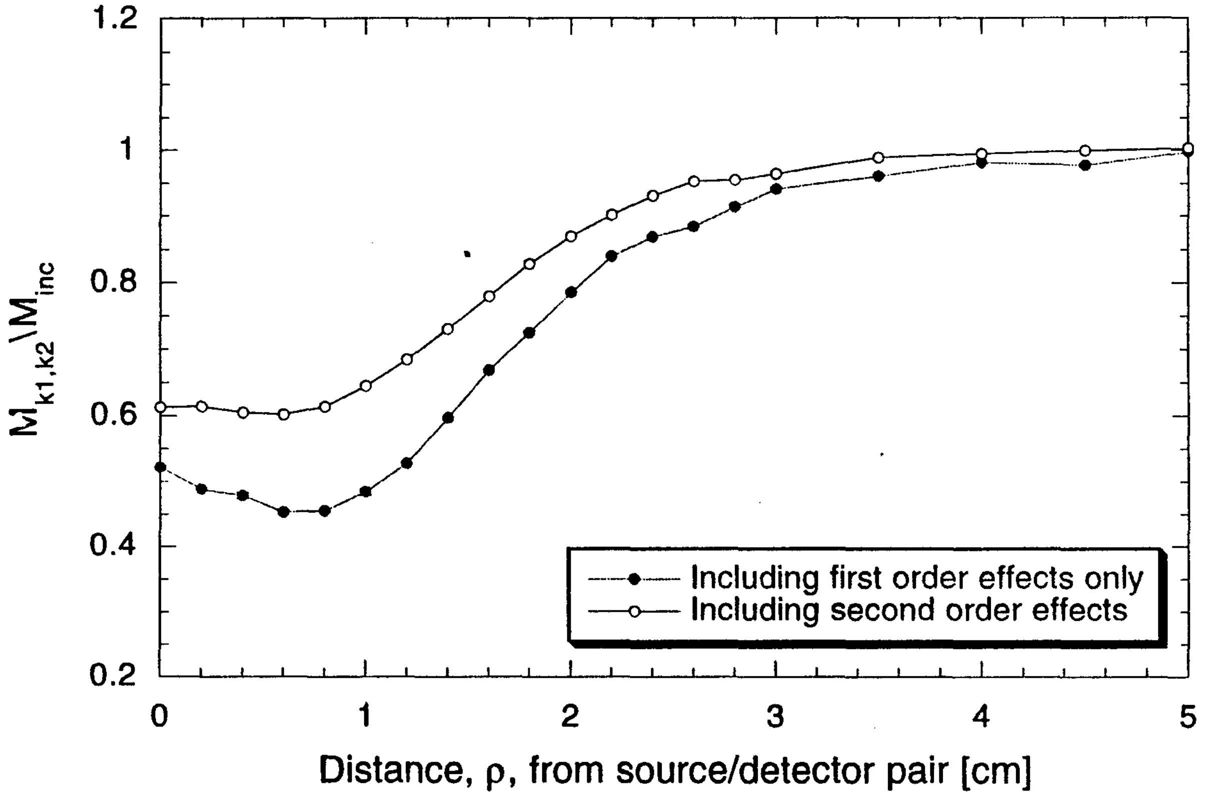

Sevick-Muraca 5a

Figure 5b

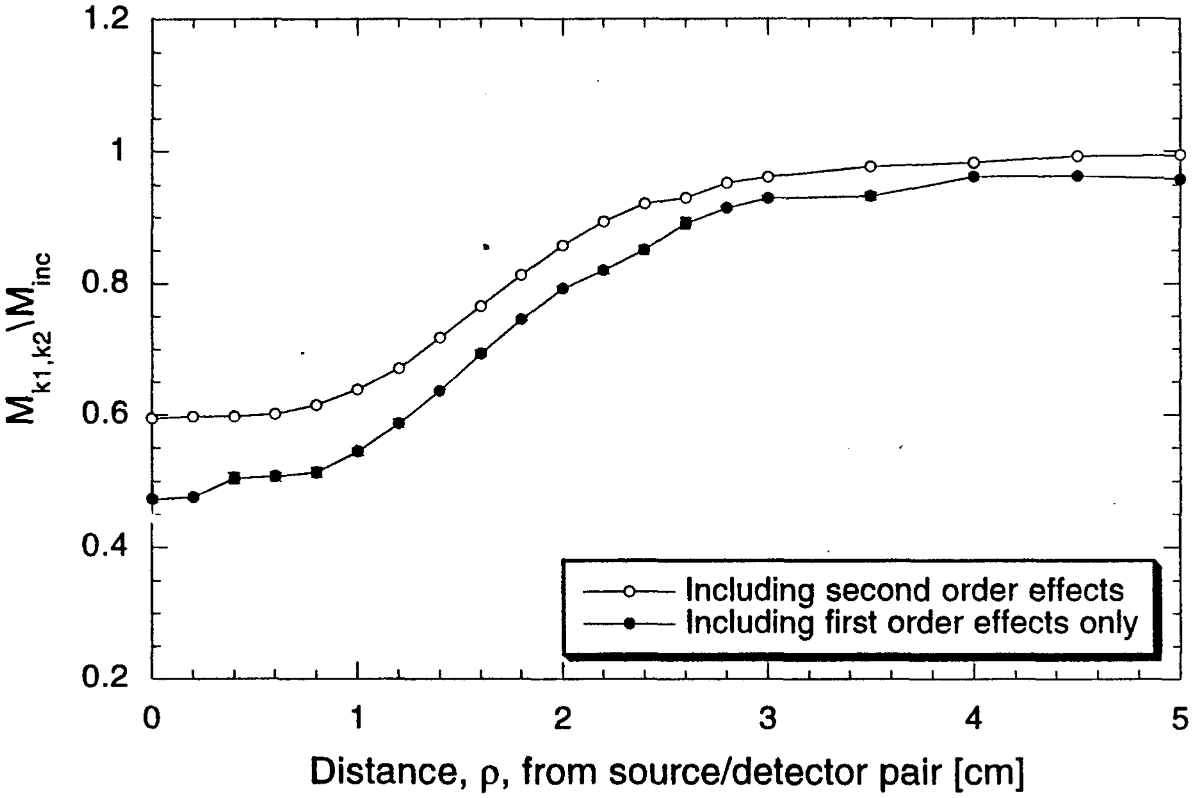

Sevick-Muraca 5b

Figure 5c

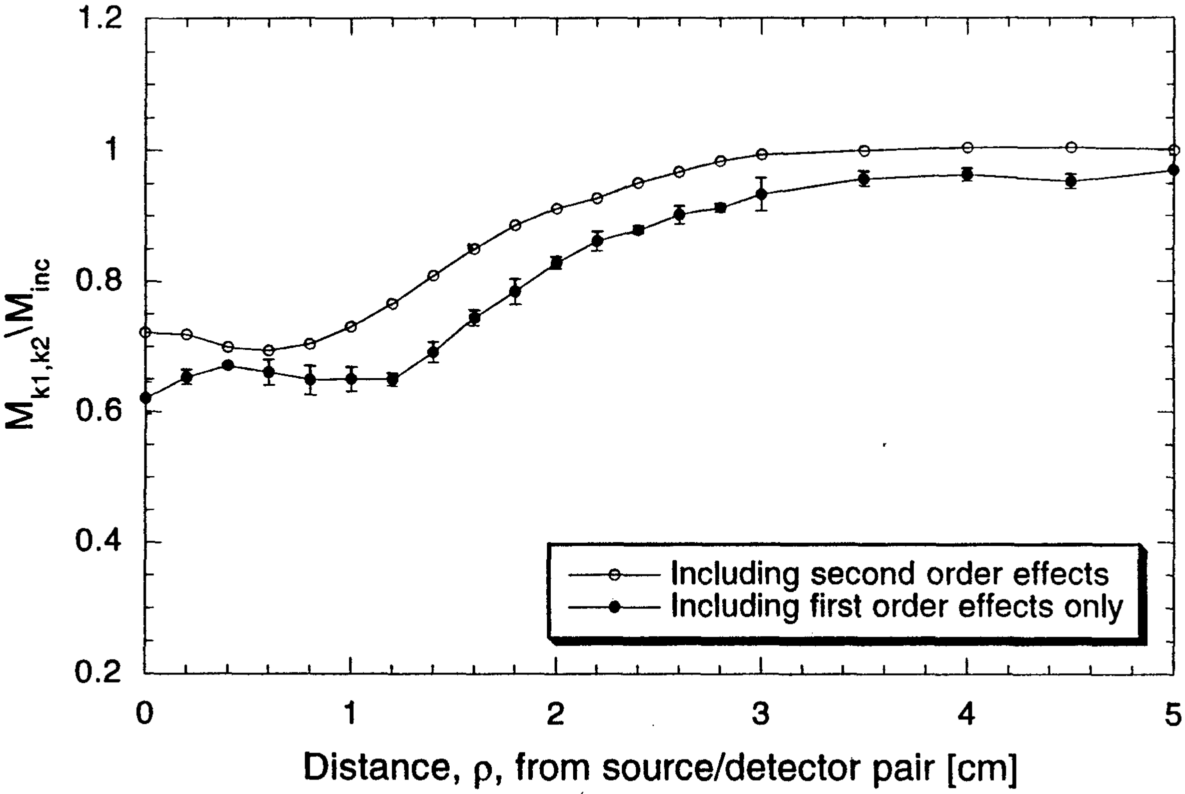

Sevick-Muraca 5c

Figure 6a

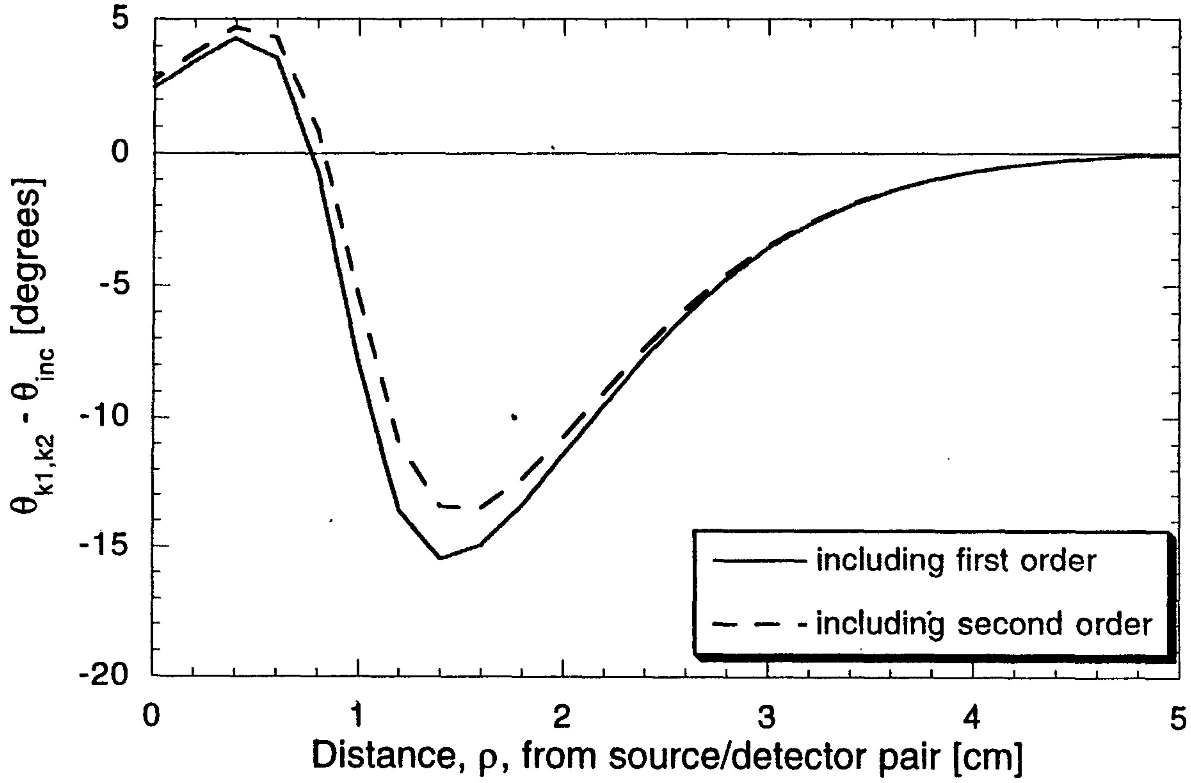

Sevick-Muraca 6A

Figure 6b

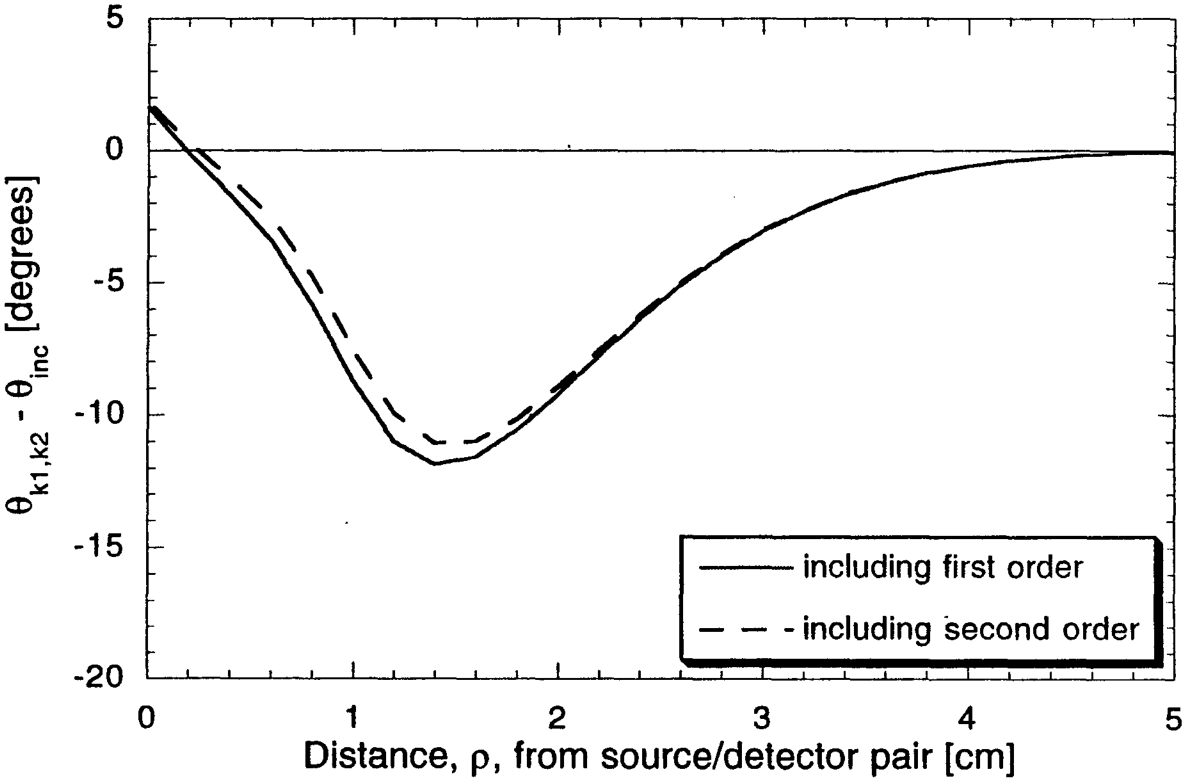

Sevick-Muraca 6b

Figure 6c

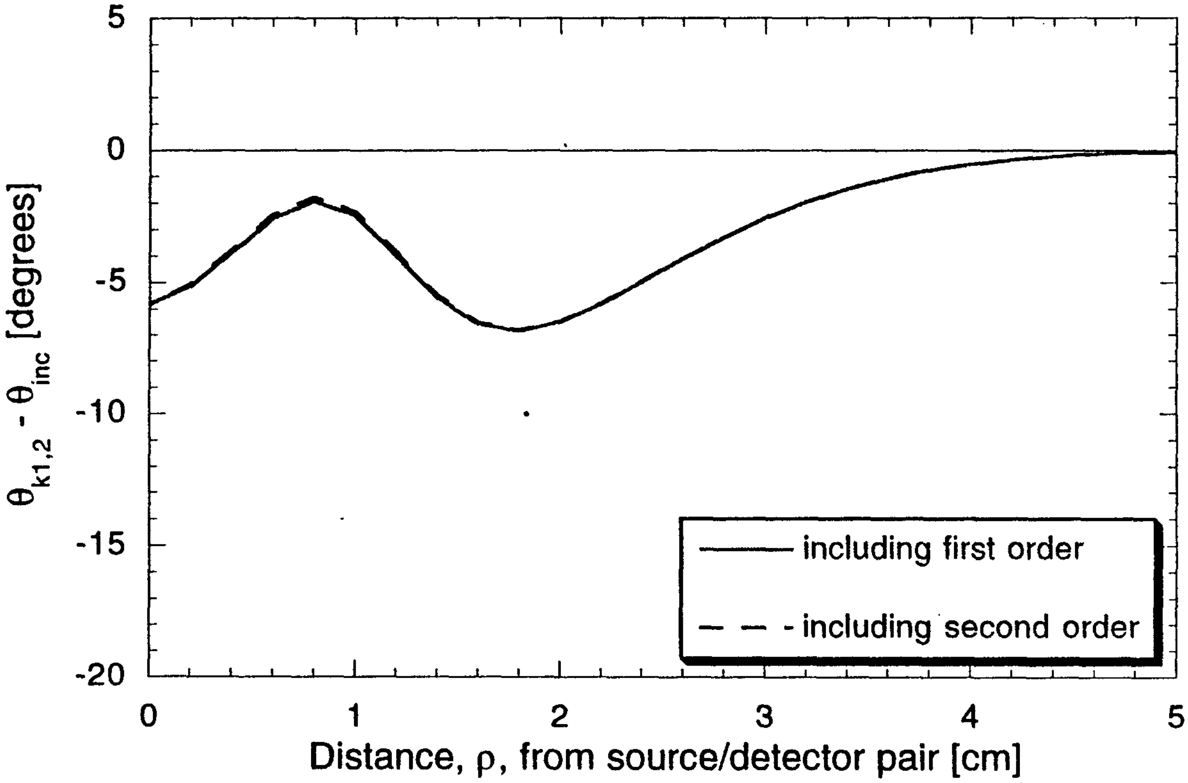
5
0
-5
-10
-15
-20
$\theta_{k1,2} - \theta_{inc}$ [degrees]
0
1
2
3
4
5
Distance, ρ, from source/detector pair [cm]
including first order
including second order

6c

Figure 7

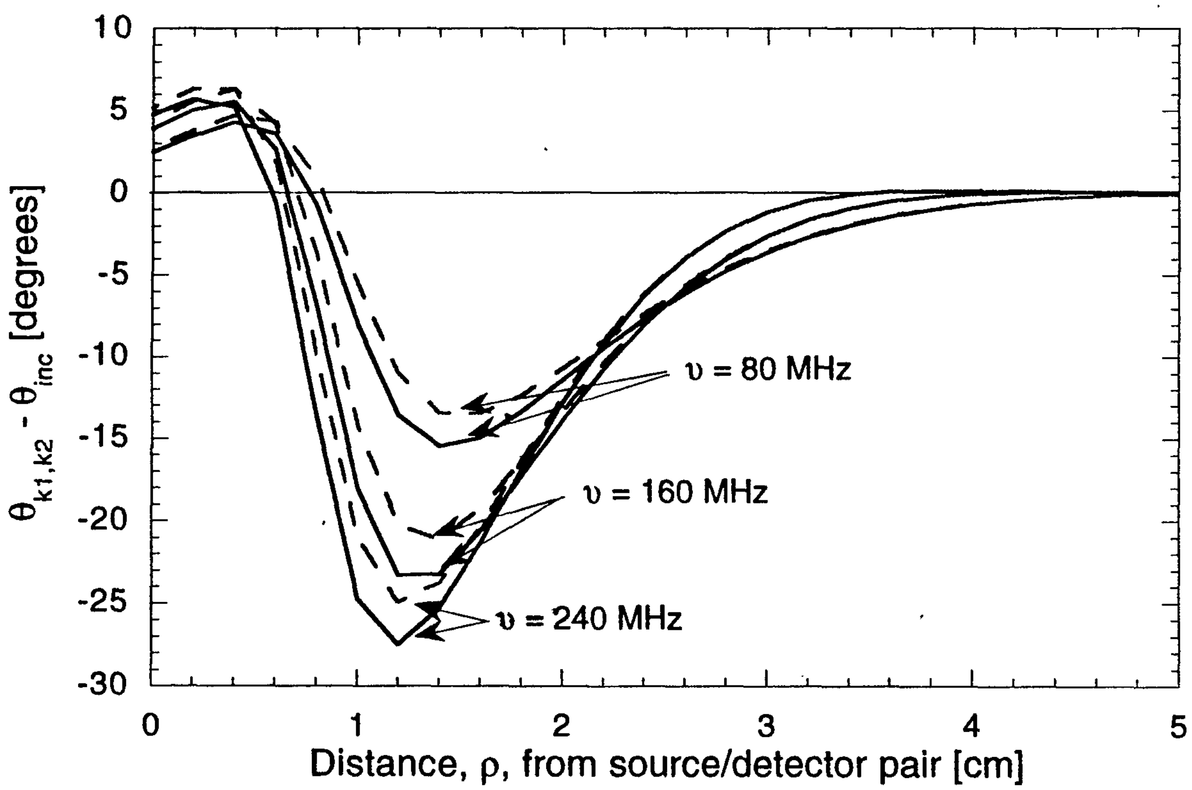
10
5
0
-5
-10
-15
-20
-25
-30
0
1
2
3
4
5
$\theta_{k1,k2} - \theta_{inc}$ [degrees]
Distance, ρ, from source/detector pair [cm]
υ = 80 MHz
υ = 160 MHz
υ = 240 MHz

Figure 8a

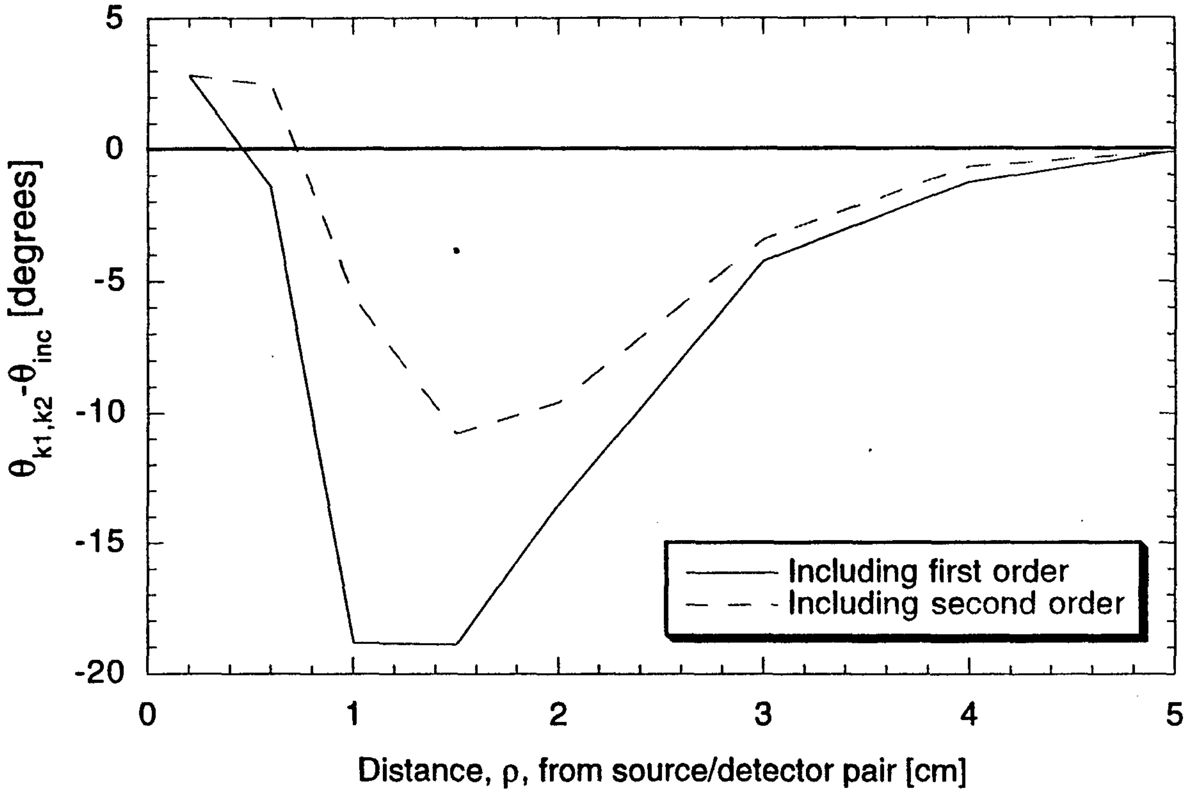

Sevick Muraca 8a

Figure 8b

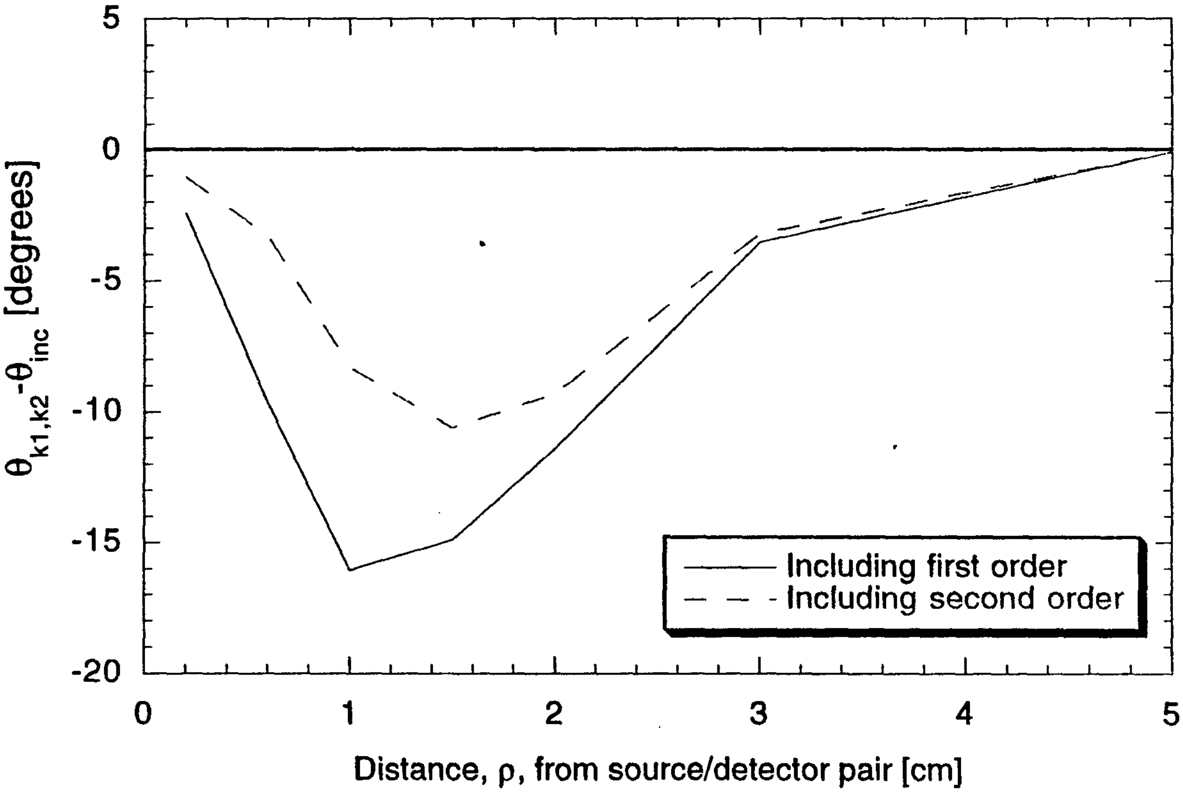

5
0
-5
-10
-15
-20
0
1
2
3
4
5
$\theta_{k1,k2}-\theta_{inc}$ [degrees]
Distance, ρ, from source/detector pair [cm]
Including first order
Including second order

8b

Figure 8c

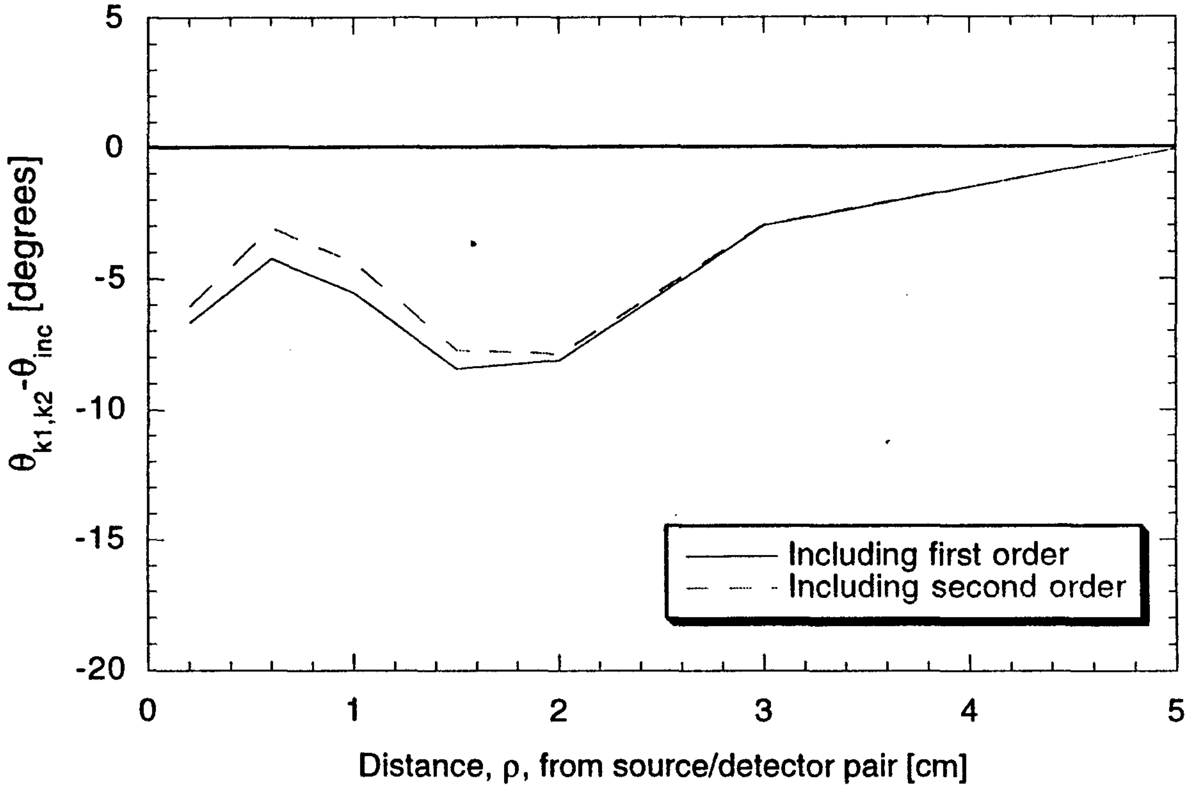

Sevick-Muraca 8C

Figure 9a

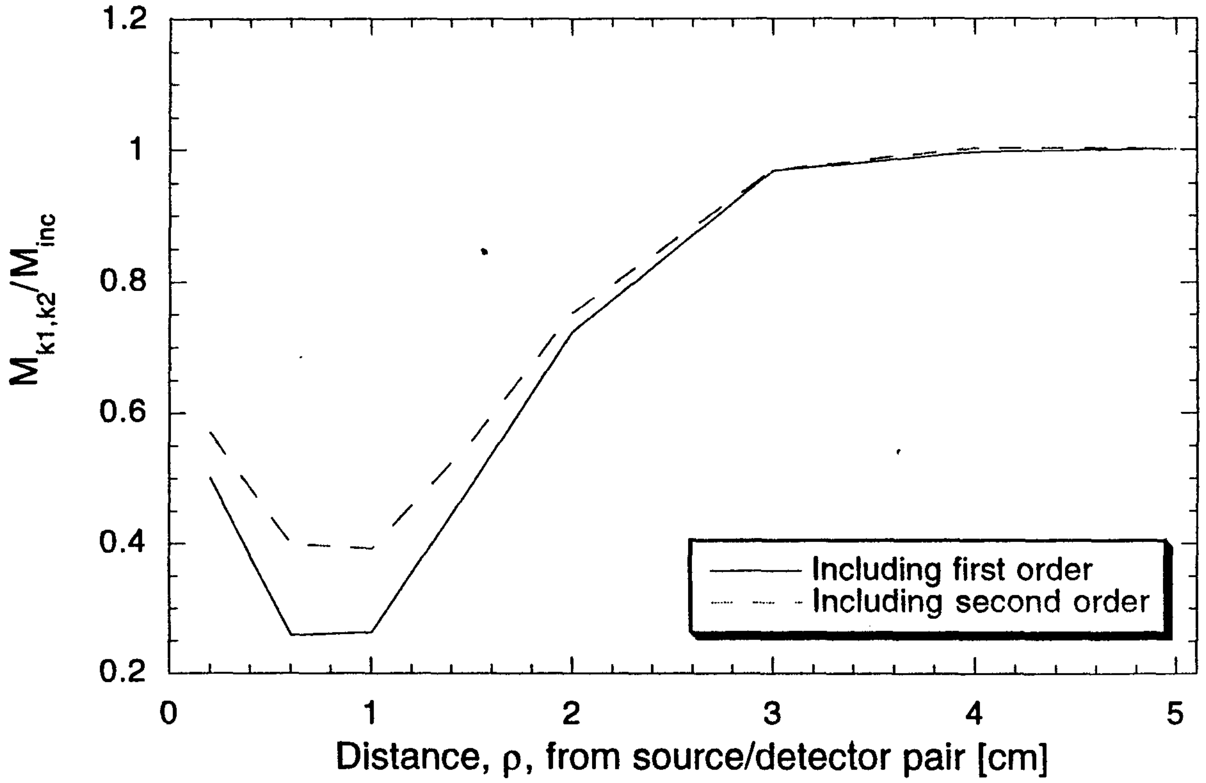

Sevick-Muraca 9a

Figure 9b

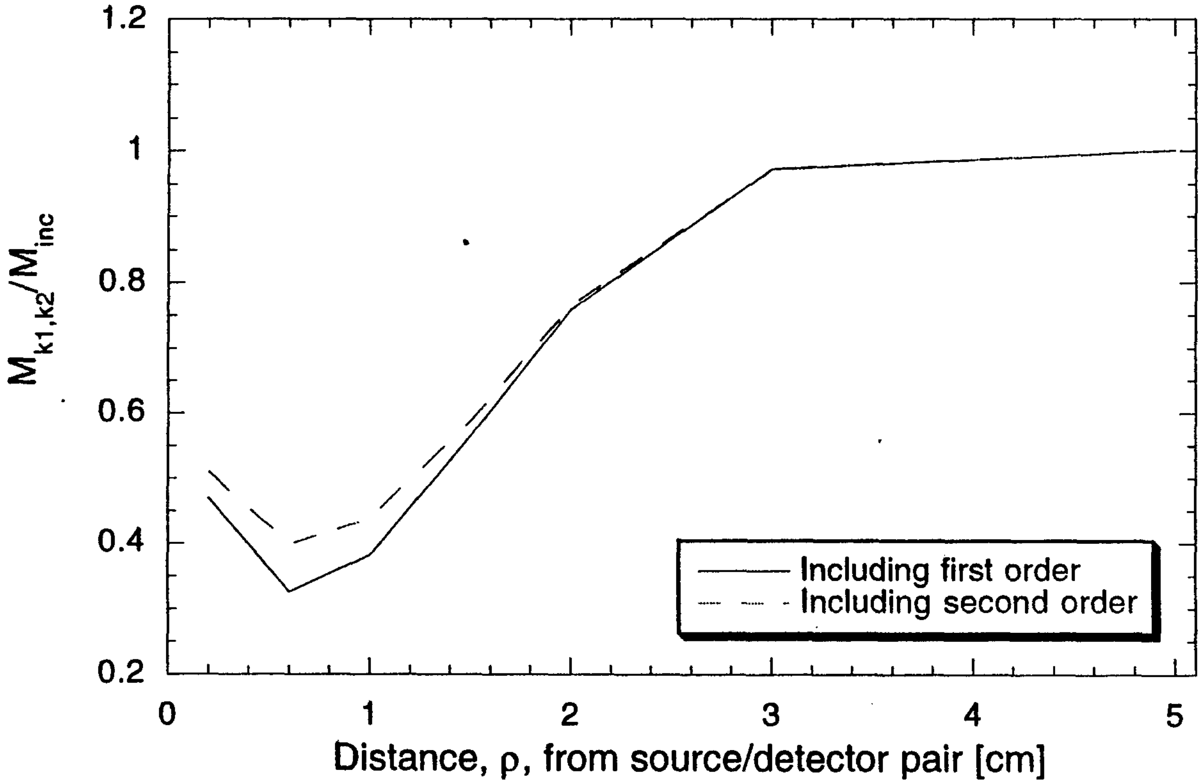

Sevick-Muraca 96

Figure 9c

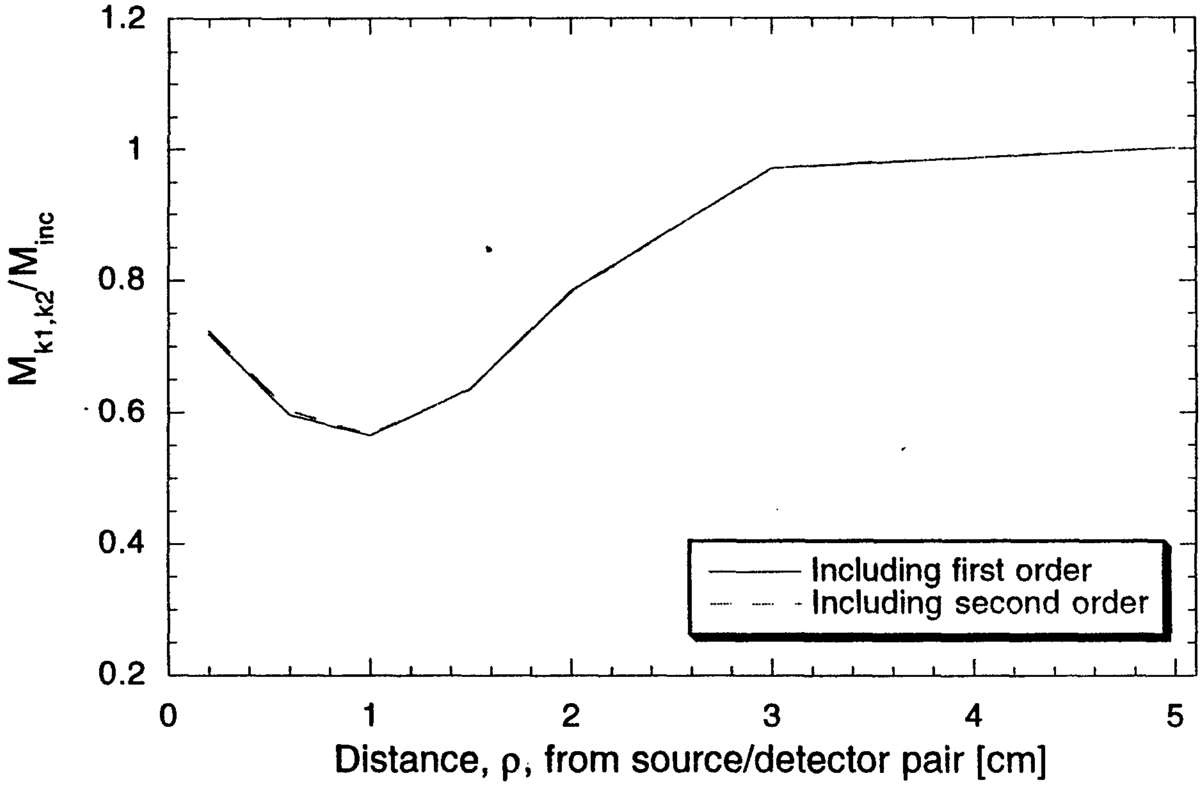

Sevick-Muraca 9c

DEPARTMENT OF THE ARMY
US ARMY MEDICAL RESEARCH AND MATERIEL COMMAND
504 SCOTT STREET
FORT DETRICK, MARYLAND 21702-5012

REPLY TO
ATTENTION OF:

MCMR-RMI-S (70-1y)

21 JUN 2001

MEMORANDUM FOR Administrator, Defense Technical Information Center (DTIC-OCA), 8725 John J. Kingman Road, Fort Belvoir, VA 22060-6218

SUBJECT: Request Change in Distribution Statement

1. The U.S. Army Medical Research and Materiel Command has reexamined the need for the limitation assigned to technical reports. Request the limited distribution statement for reports on the enclosed list be changed to "Approved for public release; distribution unlimited." These reports should be released to the National Technical Information Service.

2. Point of contact for this request is Ms. Judy Pawlus at DSN 343-7322 or by e-mail at judy.pawlus@det.amedd.army.mil.

FOR THE COMMANDER:

Encl

PHYLIS M. RINEHART
Deputy Chief of Staff for
Information Management

DAMD17-94-J-4413	ADB261602
DAMD17-96-1-6112	ADB233138
DAMD17-96-1-6112	ADB241664
DAMD17-96-1-6112	ADB259038
DAMD17-97-1-7084	ADB238008
DAMD17-97-1-7084	ADB251635
DAMD17-97-1-7084	ADB258430
DAMD17-98-1-8069	ADB259879
DAMD17-98-1-8069	ADB259953
DAMD17-97-C-7066	ADB242427
DAMD17-97-C-7066	ADB260252
DAMD17-97-1-7165	ADB249668
DAMD17-97-1-7165	ADB258879
DAMD17-97-1-7153	ADB248345
DAMD17-97-1-7153	ADB258834
DAMD17-96-1-6102	ADB240188
DAMD17-96-1-6102	ADB257406
DAMD17-97-1-7080	ADB240660
DAMD17-97-1-7080	ADB252910
DAMD17-96-1-6295	ADB249407
DAMD17-96-1-6295	ADB259330
DAMD17-96-1-6284	ADB240578
DAMD17-96-1-6284	ADB259036
DAMD17-97-1-7140	ADB251634
DAMD17-97-1-7140	ADB259959
DAMD17-96-1-6066	ADB235510
DAMD17-96-1-6029	ADB259877
DAMD17-96-1-6020	ADB244256
DAMD17-96-1-6023	ADB231769
DAMD17-94-J-4475	ADB258846
DAMD17-99-1-9048	ADB258562
DAMD17-99-1-9035	ADB261532
DAMD17-98-C-8029	ADB261408
DAMD17-97-1-7299	ADB258750
DAMD17-97-1-7060	ADB257715
DAMD17-97-1-7009	ADB252283
DAMD17-96-1-6152	ADB228766
DAMD17-96-1-6146	ADB253635
DAMD17-96-1-6098	ADB239338
DAMD17-94-J-4370	ADB235501
DAMD17-94-J-4360	ADB220023
DAMD17-94-J-4317	ADB222726
DAMD17-94-J-4055	ADB220035
DAMD17-94-J-4112	ADB222127
DAMD17-94-J-4391	ADB219964
DAMD17-94-J-4391	ADB233754